Structure-Property Relationships in the Thallium Telluride Family and Other Materials

by
Kathryn Elizabeth Arpino

A dissertation submitted to Johns Hopkins University in conformity with the requirements for the degree of Doctor of Philosophy

Baltimore, Maryland
February, 2017

Intended to be blank

Abstract

The structure and bonding of a solid-state material greatly affect its physical properties. In this dissertation, a parent material Tl_5Te_3 is shown to both have intriguing structural features and to host multiple interesting physical phenomena, including superconductivity and topological surface states. Series of ternary derivatives $Sn_xTl_{1-x}Tl_4Te_3$ and $Tl_5Te_{3-x}Se_x$ of this compound investigate the change in structure and physical properties as a function of isovalent substitution; by maintaining charge balance, isovalent substitution allows the effects of bonding character to be isolated. The structure of these compounds was probed with long-range and local structure diffraction methods including in-house and laboratory x-ray diffraction and pair-distribution function analysis. The superconducting physical properties are evaluated primarily through analysis of heat capacity and magnetization data, while density function theory and angle-resolved photoelectron spectroscopy predict and visualize topological surface states. These series illustrate a number of effects as a function of bonding: both $Sn_xTl_{1-x}Tl_4Te_3$ and $Tl_5Te_{3-x}Se_x$ demonstrate modulation, including increase, of superconductivity; at least one topological phase transition is indicated in the $Sn_xTl_{1-x}Tl_4Te_3$ series; and $Tl_5Te_{3-x}Se_x$ shows a structural distortion. The bulk of this dissertation therefore establishes and characterizes the first material to host both topological surface states and bulk, intrinsic superconductivity, and shows how chemical control of the bonding can modulate these two physical properties.

Additionally, a series of $Yb_{2+x}Ti_{2-x}O_{7-\delta}$ shows how the precise stoichiometry affects the physical properties of frustrated magnetic pyrochlore $Yb_2Ti_2O_7$, demonstrating the im-

portance of pure samples. In this material, there exists a low-temperature transition of enormous specific heat to a much-debated ground state. Results from this research indicates that at least some of the contention about the true physical character of this material's ground state is due to the effect of off-stoichiometry in crystal samples on the measured physical properties. Pertinently, a method for growing more pure $Yb_2Ti_2O_7$ crystals is put forth.

Dissertation committee

*Professor Tyrel M. McQueen (**Advisor**)*

Professor Arthur Bragg

Professor Kit H. Bowen, Jr.

Men love to wonder, and that

is the seed of our science.

– Ralph Waldo Emerson

Intended to be blank

Acknowledgments

During my time here, I have benefited indescribably from the knowledge and patience of members of the lab who welcomed and taught me. John Sheckelton, Patrick Cottingham, Jamie Neilsen, W. Adam Phelan, and Allyson Fry-Petit, I owe you a debt of gratitude I endeavor to pay forward. I owe thanks to those lab members in my cohort, Benjamin Trump and David Wallace, who worked and grew with me in lab, and I wish them the best in their current and future endeavors. Joe Caron, Jessica Panella, Zachary Kelly, Juan Chamorro, Mike Quintero, Jennifer Morey, Jake Tutmaher, Mike Winiarski, Cheng Wan, Thao Tranh, Hongcheng Lu, Veronica Stewart, and Mekhola Sinha, you have each contributed to an experience I will cherish. To all of the lab, thank you for engaging with me, talking through problems and concepts, bringing new angles and opinions, and expanding our understanding together. Thank you for laughing. Thank you for creating a workplace I enjoyed coming in to everyday, a workplace I will miss.

Many thanks to Jean Goodwin for bringing me here and changing my life. To Rosalie Elder, for help, support, and friendship. To Boris Steinburg and Brian Schriver for always making things run smoothly and taking care of our lab among many others, and always with a smile.

On a personal note, I thank my family, friends, and loved ones for their compassion, support, and care. You mean the world to me.

Thanks to my friends in the program who do not fall into these other categories, notably Sara Marquez, Evan Collins, and Julie Spencer, who have helped me with their time and

knowledge both in and outside the realm of science, and have made my time here fun.

I would like to especially acknowledge the Physics department community which I worked in. Professors Collin Broholm, N. Peter Armitage, and Chia-Ling Chien have been wise, accessible resources to me, and have each enriched the department and IQM with their distinctive personalities. Fellow students and post-docs have made me feel welcome, taught me patiently, challenged me, and connected with me. Among those, I would like to specifically acknowledge Wes Fuhrmann, Thomas O'Connor, Guy Marcus, Shan Wu, and Martin Mourigal.

I have learned much from the Institute of Quantum Matter's renowned crystal growth expert Seyed Koohpayeh, and am extremely grateful to have had the chance to work with, observe, and learn from him.

Of course, the singular most important person to whom I owe thanks is my advisor, Tyrel M. McQueen, who embodies the aspirational combination of being a brilliant person and a genuinely nice human being. I am beyond indebted to have benefited from his expansive knowledge coupled with his ability to communicate with a variety of audiences at multiple levels. His enthusiasm for science, personality, and passion for teaching has created an unparalleled lab which I have been incredibly fortunate to have been a part of.

Table of Contents

Intended to be blank

List of Figures

List of Figures

List of Tables

1 Introduction

This dissertation focuses mainly on the Tl_5Te_3 chemical family, which hosts an array of rich chemical and physical properties: two types of correlated electron phenomena – superconductivity and topological surface states – exist in the parent compound Tl_5Te_3, and the unusual cation charge of Tl^{2+} provides an avenue to explore the relationship between charge disproportionation and bonding. In order to understand the work that follows, some introductory explanations of relevant scientific concepts are presented in this chapter.

1.1 Crystalline materials, spatial symmetries, and momentum space

This dissertation focuses on exclusively solid-state crystalline materials. Long-range periodic patterning is the defining characteristic that separates crystalline from amorphous materials. As crystals can be composed of an infinite number of atom and geometry combinations, a systematic classification of patterns is needed. For this purpose, patterns are described by their governing symmetries. A symmetry element describes the relationships between atoms in the structure, e.g., an inversion center is a point symmetry element i which dictates that $(x, y, z) = (-x, -y, -z)$, so if there is an element at $(1/4, 1/2, 1/8)$ from the origin, the inversion symmetry element requires there be another atom of the same ele-

ment at $(-1/4, -1/2, -1/8)$. Crystals are historically defined as having translational symmetry as well as point symmetries. (This definition excludes a class of materials known as quasicrysals, which have long-range order extending in a fractal rather than translational fashion.) Translations displace uniaxially, e.g., $(x, y, z) = (x + 1, y, z)$, and when applied repeatedly to a unit cell can build an entire crystal structure. The set of symmetry elements which describe the patterning of a crystal are collectively referred to as the space group. As crystals are defined by translation, space groups include both point and space symmetry elements (such as a glide plane, which is the combination of a mirror symmetry and a translation symmetry). Because there exist only a limited number of translationally repeatable symmetry elements, there is a finite number of spacegroups (in each dimensional space): an infinite number of possible unit cells have a limited variety of ordering patterns. As such, it is important to note that two unit cells with the same symmetry group may have very different structures. However, within the same overall structure, change of space group may be viewed as a telling proxy for the structural distortion which drives it.

An important consequence of crystalline materials being extended in multiple spatial dimensions is that the atoms of the unit cell generate many layers, or planes. These planes are capable with interacting with the planar wavefront of waves such as radiation (e.g., x-rays) or accelerated wave-particles (e.g., neutrons). Layers can be thought of as having two characteristics: the direction (defined uniquely mathematically by the vector perpendicular to them) and the interlayer spacing. They are indexed by Miller indices (hkl) where h, k, and l, are the reciprocal of the fractional distance of the unit cell that the layer is located relative to the origin.

Because crystalline materials and their internal layers of planes extend periodically in spatial dimensions, they can be considered in both real space and in what is known as reciprocal, or momentum $\mathbf{k}$-, space, which is a Fourier transform of the former. Fourier transforms are functions that can represent any spatial object or pattern as a combination of sinusoidal functions. They therefore provide a valuable way to translate long-range extended

structures to short-range condensed structures and vice versa (e.g., from a wavepacket to a distribution of frequencies). In reciprocal/momentum, space, the real space crystal lattice parameters a, b, and c are transformed to reciprocal space vectors a^*, b^*, and c^*, where i^* is perpendicular to i and has length proportional to the reciprocal of the length of i. The unit cell in reciprocal space is called the first Brillouin zone, which is mapped out by extending $\pm\pi/i$ so that the total length is side length $2\pi/i$. The factor of 2π is required by the periodicity of the real space unit cell. Relevant for diffraction (see Section 2.2), each family of planes in real space (each Miller index) corresponds to a point in reciprocal space.

In this momentum-space analogue of the unit cell, special symmetry points arise. For example, the family of planes spaced one unit cell apart oriented perpendicular to the c faces have Miller indices (001). In the Brillouin zone, this momentum point has special symmetry: this special point is one of several which is invariant under time $\mathbb{T}$ symmetry. These points are referred to as time-reversal invariant momentum (TRIM) points, and Kramer's theorem dictates that spin-up and spin-down states must be be degenerate at them: $(E(k,\uparrow) = E(-k,\downarrow))$. It proves useful to consider the energy of bands in reciprocal space, as crystal momentum correlates with symmetry vectors. A band structure is generated by plotting the bands with energy on the y-axis and crystalline momentum on the x-axis with special points as references.

1.2 Structure-property relationships

A driving force of basic materials research is investigating how bonding and structure affect the emergent properties of materials; specifically, how one can intentionally manipulate the bonding chemically to effect a change in the physical properties. For a compound with an interesting physical property, one can remove, substitute, or add specific atoms intelligently using the guiding trends of the periodic table as a route to intentionally alter the compound's bonding, charge balance, and structure in order to observe the effects on

the desired property. Practically, this structure-property relationship is critical to designing new directed materials. The research presented in this dissertation focuses mainly on the effect of substitutional doping on the structure and properties of two materials, the Tl_5Te_3 family and $Yb_2Ti_2O_7$.

1.2.1 Charge disproportionation

Charge disproportionation refers to a situation in which an ion is relatively unstable at its formal oxidation state and instead occurs in populations of other, more stable oxidation states (generally, and most simply, charges which have one electron more or fewer than the formal charge) which average to the nominal formal oxidation:

$$M^{n+} \rightarrow (1/2)M^{(n+1)+} + (1/2)M^{(n-1)+} \tag{1.1}$$

Chemically, charge disproportionation occurs because the M^{n+} oxidation state is energetically unfavorable relative to a mix of the adjacent oxidations. Typically, this occurs for an ion with oxidation state one electron away from a completely full or completely empty subshell due to the stabilizing energy of filled subshells. Charge disproportionation is more common in heavy elements, especially lower-right *p*-block elements due to the inert-pair effect which stabilizes a s^2 shell. (The inert-pair effect is a co-product of empirically poor shielding of the nucleus by the *d* and *f* inner subshells and of predictably lower bond energies for these electrons which are too far from the nucleus to hold two atoms together strongly.)

A classic example is Bi^{4+}, which has electron configuration [Xe]s^1. The single *s* electron is not held very strongly (has a low ionization energy) due to the large, filled n = 5 [Xe] shell; in contrast, the [Xe]s^0 and [Xe]s^2 electronic configurations are more stable due to the completely filled shell in the former and the filled subshell and inert-pair effect of the latter. By charge disproportionating to the 3+ and 5+ oxidation states, the nominal Bi^{4+}

ion lowers its energy.

Charge disproportionation can be described as a "negative Hubbard-U" effect. The parameter Hubbard U is defined as $U = IE - E_A$, the difference of the ionization energy and the electron affinity. In the Bi^{4+} example, this formalization can be understood as removing an electron from one Bi^{4+}, costing the ionization energy, and adding the electron to another Bi^{4+}, releasing the electron affinity energy. Because the overall effect is a lower energy state, U for Bi^{4+} is negative, or Bi^{4+} can be said to be a "negative Hubbard-U ion."

In extended solids, this mechanism frequently gives rise to a charge density wave (CDW), a periodic modulation of charge. This occurs when the two more stable ionic charges order in a fashion that is coherent on long-range scales, and generally occurs with a structural modulation due to the bonding spheres of the differently charged ions. For example, $BaBiO_3$ is a distorted perovskite which has Bi^{4+}, a ion liable to charge disproportionation, at the octahedral *B*-site [7]. Charge disproportionation the Bi octahedral centers causes alternatively smaller (Bi^{5+} at the centers) and larger (Bi^{3+} at the centers) octahedra, giving rise to a classic charge density wave.

Charge disporportionation may be detected by effects on the structure due to the different bond lengths and geometries of the two resultant ions. Long-range charge density waves break symmetries, lowing the spacegroup, and so may be discerned by traditional diffraction measurements. If the bond distances of the two ions are sufficiently different, this splitting should be visible on pair distribution function (Section 2.2.2). Spectroscopic techniques such as x-ray photoelectron spectroscopy and Auger spectroscopy are capable of directly probing the binding energies (and thus oxidation states) of ions in the solid state.

1.3 Correlated electron phenomena

Correlated electron phenomena is a general term referring to the coupling of one or more degrees of freedom (such as charge, spin, orbital, or lattice) such that unconventional emer-

gent (macroscopic) electronic states occur. Examples include superconductivity, metal-insulator transitions, frustrated magnetism, and topologically non-trivial states.

1.3.1 Superconductivity

A superconductor is a material which conducts electricity with zero electrical resistance ("superconducts") when in its superconducting state [1]. Simply put, this occurs because the valence electrons of the superconducting material, each of which is a fermion with spin $\pm 1/2$, pair to form bosonic particles known as Cooper pairs. Being bosons, these particles can occupy the same state, and thus experience no resistance against current. The superconducting state is bound by a critical temperature T_c and critical field(s) H_c. Under classical theory, these parameters are a measure of the strength which holds together the Cooper pairs. In order for two negatively charged electrons to form a Cooper pair, some interaction must link them, and the energy of the Cooper pair must be less than that of two electrons. This difference in energy is called the pairing energy Δ [2]. The most common mechanism by which electrons form Cooper pairs is through electron-phonon coupling. In this mechanism, the negative charge of one electron couples with the vibrations of the lattice such that a second electron is attracted to the positive charge modulation. Such a mechanism only works when the thermal energy of the material is less than that of the pairing energy Δ:

$$\frac{2\Delta}{k_B T_c} = 3.53 \tag{1.2}$$

hence materials only superconduct below a critical temperature T_c.

In addition to having zero electrical resistance, superconductors have the additional interesting physical property that they reject incident magnetic field, known as the Meissner effect. When a magnetic field is applied, eddy currants in a superconductor generate an equal and opposite magnetic field such that beyond the penetration depth λ the net field at the sample interior is zero. London derived the penetration depth from Maxwell's equations

[1]:

$$\lambda = \sqrt{\frac{mc^2}{4\pi n_s e^2}}. \tag{1.3}$$

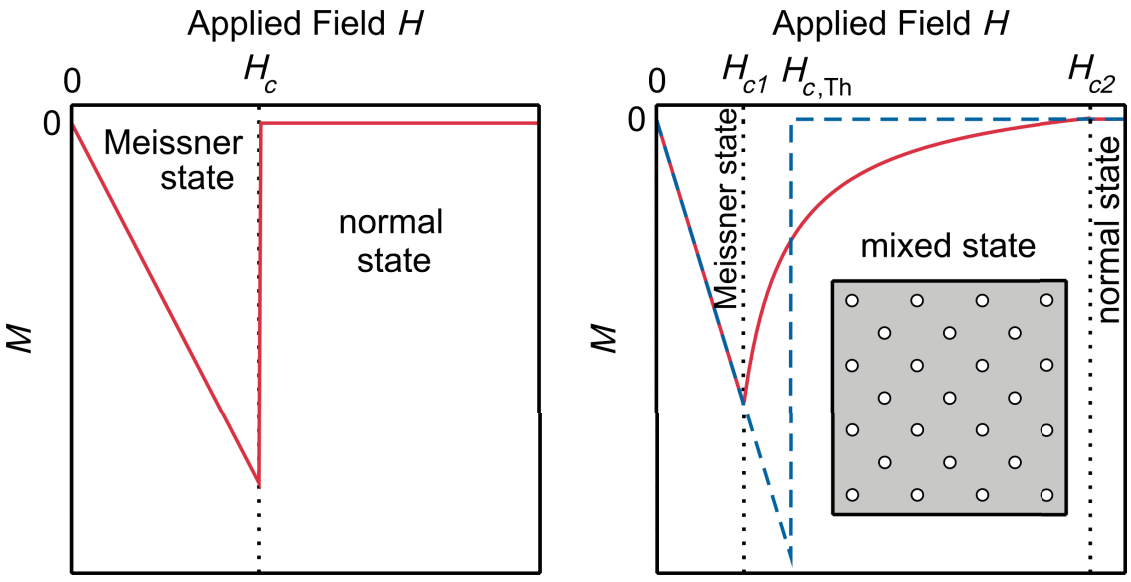

Figure 1.3.1: A graphic shows the isothermal magnetic response (M) of Type I and Type II superconductors below their transition temperature T_c as a function of applied field H. Type I superconductors transition directly from a fully superconducting Meissner state to a fully non-superconducting normal state, and therefore have one critical field H_c. Type II superconductors transition through a partially superconducting state, called the mixed state, in which the applied field penetrates through vortices of non-superconducting regions while applied field is screened from the remaining superconducting region. The thermodynamical critical field of a Type II superconductor is also plotted.

Superconductors are bound by upper critical field(s) because there exists a maximum field which the superconductor can fully expel. A Type I superconductor fully expels applied magnetic fields up to a critical field H_c, above which it does not superconduct at all. A Type II superconductor has two critical fields: it fully expels applied magnetic fields up to a lower critical field H_{c1} and does not superconduct at all past a second, higher field known as the upper critical field H_{c2}. At fields between H_{c1} and H_{c2}, the material is partially superconducting: the external magnetic field penetrates non-superconducting vortices while the rest of the material superconducts and repels the magnetic field. Figure 1.3.1 illustrates the magnetization response of the two types of superconductors as a function of applied

field. The difference between the two types is determined by whether it is energetically favorable to create interfaces. This effect is captured in a single parameter $\kappa = \lambda/\xi$ called the Ginzburg-Landau parameter, the ratio of the penetration depth and coherence length: values of $\kappa < 1/\sqrt{2}$ indicate Type I superconductivity, while $\kappa > 1/\sqrt{2}$ indicate Type II. The spatial coherence length involved in this ratio was previously introduced by Pippard as the maximum length scale required to maintain coherence of the electrons of the Cooper pair:

$$\xi = \frac{\hbar v_F}{k_B T_c} \tag{1.4}$$

where v_F is the Fermi velocity [1]. Type II superconductors have an additional parameter called the thermodynamic critical field $H_{c_{\mathrm{Th}}}$, which is the temperature at which the area under the two curves (the measured red curve and the hypothetical blue curve in Figure 1.3.1) are equal. (An alternative way of understanding and estimating $H_{c_{\mathrm{Th}}}$ is to choose the value which satisfies $\int_{H_{c1}}^{H_{c_{\mathrm{Th}}}} MdH = \int_{H_{c_{\mathrm{Th}}}}^{H_{c2}} MdH$.) This thermodynamic parameter is dictated by the Gibbs free entropy, which must satisfy $dG = -SdT - MdH$, a relationship which simplifies to $dG = -MdH$ (or, the integral of the curves shown) for the isothermal relationships shown in Figure 1.3.1 [1].

A superconductor may be detected experimentally by three methods: by measuring the electrical resistance to low temperatures, the response to applied field, or the heat capacity through the superconducting transition. For a superconducting material, resistance measurements will drop to zero resistance below T_c, the magnetic response will expel the applied magnetic field below T_c, and the heat capacity will exhibit a peak called a lambda anomaly around T_c as the material undergoes a second-order phase transition from the normal to superconducting phase. Experimentally, resistance is measured via leads on the surface and so is subject to surface effects. Moreover, trace superconducting impurities may result in a zero-resistance measurement regardless of the bulk properties. In contrast, both magnetization response and heat capacity can differentiate between bulk and trace signal from the magnitude. Resistivity measurement were not used to evaluate superconductivity

in this dissertation; the remaining two methods are explained in detail in Subsections 2.3.1 and 2.3.2.

1.3.2 Topological insulators

Over the past decade, research in topological phases of matter has exploded, from the initial theoretical predictions of topological insulators [3–5] to the most recent Nobel prize in Physics [6]. The term "topological insulator" describes an insulating material with metallic states on the surface. These surface states originate in the bulk band structure: materials with an odd number of band parity inversions are topologically distinct from those with an even number (including zero). Band parity refers to the symmetry of a band; like the point symmetries of molecules which has symmetric or antisymmetric (gerade or ungerade) orbitals, bands of an extended solid are also symmetric or antisymmetric with regard to phase. An inversion of bands with opposite parity makes the ordering of band symmetries distinct from that of the exterior atmosphere or vacuum. A crossing of bands therefore **must** occur at the interface (at the surface), giving rise to surface states.

Band parity inversions must occur in an odd number in order to have a strong topological insulator under what is called the $\mathbb{Z}_2$ invariant. The $\mathbb{Z}_2$ invariant ν is defined as

$$(-1)^{\nu} = \prod_{i} \prod_{m=1}^{N} \xi_{2m}(\Gamma_i) \tag{1.5}$$

where i is the number of TRIM points, $\xi_{2m}(\Gamma_i) = \pm 1$ is the eigenvecter describing the parity of the $2m$th occupied band at TRIM point Γ_i, and there are $2N$ total occupied bands [7]. Therefore the $\mathbb{Z}_2$ invariant ν is essentially a measure of the ordering of band parities at TRIM points for the occupied bands: $\nu = 0$ is topologically trivial, and $\nu = 1$ is non-trivial, signifying a odd number of band-parity inversions around the Fermi level at TRIM points.

Figure 1.3.2 illustrates the surfaces states of a topological insulator. Kramer's theorem, $E(k,\uparrow) = E(-k,\downarrow)$, dictates that spin-up and spin-down states must be degenerate at points

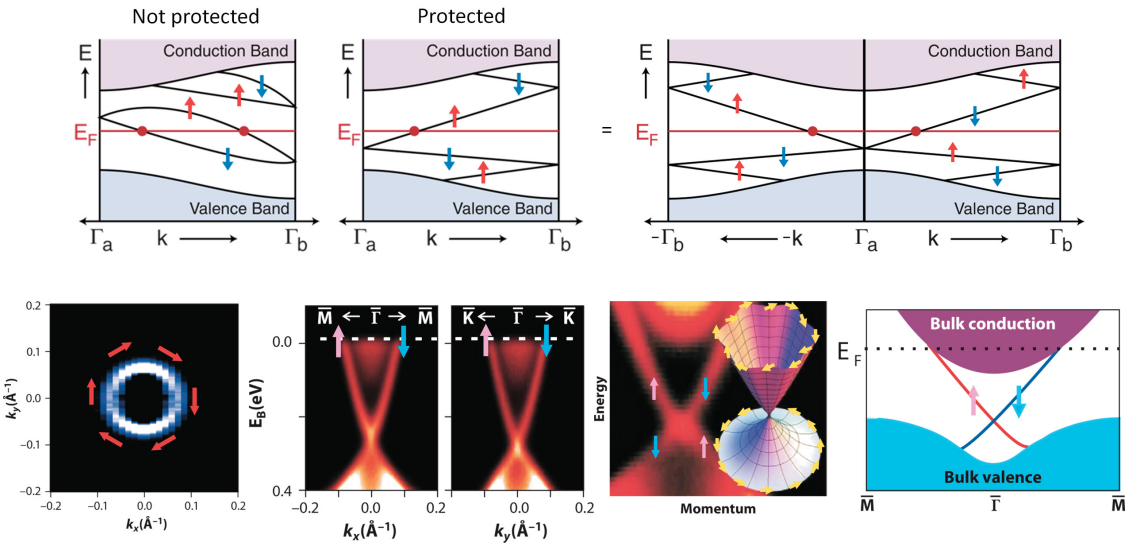

Figure 1.3.2: The protected surface states of topological insulators is shown in theory and experiment. The top panel, adapted from adapted from Hasan and Kane [7], shows unprotected (left) and protected (right) arrangements of spin-up and -down surfaces states imposed on a band structure. Only when there is an odd number of states crossing the Fermi level between the two TRIM points are those states protected. An expanded view of the band structure with protected surfaces states is shown on the far right of the upper panel. The lower panel, from Hasan and Moore [8] shows the surface states composing the Dirac cone in Bi_2Se_3 from a number of perspectives. From left to right, the images depict the spin direction as a function of momentum for the top of the Dirac cone, ARPES data showing the Dirac cone in two directions along the Brillouin zone, an artist's rendition of a Dirac cone overlaid on ARPES visualization of one, and a cartoon band structure showing the origin of the Dirac cone.

of time-reversal invariant momentum (TRIM points) because $\mathbb{T}$-symmetry is odd. An even number of states crossing the Fermi level between TRIM points (left, upper panel) are not protected because the spin-up and spin-down states meet pairwise at the TRIM point, and so perturbing either the states or the Fermi level could avoid the states crossing the Fermi level. Conversely, an odd number of bands crossing the Fermi level between two TRIM points ensures a topologically protected gapless surface state regardless of any energy perturbations (right, upper panel). Thus these surfaces states are protected. Due to Kramer's theorem, these states mirror across the TRIM point, creating a cone called the Dirac cone: in this situation, states at the same energy with negative momentum ($-k$) have the opposite

spin direction. As a result, the spin-direction of an electron in the surface is coupled with its momentum: these phenomenon is referred to as "spin-momentum locking" and could give rise to a whole field of spintronics.

Strong two- and three-dimensional topological insulators were predicted theoretically [3–5] and subsequently discovered [9, 10], and the frenzied search for more topological materials is still underway. Materials with non-trivial topology have a wide array of new fundamental science and potential applications. Specifically, those materials which combine topological surface states and superconductivity have the potential to test the predictions of new states of matter and exotic quasiparticles, such as the Majorana fermion, and open the field for new technologies such as quantum computing [11–14]. However, superconductivity in topological insulators has been limited to proximity effects [15] and optimal doping of $Cu_xBi_2Se_3$ [16] and the topological crystalline insulator (TCI) $Sn_{1-x}In_xTe$ [17]. The paucity of intrinsically superconducting topological insulators poses both experimental and theoretical challenges.

One can predict $\mathbb{Z}_2$ topologically non-trivial materials by computing the number of band-parity inversions at TRIM points of calculated band structures. Spin-orbit coupling is considered the major driving force of such band-parity inversions; calculating band structures with and without accounting for spin-orbit coupling can show if it causes the band-parity inversion. Experimentally, surfaces states may be detected by angle-resolved photoelectron spectroscopy, which probes the electronic states near the Fermi level mapped in the Brillouin zone. Note the ARPES alone is insufficient to prove non-trivial topology, as surface states, while uncommon, could arise from a number of phenomena including, but not only, non-trivial topology. Spin resolution via spin-resolved ARPES ("spARPES") can determine if these surface states are spin-momentum locked.

Initially, the reported strong three-dimensional $\mathbb{Z}_2$ topological insulators (namely, $Bi_xSb_{1-x}Bi_2Se_3$, Bi_2Te_3, and Sb_2Te_3) all had trigonal space group symmetry $R\bar{3}m$ [3–5, 9, 10]. The time-reversal invariant points of this symmetry class all occur in odd-

numbered sets (one Γ, one Z, three F, and three L points); a band inversion at any one or odd number of these points therefore guarantees a $\mathbb{Z}_2$ topological insulator. It may prove fruitful to investigate other crystal systems which also have odd-numbered sets of time-reversal invariant points. Chapter 5 shows the existence of non-trivial surface states in tetragonal Tl_5Te_3, a new structure type to host non-trivial $\mathbb{Z}_2$ topology.

A related class of materials called topological crystalline insulators (TCIs) also has spin-momentum locked surface states. In these materials, the topological surface states which result from crystal symmetry rather than time-reversal symmetry (and thus are not non-trivial under $\mathbb{Z}_2$ topology) [18]. Incidentally, TCIs may have an even number of band inversions, and therefore could exist in more materials. Currently known TCIS include cubic SnTe and $Pb_xSn_{1-x}Te$ [19, 20]. The existence of this class of materials illustrates the potency of using crystal symmetries to discover topological surface states.

1.3.3 Geometric magnetic frustration

Geometric magnetic frustration occurs in materials whose structure prevents the dominant magnetic interaction from achieving a single lowest-energy ground state, generally antiferromagnets with triangle-based structures [21, 22]. Antiferromagnetism refers to a counter-aligned arrangement of electron spins: each spin aligns in an opposite direction than its neighbor (compared to more well known ferromagnets, or colloquial "magnets," materials in which electron spins align, or all point in the same direction). The term J describes pair-wise magnetic interactions: the sign indicates whether electrons prefer to align ($J > 0$) or counter-align ($J < 0$), and the magnitude indicates the strength of the interaction. Because this interaction occurs pairwise, structures based on triangles can create a lattice in which it is impossible to satisfy all interactions. Examples of these structures include two-dimensional triangular and kagome lattices which have side- and corner-sharing triangles, and the three-dimensional pyrochlore lattice which has corner-sharing tetrahedra (each side of which is a triangle) [21–23].

Antiferromagnetic interactions cannot be completely satisfied on a regular triangle: the lowest energy state has two sidelengths which satisfy antiferromagnetic interaction, and one which does not; likewise a lowest-energy antiferromagnetic tetrahedron has four sidelengths which satisfy the interaction and two sidelengths which do not. However, in a regular lattice it does not matter which vertex and sidelengths have the unfavorable interactions; so an independent triangle has six equally degenerate lowest-energy configurations instead of the two (one spin-up and one spin-down) that would occur if there were a single lowest-energy state, as there is for a ferromagnetic triangle. In extended triangle-based lattices, the spin on one site affects not just the configuration in that triangle but, due to the connectivity of that triangle in the lattice, has ramifications propagating through the entire structure. This gives rise to a far, far greater number of degenerate lowest energy states whichf scales with the crystallite size, called a "macroscopic" number of degenerate lowest-energy configurations [21–23].

Pyrochlore $Yb_2Ti_2O_7$ is a type of geometrically frustrated material known as a spin ice [21–23]. Pyrochlores has two interpenetrating sublattices of corner-sharing tetrahedra, each of which can potentially host geometric frustration. The lowest-energy state for an arrangement of corner-sharing tetrahedra is "2-in-2-out": two spins point into each tetrahedron, and two point out. The name "spin ice" comes from the similarity of this 2-in-2-out configuration with that of the inter- and intra molecular hydrogen bonds in water ice: envisioning oxygen as the center of a tetrahedron, there are two short, intramolecular bonds to hydrogens and two long, intermolecular bonds to hydrogens, which can be thought of an analogs for two spins pointing in and two pointing out.

It is common for materials to spontaneously distort in order to relieve ground state degeneracy present in geometric magnetic frustration, or for other defects to lower the energy of a specific configuration. However, if a structure remains perfectly regular down to very low temperatures, an interesting array of quantum materials are theorized. In quantum spin ices, quantum fluctuations are sufficient to switch between spin-frozen degenerate ground

states [23, 24]. Quantum spin liquids, in contrast, possess spins which never align and dynamically fluctuate even at $T = 0$ K [25, 26].

1.4 Tl_5Te_3 family background

The bulk of the research discussed in this disseration focuses on Tl_5Te_3 and its derivatives. Tl_5Te_3 was initially indicated as a γ-phase in studies of the binary Tl-Te phase diagram [27, 28] (though was notably and controversially absent from one [29]). In the 1960s, a number of studies further investigating these phase diagrams confirmed the existence and identity of the γ-phase as Tl_5Te_3. [30–37] One of these studies also found Tl_5Te_3 to be superconducting at $T_c \approx 2.2$ K and further looked into the stoichiometry and superconductivity [32, 38]. The compound has since received some attention as a potential thermoelectric [39–43].

Structurally, Tl_5Te_3 is a subfamily of the In_5Bi_3 family, which in turn is part of the larger Cr_5B_3 family which includes about 40 binary metallic compounds. The structure and bonding of these compounds are discussed in detail in Section 3.2.

Table 1.4.1: List of known Tl_5Te_3 ternary derivatives

Formula	Substituent atoms
$M Tl_4Te_3$	Sn [44–47], Pb [44, 45, 47–49], Cu [47, 50, 51], Mo [52] Ag [47]
$M Tl_9Te_6$	Bi [45, 49, 53], Sb [45, 54], La [55], Nd [49, 56], Ce [57], Sm [57], Gd [57]
$M Tl_4Se_3$	Pb [59], Sn [60, 61], Au [47, 62]
$M Tl_9Se_6$	Sb [58]
Tl_5Se_2X	Cl, Br, I [64, 65]

A number of ternary derivatives of Tl_5Te_3 exist (Table 1.4.1). Cations have been reported to substitute for thallium, generally forming one of two compounds, $M Tl_4Te_3$ and $M Tl_9Te_6$, depending on the charge of M. Most studies of substituent cations focus predominantly on p-block elements, though some transition metals and rare earth derivatives are

also reported. Compounds with stoichiometry $M Tl_4Te_3$ generally occur for M^{2+} cations, while M^{3+} cations form $M Tl_9Te_6$. A number of ternary selenides also exist, as well as a sulfide, $SnTl_4S_3$ [63]. Ternary selenide compounds exist with substitution of a single molar equivalent of halide anions. Additionally, Tl_5Se_3 and/or $Tl_5Se_{3-\delta}$ have been reported to exist [64, 66–68, 70, 71]; a detailed discussion of these compounds is given in Section 7.3.

Bibliography

[1] C. P. Poole, H. A. Farach, and R. J. Creswick, *Superconductivitiy* (Academic Press, San Diego, 1995).

[2] J. C. Bardeen, L. N. Cooper, and J. R. Schrieffer, Phys. Rev. **108**, 1175 (1957).

[3] L. Fu, C. L. Kane, and E. J. Mele, Phys. Rev. Lett. **98**, 106803 (2007).

[4] J. E. Moore and L. Balents, Phys. Rev. B **75**, 121306 (2007).

[5] R. Roy, Phys. Rev. B **79**, 195321 (2009); **79**, 195322 (2009).

[6] The Class for Physics of the Royal Swedish Academy of Science, "Scientific Background on the Nobel Prize in Physics: Topological phase transitions and topological phases of matter" (2016).

[7] M. Z. Hasan and C. L. Kane, arXiv:1002.3895 (2010).

[8] M. Z. Hasan and J. E. Moore, Annu. Rev. Condens. Matter Phys. **2**, 55 (2011).

[9] D. Hsieh, D. Qian, L. Wray, Y. Xia, Y.S. Hor, R. J. Cava and M. Z. Hasan, Nature **452**, 970 (2008).

[10] M. König *et al.*, Science **318**, 766 (2007).

[11] A. C. Potter and P. A. Lee, Phys. Rev. B **85**, 094516 (2012).

[12] J. Linder, Y. Tanaka, T. Yokoyama, A. Sudbo, and N. Nagaosa, Phys. Rev. Lett. **104**, 067001 (2010).

[13] J. D. Sau, R. M. Lutchyn, S. Tewari, and S. Das Sarma, Phys. Rev. B **82**, 094522 (2010).

[14] S. Tewari, T. D. Stanescu, J. D. Sau, and S. Das Sarma, New J. Phys. **13**, 065004 (2011).

[15] G. Koren, T. Kirzhner, E. Lahoud, K. B. Chashka, and A. Kanigel, Phys. Rev. B **84**, 224521 (2011).

[16] Y. S. Hor *et al.*, Phys. Rev. Lett. **104**, 057001 (2010).

[17] S. Sasaki *et al.*, Phys. Rev. Lett. **109**, 217004 (2012).

[18] L. Fu, Phys. Rev. Lett. **106**, 106802 (2011).

[19] T. H. Hsieh, H. Lin, J. Liu, W. Duan, A. Bansil, and L. Fu, Nature Comm. **3**, 892, (2012).

[20] S.-Y. Xu, C. Liu, N. Alidoust, M. Neupane, D. Qian, I. Belopolski, J. D. Denlinger, Y. J. Wang, H. Lin, L. A. Wray, G. Landolt, B. Slomski, J. H. Dil, A. Marcinkova, E. Morosan, Q. Gibson, R. Sankar, F. C. Chou, R. J. Cava, A. Bansil, and M. Z. Hasan, Nature Comm. **3**, 1192 (2012).

[21] A. P. Ramirez, Ann. Rev. Mater. Sci. **24**, 453 (1994).

[22] J. S. Gardner, M. J. P. Gingras, and J. E. Greedan, Rev. Mod. Phys. **82**, 53 (2010).

[23] S. T. Bramwell and M. J. P. Gingras, Science **294**, 1495 (2001).

[24] S. B Lee, S. Onoda, and L. Balents, Phys. Rev. B **86**, 104412 (2012.)

[25] B. Canals and C. Lacroix, Phys. Rev. Lett. **80**, 2933 (1998).

[26] L. Balents, Nature **464**, 199 (2010).

[27] M. Chikashigé, Z. anorg. allg. Chem. **78**, 68 (1912).

[28] A. P. Obukhov and N.S. Bubyreva, Izv. Sektora Fiz.-Khim. Anal. **17**, 276 (1949).

[29] M. Hansen, *Constitution of Binary Alloys* (McGraw-Hill Book Company, New York, 1958).

[30] A. Rabenau, A. Stegherr, and P. Eckerlin, Z. Metalkd. **51** 29 (1960).

[31] P. Flicker, Z. Metalkd. **8**, 641 (1966).

[32] A. Juodakis and C. R. Kannewurf, J. Appl. Phys. **39**, 3003 (1968).

[33] K. P. Lips and W. Nahlik, Annalen der Physik **476**, 402 (1968).

[34] E. Cruceanu, Z. Metalkd. **11**, 852 (1969).

[35] E. Cruceanu and S. Sladaru, J. Materials Science **4**, 410 (1969).

[36] E. Cruceanu, R. Lück, and H. Schwarz, J. Appl. Phys. **41**, 5223 (1970)

[37] R. P. Ferrier, J. M. Prado, M. R. Anseau, J. Non-Cryst. Solids **8-10**, 798 (1972).

[38] W. H. Haemmerle, W. A. Reed, A. Juodakis, and C. R. Kannewurf, J. Appl. Phys. **44**(3), 1356 (1973).

[39] K. J. Nordell and O. J. Miller, J. Alloys Compd. **241**, 51 (1996).

[40] B. Wölfing, C. Kloc, A. Ramirez, and E. Bucher in *18th International Conference on Thermoelectrics, 1999* p. 546.

[41] H. Matsumoto, K. Kurosaki, H. Muta and S. Yamanaka, Mater. Trans. **50**(7), 1582 (2009).

[42] P. Jund, X. Tao, R. Viennois, and J.-C. Tédenac, Solid State Phenom. **172-174**, 985 (2011).

[43] X. Tao, P. Jund, R. Viennois, and J.-C. Tédenac, J. Phys. Chem. A **115**, 8761 (2011).

[44] S. Bradtmöller and P. Böttcher, Z. anorg. allg. Chem. **619**, 1155 (1993).

[45] Y. V. Voroshilov, M. I. Gurzan, Z. Z. Kish, and L. V. Lada, Neorganicheskie Materialy **24**, 1479 (1988).

[46] B. A. Kuropatwa, A. Assoud, and H. Kleinke, J. Alloys Compd. **509**, 6768 (2011).

[47] T. Doert, S. Höffkes, C. Klein, and P. Böttcher, Supplemental issues of Z. Kristallogr. **3**, 52 (1991).

[48] R. Chami, J.-C. Tédenac, G. Brunet, and M. Maurin, Mat. Res. Bull. **18** 803 (1983).

[49] M. B. Babanly, J.-C. Tédenac, S. Z. Imamalieva, F. N. Guseynov, and G. B. Dashdieva, J. Alloys Compd. **491**, 230 (2010).

[50] S. Bradtmöller and P. Böttcher, Z. Kristallogr. **209**, 97 (1994).

[51] N. B. Babanly, Z. E. Salimov, M. M. Akhmedov, and M. B. Babanly, Russian Journal of Electrochemistry **48**, 68 (2012).

[52] S. Bradtmöller, and P. Böttcher, Z. Kristallogr.**209**, 75 (1994).

[53] T. Doert and P. Böttcher, Z. Kristallogr., **209**, 95 (1994).

[54] T. Doert and P. Böttcher, Z. Kristallogr., **209**, 96 (1994).

[55] S. Bangarigadu-Sanasy, C. R. Sankar, A. Assoud, and H. Kleinke, Dalton Trans. **40**, 862 (2011).

[56] S. Z. Imamalieva, F. M. Sadygov, and M. B. Babanly, Inorg. Mat. **44**, 935 (2008).

Bibliography

[57] M. B. Babanly, S. Z. Imamalieva, D. M. Babanly and F. M. Sadygov, Azerbaidzhanskii Khimicheskii Zhurnal **2**, 122 (2009).

[58] I. Schewe-Miller, Ph.D. thesis, Stuttgart, 1990.

[59] T. O. Malakhovska, M. Y. Sabov, E. Y. Peresh, V. Pavlyuk, B. Marciniak, Chem. Met. Alloys **2**, 15 (2009).

[60] S. Bradtmöller, R. K. Kremer, and P. Böttcher Z. anorg. allg. Chem. **620**, 1073 (1994)

[61] T. A. Malakhovskaya-Rosokha, M. Y. Sabov, I. E. Barchy, and E. Yu. Peresh, Russian Journal of Inorganic Chemistry **57**(3), 439 (2012).

[62] S. Bradtmöller, Ph.D. Thesis, Heinrich-Heine-Universitat, 1995.

[63] S. del Buccia, J.-C Jumas, E. Phillipot, M. Maurin, Rev. Chim. Miner. **18**, 224 (1981).

[64] T. Doert, R. Asmuth, P. Böttcher, J. Alloys Compd. **209**, 151 (1994).

[65] R. Blachnik and H. A. Dreisbach, J. Solid State Chem. **52**, 53 (1984).

[66] M. M. Stasova and B. K. Vainshtein, Kristallografiya **3**, 141 (1958).

[67] L. I. Man, V. S. Parmon, R. M. Imamov, and A. S. Avilov, Kristallografiya **25**, 1070 (1980).

[68] R. Blachnik and H. A. Dreisbach, J. Solid State Chem. **52**, 53 (1984).

[69] T. Doert, R. Asmuth, and P. Böttcher, J. Alloys Compd. **209**, 151 (1994).

[70] P. Böttcher, T. Doert, C. Druska, and S. Bradtmöller, J. Alloys Compd. **246**, 209 (1997).

[71] F. Römermann, Y. Feutelais, S.G. Fries, and R. Blachnik, Intermetallics **8**(1), 52 (2000).

2 Methods

2.1 Single crystal growth

Several structural and physical properties characterization techniques require single crystals. Single crystals can be grown by a variety of methods, including a slow cooling, flux growth, multi-arcs, and directional techniques such as the Bridgman method or floating zone technique. Crystals of the Tl_5Te_3 family were grown in an optical floating zone furnace via a "modified Bridgman floating zone" method developed during the course of this research, typically with a Te traveling solvent. Crystals of $Yb_2Ti_2O_7$ were grown using the traveling solvent floating zone method.

An optical floating zone furnace uses optical light from focused lamps or lasers to heat a small section of material. Because these lamps provide light rather than direct thermal energy, the resulting temperature of, and thermal gradient along, the growth material depends on the material's properties such as reflectivity, heat absorption, and thermal conductivity. The type of optical furnace used in this research was a four-mirror optical floating zone furnace Crystal System Inc. FZ-T-4000-H-VII-VPO-PC equipped with four 1-kW halogen lamps. Carefully calibrated elliptical mirrors around each lamp focus the light onto the very center point of the apparatus, generating a sharp thermal gradient with the center as the hottest zone of the furnace. A camera focused on this point and surrounding area permits the operator to monitor the growth. A limited number of controls allows the operator to adjust the power level delivered to the lamps, the vertical positioning of the sample rel-

ative to the mirrors, and the movement speed and rotation of the sample. Additionally, the atmospheric gas and its pressure (from vacuum to several atmospheres) may be controlled manually.

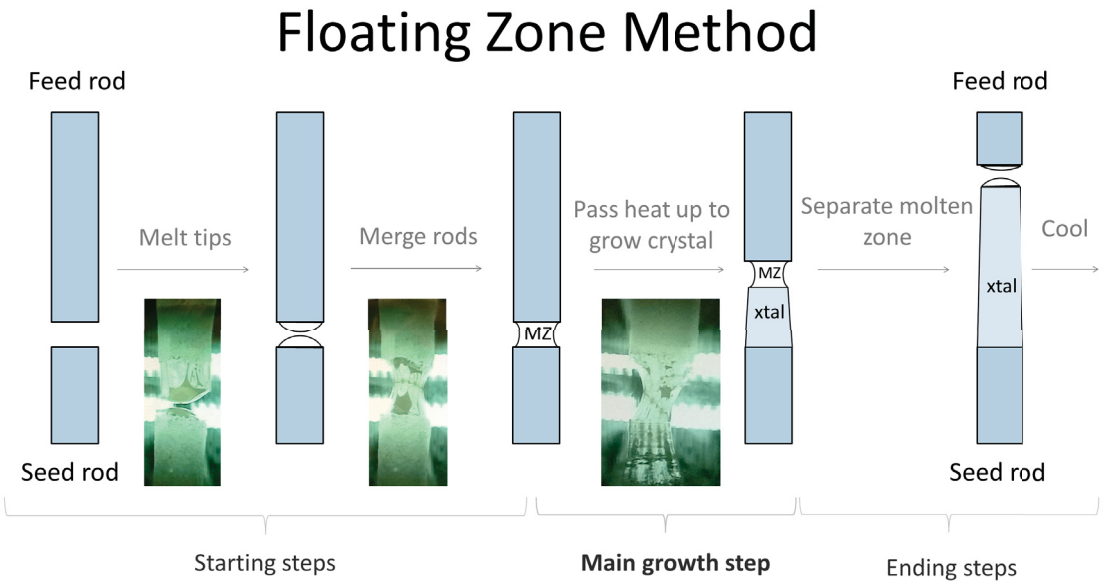

Figure 2.1.1: A graphic shows part of the floating zone crystal growth method with images from a growth. The molten zone is abbreviated "MZ" and crystal "xtal."

The floating zone technique involves melting powder in the hot zone of an optical furnace and drawing the material through the hot zone and its surrounding thermal gradient in order to directionally grow a crystal on the seed rod. This technique produces sizable, roughly cylindrical crystals of 1-5 cm in length and around 0.5 cm in diameter. Typically, the floating zone technique is a crucible-free method: the application of grinding, vacuum, pressure, and sintering generates densified polycrystalline rods which may be mounted self-standing in an optical furnace. Once in the optical furnace, the ends of the two rods are melted and joined, creating a molten zone (MZ) held together by surface tension. Rotation of the rods can help stabilize the molten zone. The molten zone is then passed vertically along the length of the feed rod in order to directionally grow a crystal from the thermal gradient. Figure 2.1.1 shows a portion of this process. The molten zone may be passed along the length of the rods by moving either the rods or the light source, and the growth direction

can be either up or down. The stability of the molten zone and the quality of the crystal formed can be highly sensitive to parameters including the lamp power (effectively the temperature), the growth speed, the alignment of the feed and seed rods, rotation direction and speed, atmosphere, and even how well densified the polycrystalline rods were. During the initial growth steps, multiple crystal grains may form on the seed rod and function as seed crystals. Due to the geometry of these crystal grains, and because different crystal facets grow at different rates, generally one of these grains will become dominant and edge out the others in an ideal floating zone growth. One method of encouraging the selection of a single seed crystal is to intentionally attenuate the interface between the molten zone and seed rod. The floating zone technique is good for a variety of congruently melting metallics and intermetallics, fluorides, oxides, and chalcogenides, as well as some organics [1].

The traveling solvent floating zone (TSFZ) technique is similar to the floating zone technique described above, but includes a solvent (or flux) which "travels" with the hot zone during the growth (does not precipitate out with the growing crystal). This technique is ideal for incongruent melters. Practically, this can be achieved by adding a small pellet of the intended flux on the end of one of the polycrystalline rods and joining them very carefully, shown in Figure 2.1.2. The molten zone of this crystal growth technique is both incredibly sensitive and particularly influential on the growth results. Changes in the molten zone composition affect a number of factors, primarily its melting point, potentially rendering the molten zone unstable, but also the rates of feed rod solvation and seed rod crystal growth, and possibly even the phases present depending on the phase diagram. When unbalanced, these factors compound rather than self-correct, thus driving the molten zone further from stability. It is therefore imperative to chose the identity, volume, and molar ratio of a solvent or solvent mix carefully so that the composition of the molten zone does not change during the course of the growth. Moreover, a consistent molten zone composition is essential to obtain a high-purity crystal of the same stoichiometry as the feed rod. TSFZ can also be sensitive to growth rates, which must balance the rate at which the

feed rod melts and dissolves in the molten zone solution with the rate at which the crystal precipitates out [1, 2].

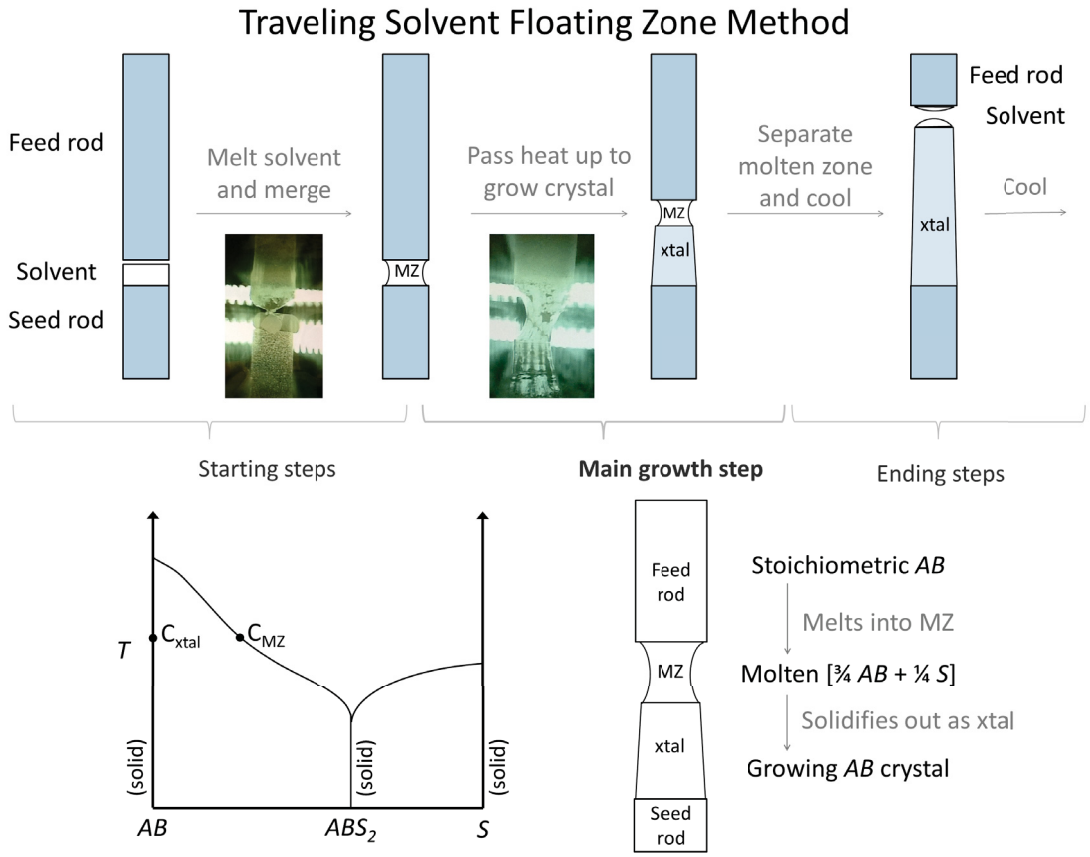

Figure 2.1.2: A graphic depicts relevant parts of the TSFZ technique. The top panel shows part of the traveling floating zone crystal growth method with images from a growth. The bottom panel details the sensitivity of the molten zone to composition for a hypothetical growth of compound *AB* with traveling solvent *S*. The molten zone is abbreviated "MZ" and crystal "xtal."

For the Tl_5Te_3 family crystals, the typical floating zone methods were not used. The optical furnace was used as a source of concentrated heat which can be slowly, steadily moved along the length of crystal growth, and a tapered fused quartz tube was used as a crucible similar to a Bridgman-type method. Bridgman method refers to the method of crystal growth in which a polycrystalline material is slowly pulled through a temperature gradient. Typically, this Bridgman process occurs horizontally in a multi-zone furnace with polycrystalline material in a tapered crucible which promotes the growth of a single crystal

grain.

In this "modified Bridgman" technique used to grow Tl_5Te_3 and similar compounds, polycrystalline material is held in a fused quartz ampoule which serves as the crucible. The quartz ampoule is outfitted with a slightly elongated, tapered bottom tip; like in the traditional Bridgman technique, the purpose of this acute angle is to encourage selection and growth of a single crystal seed. The growth therefore occurs from bottom to top. Empirically, it was found that a slight inert atmosphere in the quartz ampoule was preferable to vacuum, and that using fine granules of polycrystalline material minimized effects due to surface tension as compared to fully powder or pre-melted polycrystalline material.

This technique was developed for Tl_5Te_3 in conjunction with Seyed Koopayeh and used successfully to grow crystals of the Tl_5Te_3 family as well as Cd_3As_2. It is presented first in the publication of Tl_5Te_3's topological properties and described in detail in a review article [2, 3]. Further developments could examine in detail the effects of the quartz tube dimensions in addition to the aforementioned atmosphere and pressure within the ampoule and the form of the material, as well as the rotation and growth speeds. The latter two are general considerations of any chemical system when using optical furnace crystal growth. One factor that proved difficult to control was how the molten liquid's surface tension affected the crystal growth – this may be influenced by the inner diameter of the quartz tube as well as form and particle size of the polycrystalline material. The transfer and absorption of light is affected by the thickness and curvature of the quartz tube as well as the form and particle size of the polycrystalline material.

It was found that Tl_5Te_3 crystals grown by the modified Bridgman floating zone technique exhibited a slight gradient along the length of the growth. Tl_5Te_3 appears to exist over a phasewidth from stoichiometric (62.5% Tl) to Tl-rich (up to 65.5% Tl). Because the composition affects the physical properties such as the superconductivity (see Section 4.2 for more), it is desirable to avoid such a gradient in order to get pristine crystals. Therefore, for Tl_5Te_3 crystals, a small amount (1-5 mol%) of Te was used as a traveling solvent. Gran-

ules of pure elemental Te were placed at the bottom of the quartz ampoule before loading the appropriate Tl_5Te_3 granules, and the growth proceeded at usual from bottom to top. The Te flux is known to have traveled up the material with the molten zone because excess Te and TlTe is observed at the top of the resultant boules and some Te vaporization condenses on the sides of the ampoule above the boule. The technique of using a Te flux successfully produces single crystals of Tl_5Te_3 with no observable gradient along the growth length.

2.2 Diffraction as structural characterization

The most basic and the most important structural characterization technique is diffraction. Solids come in two general categories: glassy or amorphous materials, which have no long-range order, and crystalline materials, which have a repeating unit cell which, if translated, maps the entire material; the latter, the focus of this dissertation, may be characterized via diffraction analysis. Diffraction occurs when an incident probe beam (usually comprised of x-rays, neutrons, or electrons) diffracts off the planes of a crystalline material. The interference of the diffracted beams gives rise to a pattern of peaks, which may be collected by a detector. As the pattern results from the planes available, one can use the diffraction pattern to back out the geometry and symmetry of the unit cell which generated it.

A diffraction pattern is simply the interference pattern of the incident beam, which is composed of waves (x-rays) or accelerated wave-particles (electrons, neutrons). When the beam strikes a crystalline sample, different portions travel different paths, depending on how many layers deep each portion penetrates. The difference in the length traveled relative to the period of the wave gives rise to constructive and destructive interference. This relationship is described by Bragg's law, which states:

$$n\lambda = 2dsin\theta \tag{2.1}$$

where λ is the wavelength of the incident beam, θ the angle of the incident beam, d the

distance between diffracting planes, and n an integer. The righthand side of the equation describes the additional length traveled; the lefthand side is the criterion that this difference must be an integer multiple of the wavelength in order for constructive interference to occur.

The reason diffraction works on crystalline materials is evident from the d in Bragg's law: the translational symmetry of crystal gives rise to the repetition which is necessary to generate a sufficient number of planes to diffract. It is also possible for these planes to interfere destructively. Figure 2.2.1 shows the diffraction of a primitive "P" and a centered "I" (possessing an atom at the center – at (x, y) = (1/2,1/2) of this two-dimensional unit cell) unit cell which are otherwise identical. This central atom creates a second layer (Miller index 02) exactly between those created by the edge of the unit cells (Miller index 01). Incident waves diffracting off this central layer precisely destructively interfere with those diffracting off the layers created by the edges of the unit cell, and thus the peaks due to diffraction off of the (01) planes in the primitive unit cell are systematically absent in the diffraction pattern of the centered unit cell. In terms of d, the unit cell with a central atom has a layer space d_{I} which is half that of the same unit cell without it d_{P}: $d_{\mathrm{I}} = d_{\mathrm{P}}/2$. In this fashion, symmetry elements pose additional restrictions on diffraction conditions. These systematic absences (peaks which cannot be present due to the symmetries of the unit cell) can therefore identify the symmetries present in the unit cell.

While the positions of peaks are dictated by the unit cell symmetries as described above, the intensities of peaks depend on the scattering factors of the atoms in the unit cell. Scattering factors depend on the nature of the scattering force (described in Subsection 2.2.3), e.g., scaling with electronic density for x-rays, which are electromagnetic radiation. It is possible therefore to determine the amount of an atom, or the ratio of atoms, at a site due to its peak intensity.

The diffraction intensities and pattern discussed above are encompassed entirely by the scattering equation

$$F_{hkl} = \sum_{j=1}^{n} f_j e^{2\pi i(hx_j + ky_j + lz_j)} \tag{2.2}$$

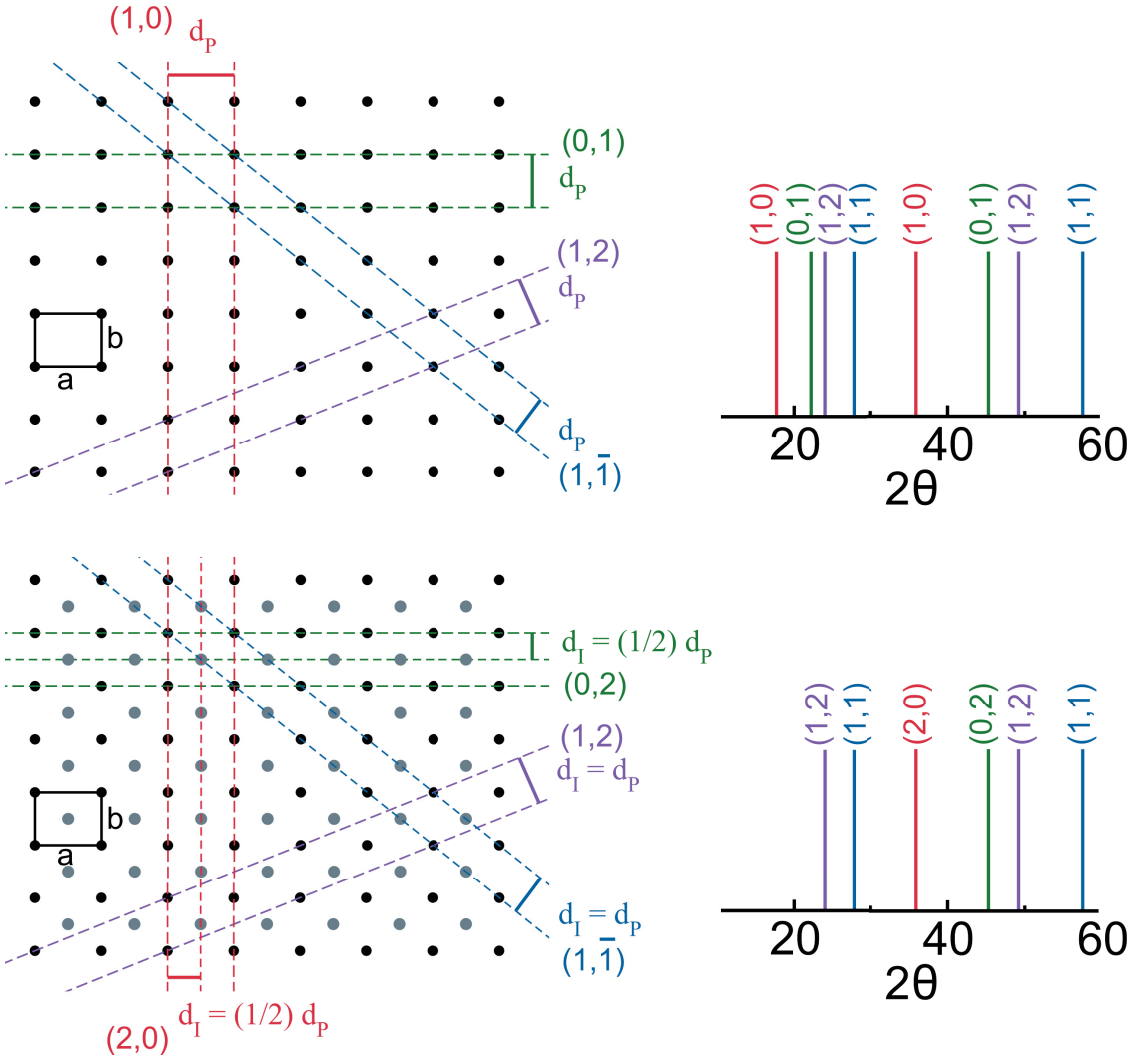

Figure 2.2.1: A graphic shows the how the symmetry of a material can affect the planes present, and thus the resultant diffraction pattern. The top panel illustrates a two-dimensional, primitive ("P") orthorhombic unit cell ($a > b$, angle = 90°) with several planes labeled and the expected diffraction pattern for that material (assuming $\lambda = 1.54$ Å), and the bottom panel show the same for a centered ("I") unit cell. Note the addition of an atom at the center inserts an additional plane in each of the a and b directions. The destructive interference created by these inserted planes removes diffraction peaks ("systematic absences").

where F_{hkl} is the square root of the scattering intensity, j is an atom located at (x_j, y_j, z_j), and f_j the scattering factor of atom j.

Diffraction data may be collected on either single crystals or on powder data. Single crystals generate a single peak in three-dimensional space for each diffraction plane, Poly-

crystalline powders are composed of a large number of randomly aligned crystallites, and thus what was a single spot of for a single crystal is a cone at the given collection angle for powder sample. Data collection for a powder can therefore be taken along a single arc, generating a plot of diffraction intensity as a function of diffraction angle; whereas data collection for a single crystal involved taking an array of images in three dimensional arrangements and extracting a sets of intensity and position from the spots on the images. Both sample and experimental preparation for powder diffraction is more simple and efficient than for single crystal. The diffraction patterns presented in this dissertation are typically from powder data.

2.2.1 Powder diffraction analysis

The lattice parameters of the unit cell and its symmetry class can be derived directly from a diffraction pattern by peak indexing, the process of assigning peaks to reflection indices. Once the lattice parameters and symmetry class have been determined from the peak positions, the identities of the constituent atoms and their positions may be estimated through simulated annealing, a computational process which tests the energy of a number of configurations. In practice, the combination of peak indexing and simulated annealing can be time- and resource-consuming. Databases of known structures with calculated and experimental diffraction patterns exist for comparison of diffraction data; it is much more expedient to match diffraction patterns of known compounds to such a database. For an unknown compound, these databases can suggest structural prototypes as an initial approximation of the structure.

From an initial ansatz of the complete unit cell (both lattice parameter and atom identity and positions), a process called Rietveld refinement can yield an improved unit cell. Rietveld refinement is a method of repeatedly refining a model of the unit cell to the diffraction data. The simulated diffraction pattern is generated from the model, and the free parameters are optimize to minimize the difference between the simulated diffraction

pattern and the data. The user can adjust which parameters (both those due to experimental conditions and those in the structural model) to refine freely or in a constrained manner, or to remain fixed. Constraints might include limits (e.g., the physically sensible minimum of 0 for atomic thermal parameters) or relationships between parameters (e.g., fixing the total occupancy of a mixed occupancy site). Judicious use of this method can yield an accurate picture of the complete unit cell of the sample to whose diffraction data the model is being refined.

Rietveld refinement comes with the caveat that parameters may convolute. Some of these potential correlations are transparent: for example, both the thermal parameter and the occupancy of the same site affect peak intensities, and so refining both at the same time can easily seesaw the refinement out of a local minimum. A fair amount of user sensibility and expertise is required to evaluate the accuracy, rather than statistical goodness, of a refinement. Practically, use of a silicon standard can prevent experimental parameters from convoluting with parameters based in the structural model. Silicon's lattice parameter is well characterized, so holding it constant provides a reference to refine the experimental parameters without allowing them to correlate with the model's lattice parameters.

2.2.2 Pair distribution function

Pair distribution function (PDF) analysis is a diffraction technique which returns a histogram of real-space atom-atom distances, with the peak intensities scaled by the scattering factor of the involved atoms (Figure 2.2.2). A pair distribution function is generated by a Fourier transform of diffraction data from inverse space to real space. This Fourier transform requires an excellently characterized background to high Q. Although there do exist laboratory instruments for PDF analysis, high-quality PDF facilities are typically found in specialized synchrotron or neutron facilities for these reasons.

Arguably the greatest unique advantage of PDF is the ability to discern local structure changes that are averaged out in long-range diffraction data. In the context of this disser-

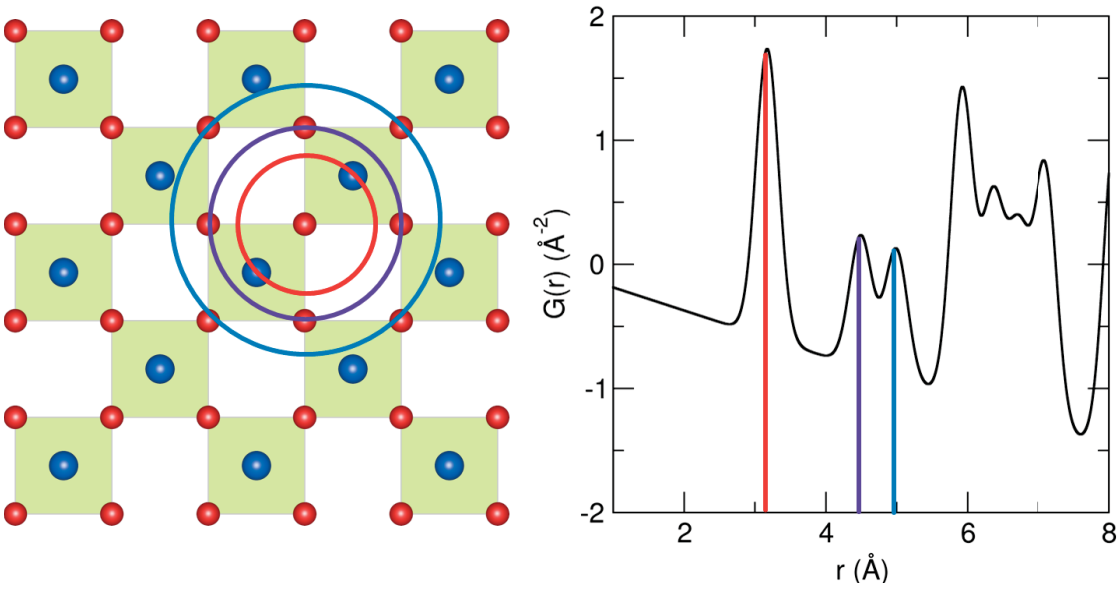

Figure 2.2.2: Representations of pair-distances in a structure and its PDF illustrates the physical information conveyed by the pair distribution function. On the left panel, a two-dimensional square lattice analogue of the perovskite structure is shown with specific pair-distances highlighted by colored circles. The simulated pair distribution function for this structure is shown on the right, with the corresponding pair-distances indicated by lines of the same colors. The two-dimensional structure is visualized in the VESTA program [4].

tation, high-resolution PDF data would perceive charge disproportionation as a bifurcation of short pair-distances (bonds) as the cations with higher and lower oxidation states should form shorter and longer bonds, respectively.

2.2.3 Types of radiation

Scattering conditions require the wavelength of the incident beam λ to be comparable to the distances between layers d which are diffracting it. Therefore, a number of waveparticles can be used as the incident beam, each with their own advantages and drawbacks. The most common types are x-rays (short-wave electromagnetic radiation), accelerated neutrons, and accelerated electrons. The last of these is not discussed in this dissertation.

X-rays, being short-wave electromagnetic radiation, interact with the electron density around atoms. This has three primary disadvantages: near impossibility of locating very

light elements, poor resolution between elements of similar Z numbers, and a decrease of diffraction signal with increasing angle. The first is a result of lighter atoms having fewer electrons and thus generating significantly less intense diffraction signal. This small signal (e.g., hydrogen has only a single electron) is hard to resolve, and can even be within the error of diffraction signal for materials with much heavier atoms. Similarly, diffraction off of electron density results in poor resolution between atoms of similar Z numbers the difference in their scattering factor is very small or even insignificant. X-ray diffraction is therefore not able to reliably distinguish substitution between elements with similar Z numbers based on peak intensity (N.B.: other aspects, such as bond length, may still prove useful). Finally, x-ray diffraction signal drops off as increasingly scattering angle increases due to the fact that the x-rays wavelengths (0.5 - 10 Å) are on the order of the electron density that is diffracting them, which results in Mie scattering rather than Raleigh scattering. The forward (incident angle θ close to 0 °) scattering remains at full intensity while the intensity of sideways/backwards scattering is decreased due to interference, effectively reducing scattering intensity as the incident beam angle angle increases.

In practice, laboratory x-ray diffraction is a common first step in characterizing crystalline materials used extensively in the research undertaken in this dissertation. Laboratory x-ray diffractometer (XRD) instruments are relatively inexpensive, do not require destruction of the sample, and are not time-consuming to prepare samples for or to undertake measurements on. Our laboratory XRD is outfitted with a copper x-ray source and produces primarily Cu K_α $\lambda = 1.54$ Å wavelength x-rays. The diffraction patterns shown in this dissertation sometimes have silicon added as an internal standard by which to better determine the target compound's experimental structure (see Subsection 2.2.1).

Synchrotron x-ray diffraction is also available at a number of national and private facilities. By accelerating the waveparticles in a large circle, a spectrum of energies is available (in contrast to the select few wavelengths available by copper or molybdenum tubes), which can then be selected as necessary by a monochromator or used collectively as white-light ra-

diation. Synchrotron radiation is far more intense than laboratory-based radiation sources. This combination of a narrower spread of wavelengths and high intensity allows excellent resolution and impurity detection limits. In this dissertation, synchrotron x-ray diffraction is used to look for small (low-intensity) peaks resulting from a potential minor distortion in Tl_5Te_3, and for Tl_5Se_3 samples to resolve the splitting of large peaks, to better refine the occupancies (from the relative intensities of peaks) and look for small peaks associated with a structural distortion.

In contrast to x-rays, neutrons are uncharged particles; they do no interact electromagnetically and instead diffract off of the nuclear weak force. This interection, which fundamentally differs from the one governing electron and x-ray diffraction, offers complementary advantages and disadvantages. One most notable advantage of the different type of interaction involved is the different atomic scattering factors which result. In x-ray and electron diffraction, which diffract Coulombically, scattering intensity scales with the number of electrons on the atom. In contrast, neutron scattering factor varies non-linearly with atomic number, even having negative scattering for some elements. Thus neutron diffraction is an ideal contrast to x-ray diffraction to detect lighter atoms such at hydrogen or differentiate between atoms of similar Z numbers. Another advantage of neutrons is that the scattering factor does not decrease with angle: by scattering off of nuclei rather than electronic density, the wavelength of the incident neutron beam is much larger than the size of the nuclei which diffract it, resulting in Raleigh scattering, which is constant over all angle because there is no interference.

The main disadvantages of neutron diffraction are that it requires a large amount of sample and travel to a specialized facility. By diffracting off the nuclei (which are comparatively very small) rather than electron density, neutrons interact weakly with matter. Due to this lesser interaction, a large amount of sample is needed. Neutron beams can be generated in one of two ways: a beam from a traditional nuclear reactor, or from a spallation source. The complexity of generating neutrons, especially in significant co-aligned

quantities, restricts their availability as a diffracting medium to centralized facilities. The low interaction with matter offers further challenges when constructing experimental apparati, as the weak interaction manifests as difficulty focusing neutron beams and building beamstops.

2.3 Measurement of physical properties

A driving force of materials discovery and design is the desired properties of the materials. In order to measure these properties, the McQueen lab relies primarily on a versatile piece of equipment by Quantum Design called the Physical Properties Measurement System (PPMS). This instrument is essentially a large, cold dewar with a solenoid of superconducting wire, and a chamber with 16 electrical pins at the bottom. This set-up allows the user to control both the environment and the property measured: the dewar and the solenoid moderate the temperature and field over large ranges, and different insets electrically connect the pins to either the sample or a measurement device in the inset in order to properly measure a desired property while the accompanying option correctly processes the signal into usable data. The atmosphere and pressure of the chamber can be controlled with vacuum pumps and helium gas vented in from the cryogenic cooling headspace.

2.3.1 Magnetization measurements

The Quantum Design PPMS has an option called the AC Measurement System (ACMS), which consists of an inset with a smaller detection coil around the sample, and a sample rod which holds the sample in the insert. The top of the sample rod is held by a servo motor, which can oscillate the sample up and down. This movement, coupled with the magnetic properties of the sample, creates a flux which is captured by the detection coils. The material's magnetic response may be determined from this flux. Both the temperature and applied magnetic field may be controlled. Generally a pressure of about 10 torr helium

atmosphere aids the sample in achieving the target temperatures relatively quickly. This instrument operates in Gaussian-cgs units, not SI units: applied field H in Oe, magnetization response M in emu, and $\lim_{H\to 0} = dM/dH = \chi_{\text{cgs}} = \chi_{\text{SI}}/(4\pi)$.

As discussed in Subsection 1.3.1, a superconductor rejects all applied magnetic fields when below critical temperature T_c and field H_c or H_{c1}. The Meissner effect occurs due to eddy currents at the surface which generate a magnetization response M that equals and opposes the applied field H, thus the magnetic susceptibility of a simple, pure superconductor below T_c should be flat at $\chi_{\text{SI}} = 4\pi\chi_{\text{cgs}} = -1$. This effect can be observed using the ACMS inset by applying a field and measuring the sample's magnetic response as a function of temperature. For reliable determination of bulk superconductivity, the applied field should be small in order to not potentially exceed H_{c1}. Measurements on a sample when cooled under zero field and when cooled under non-zero field provide lower and upper bounds of bulk superconducting volume fraction respectively. Field-cooled measurements provide a lower bound because any impurity defects present can fix the applied field before the sample enters a superconducting regime, thereby lowering the apparent superconducting fraction. Zero-field-cooled measurements provide an upper bound because good metals also generate eddy currents opposing the applied field when subjected to the same experimental procedure, so any metal impurities present would behave in the same manner as superconducting material, therefore increasing the apparent superconducting fraction.

The critical fields of superconductors may be determined by measuring the magnetic response as a function of applied field, as illustrated in Figure 1.3.1. Below H_c or H_{c1} for type I and II superconductors respectively, the material should be in a full Meissner state characterized by the magnetic response (the internally generated magnetic field) responding linearly with the magnitude of the applied field. At fields above H_c for a type I superconductor, the magnetic response should drop in magnitude immediately near to zero. For a type II superconductor, the magnetic response should begin to decrease in magnitude at fields above H_{c1}, but persist until H_{c2} is reached as a mixed state exists for fields

intermediate to the two critical fields.

When considering the magnetization measurements, one must account for the shape of sample geometry. Due to the material's magnetic response M, the experienced "internal field" H_{int} differs from the applied "external field" H_{ext} as a function of direction (i) and geometry: $H_{\text{int},i} = H_{\text{ext},i} - N_i M_i$ [5]. Demagnetization factors N, where $0 \leq N \leq 1$, account for this discrepancy. Normalization requires the sum of all the geometrically normal directions must be 1 ($N_x + N_y + N_z = 1$): therefore for a cube or sphere, $N_i = 1/3$; for a two dimensional object such as a flat disc or a superconducting plane, $N_\perp \approx 1$ and $N_\parallel \approx 0$; for a one dimensional object such as a rod, $N_\perp \approx 0$ and $N_\parallel \approx 1$. [5]

Magnetization measurements, as the name implies, are uniquely adept at characterizing magnetic materials. Magnetization data as a function of temperature permits a Curie-Weiss analysis in the paramagnetic regime (temperatures at which the thermal energy surpasses the magnetic interactions). The Curie-Weiss law is:

$$\chi = \frac{C}{T - \theta} + \chi_0 \tag{2.3}$$

where C is the Curie constant, a measure of the effective magnetic moment of the magnetic ions; θ is the Weiss temperature, a measure of the predominant magnetic interaction; and χ_0 a temperature-independent contribution. This relationship may be linearized and fit to data:

$$\frac{1}{\chi - \chi_0} = \frac{1}{C} - \frac{\theta}{C}. \tag{2.4}$$

This analysis determines the alignment and strength of the average, dominant magnetic interaction by means of the Weiss temperatue θ (also known as the Curie-Weiss temperature) and effective magnetic moment, which is included in the Curie constant, for simple magnetic materials. Note that the Weiss temperature is a unit of energy not temperature; negative Weiss temperature indicate a net antiferromagnetic interaction.

2.3.2 Heat capacity

Heat capacity is defined at the amount of heat it takes to raise the temperature of a material: $C \equiv \delta Q/dT$. The heat energy transfered to the material goes into vibrations (phonon modes), electrical behavior, and phase transitions. Therefore, heat capacity is a measurement of energy that can discern phase transitions. Moreover, as will be explained below, entropy may be calculated from heat capacity.

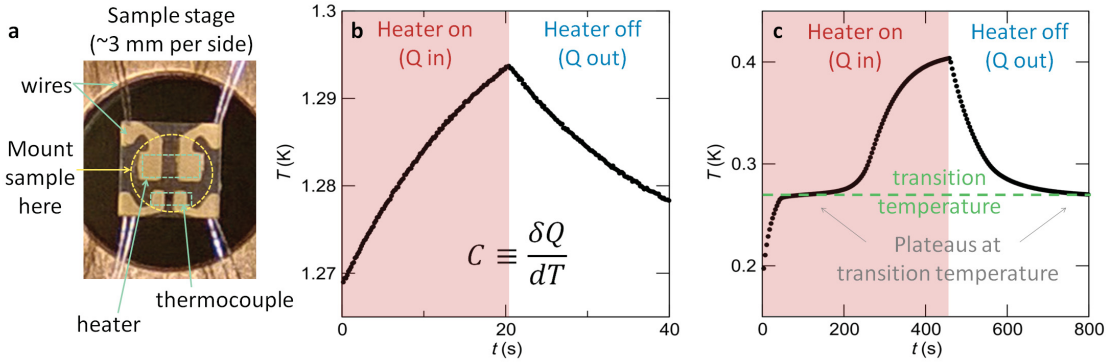

Figure 2.3.1: (a) The sample stage of a Quantum Design PPMS heat capacity option insert puck is shown with relevant physical aspects labeled. (b) The heating trace for a heat pulse of the typical semiadiabtic technique is shown; C_p is extracted from fits to the heating and cooling curves. (c) The heating trace for a large heat pulse used in the "large heat pulse" data collection shows plateaus at the transition temperature of a first order transition with large latent heat.

The heat capacity inset for the PPMS is composed of a sample stage with a heater and a thermocouple, shown in Figure 2.3.2(a). Suspending the sample stage in space by only the necessary wires isolates it from the thermal mass of the inset and greater instrument. The sample stage is further isolated by high vacuum and baffle. The heat capacity of the sample stage with a small amount of thermal grease but no sample, called the addenda, is collected prior to collecting data on the same set-up with the sample. The sample is then thermally paired with the sample stage via the thermal grease and a measurement of the sample-stage unit is taken. A "flake" or disc (flat, wide, low, and even/smooth) sample shape is preferred so that the sample thermally equilibrates quickly and evenly. After measuring heat capacity on the sample-stage unit, the addenda dataset may be subtracted to isolate the heat capacity

of the sample only.

During data collection, the heater provides heat pulses to the sample-stage unit while the temperature of the sample-stage unit is measured by the thermocouple. (Note the heat pulses are only applied to the sample-stage unit; the PPMS instrument is kept at temperature.) The graph in Figure 2.3.2(b) and (c) shows the heating curve of such a heat pulse: in the red shaded portions, the heater is on and actively applying a heat pulse, and the temperature of the sample-stage unit increases; in the white portions, the heater has shut off and the sample-stage unit is decreasing in temperature as the heat dissipates. Typically, small "semiadiabatic" heat pulses no more than 1-3% heat rise is applied and C_p is assumed to be constant over a single short measurement, as is the case for Figure 2.3.2(b). A 2τ heat flow model is fit to both the heating and cooling portions of these curves, and C_p may be extracted from the 2τ heat flow model.

In Chapter 8, a large heat pulse method is also used in order to better capture the large latent heat of $Yb_2Ti_2O_7$'s first order transition. A heating and cooling trace of this method taken on $Yb_2Ti_2O_7$ is shown in Figure 2.3.2(c): there is a plateau at the transition temperature due to the absorption of latent heat associated with the transition. In this "large pulse" method, a larger heat pulse (100-200% or 0.150-0.200 K heat rise Chapter 8) which cannot be assumed to be adiabatic is applied in order to surpass the latent heat of a first order transition. The assumption that C_p remains constant over the course of the entire measurement is removed; instead, C_p is assumed to have distinct, constant values in a series of δT bins. The basic assumption, that for 1-3% heat rise, C_p may be assumed to be constant, therefore is the same for both methods. Because the large heat pulse repeatedly transverses the entire heat capacity peak, it is less likely to be affected by hysteresis than semiadiabatic measurements, which do not supply enough heat per measurement to cross the first order phase transition.

The PPMS gathers constant-pressure heat capacity data (C_p) rather than constant-volume (C_v), as the latter is experimentally unfeasible for small, solid samples. The two are related

strictly by

$$C_p - C_v = \frac{V\beta^2}{\kappa_T}T = \frac{\left(\frac{\partial V}{\partial T}\right)_P}{\left(\frac{-\partial V}{\partial P}\right)_T}T \tag{2.5}$$

where β is the volume expansion coefficient and κ_T is the isothermal compressibility [6]. At temperatures below ~30 K, there is only negligible difference between the two measures of heat capacity: typically, $\frac{C_p - Cv}{C_p} \leq 0.1\%$ for temperatures up to $\theta_D/6$, 1% for temperatures up to $\theta_D/3$, and 10% at the melting point [6]. Most heat capacity measurements used in this research are well below the temperatures at which the two measures differ appreciably, and so no conversion is applied. Therefore no delineation is indicated between the two in chapters other than this one.

At low temperatures, the heat capacity can be approximated by

$$\begin{aligned} C_v &= \gamma T + \beta_3 T^3 + \beta_5 T^5 + ... \\ C_v &\approx \gamma T + \beta_3 T^3 \end{aligned} \tag{2.6}$$

where γT term describes the electronic contribution (γ is the Sommerfeld coefficient) and $\beta_3 T^3 + \beta_5 T^5 + ...$ describes the phononic contribution of the lattice [6]. The lattice heat capacity has been described by the Einstein and Debye models, the former of which assumes the lattice to be a collection of independent quantum harmonic oscillators (and thus can describe localized phonon modes), and the latter which assumes collective phonons as a classical continuum of states (and thus can describe phonon modes delocalized over the entire crystallite). Fully expressed, these models give the expressions

$$C_{v,\text{Einstein}} = 3R\sigma_E \left(\frac{\theta_E}{T}\right)^2 \frac{e^{\theta_E/T}}{[e^{\theta_E/T} - 1]^2} \tag{2.7}$$

and

$$C_{v,\text{Debye}} = 9R\sigma_D \left(\frac{T}{\theta_D}\right)^3 \int_{0\text{ K}}^{\theta_D/T} \frac{x^4 e^x}{(e^x - 1)^2} dx \tag{2.8}$$

where the Einstein and Debye temperature are defined as $\theta_E = (\hbar\omega_E/k_B)$ and $\theta_D = (\hbar\omega_D/k_B)$ [6]. Plotting the heat capacity as C/T^3 vs. lnT permits easy visualization and separation of the Einstein and Debye modes [7], shown in Figure 2.3.2.

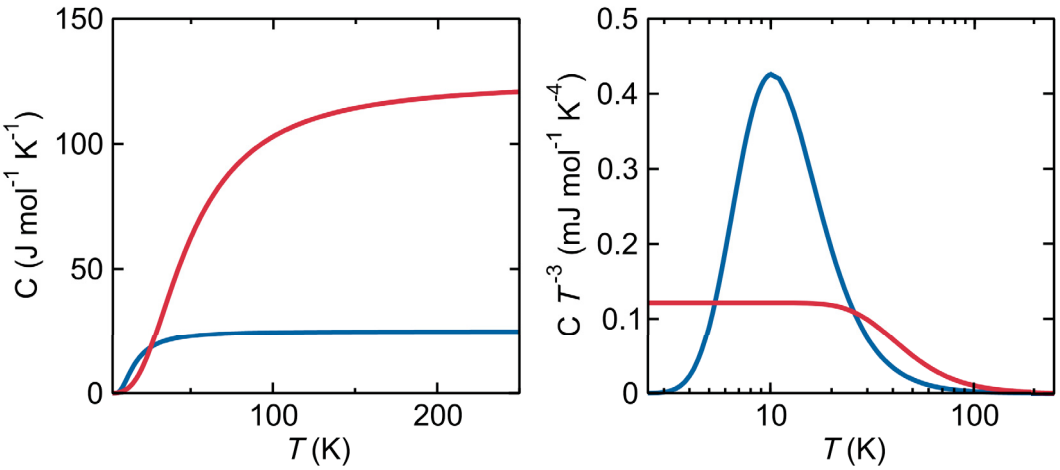

Figure 2.3.2: Plotting heat capacity as C/T^3 vs. lnT allows the Einstein (blue curves) and Debye modes (red curves) to be easily identified by a peak and plateau, respectively.

Heat capacity is intimately related to entropy, which is

$$S = \int_{0\,\mathrm{K}}^{T} \frac{C}{T} dT. \tag{2.9}$$

The change in entropy may be calculated from heat capacity data. In Chapter 8, the heat capacity was measured to very low temperatures, nearly absolute zero. In this situation, the total magnetic entropy S was calculated (rather than the change in magnetic entropy, ΔS) by assuming that $C(T = 0\ K) = 0$ and integrating the electronic heat capacity from absolute zero. As entropy is also defined by the number of microstates ($S = k_B ln\Omega$), the results from this analysis can determine the degeneracy of the ground state. Pauling calculated the ground state magnetic entropy of a spin ice to be $S = (3/2)Rln2$; and therefore no more than $S = Rln2 - (3/2)Rln2$ can be recovered. The term $S = Rln2$ is the two-state entropy due to two spin states (spin up and spin down): for a mole (N_A) of electron spins which can

each be in a spin-up or -down state, $S = k_B ln(2^{N_A}) = Rln2$.

In Chapters 4 and 6, the precise superconducting temperatures T_c are calculated through entropy. Thermodynamic quantities provide a more robust determination of the bulk superconducting critical temperature than magnetization measurements because impurities and sample inhomogeneity can result in multiple drops in the magnetization. An "equal-entropy construction" plots the electronic specific heat over temperature (C_{el}/T) as a function of temperature. These axes allow visualization of entropy associated with the transition between the normal and superconducting states as the integral (the area under the curve). The electronic specific heat may be isolated using a fit to the low-temperature approximation given in Equation 2.6; for a normal state, $C_{el}/T = \gamma$ should be a straight horizontal line in the equal entropy plot. The transition between the normal and superconducting states occurs as a sharp increase in C_{el}/T at the transition, then C_{el}/T decreases sharply below the transiton temperature. (Thermodynamically, there is an immediate entropic cost to the transition, but a net decrease in entropy when considering the full range of superconducting temperatures.) In reality, this initial increase occurs over some small but discrete range of temperatures: an "equal entropy" construction defines the precise temperature as that temperature corresponding to exactly half of the initial entropic cost of the transition.

2.4 Angle-resolved photoelectron spectroscopy

Angle-resolved photoelectron spectroscopy (ARPES) is the primary experimental technique to verify a candidate topological insulator (or to observe topological surface states in non-insulating materials). Photoelectron spectroscopy is based on the photoelectric effect, the process of incident photons ejecting electrons from a surface. The relative energies of the incident photon and ejected electron reveals the work function of a material: $KE_{\text{electron}} = h\nu_{\text{photon}} - \varphi$, where φ is the work function, the energy required to dislocate an electron from the structure. This is a measure of how far below the Fermi level the state or

band is in energy.

Angle-resolved photoelectron spectroscopy separates data by real-space angle. When performed on single cyrstal in a known orientation, the data resolved by real-space angle yields data resolved by momentum k in the Brillouin zone through a Fourier transform. The technique therefore can map the band structure below the Fermi level. Because this is a surface measurement, this technique measures the the two-dimensional surface Brillouin zone projection (2DBZ) of the three-dimensional bulk Brillouin zone.

ARPES is an experimentally non-trivial technique to perform. It requires a single crystal which must be exposed in situ, generally by cleaving, because the technique is highly surface sensitive. Therefore this technique is costly in terms of time and labor to make, orient, and properly cut several crystal samples; moreover, exposing a new face via cleaving or ablation is a destructive technique which renders the remains of the crystal less useful for other measurements. Additionally, ARPES experimental set-ups are relatively uncommon: the technique requires an intense source of monochromatic light at low temperature, and so the best data is collected at synchrotron facilities. Higher energy ultraviolet light is necessary to map more energies below the Fermi level (which is particularly relevant for the initial and current topological materials candidates, which have Dirac cones energetically displaced from the Fermi level), and until recently, lasers in this range lacked sufficient flux to generate results of acceptable quality.

2.5 Computational methods

It is highly desirable to map the band structure of a compound, as it reveals not only the compound's overt physical properties (metal, insulator, or semiconductor; direct or indirect bandgap) but also the energy as a function of crystal momentum (essentially as a function of symmetry direction). However, as ARPES hints, experimental mapping of the band structure is generally limited to the near-Fermi level range, and data as a function of crystalline

momentum requires oriented single crystals, which can be extremely time-consuming to produce.

As an alternative to experimental data, an array of computational methods have been developed to model chemical bonding. However, the most accurate of these, based on the wavefunctions themselves, are incredibly computationally expensive. Modeling a discrete observable, such as electron density, requires considerably less computation: density function theory (DFT) is a computational method which computes band structures by modeling electron density as a function of spatial position. An advantage of basing computations on an observable is that empirical parameters obtained from experiment may be readily incorporated to improve the results of the computational method.

Chapters 5 and 6 presents band structures of potential topologically non-trivial materials. These band structures were calculated by DFT using the basis set FP-LAPW-LO, or "full potential linearized augmented plane wave plus local orbitals." This is the most complete DFT basis set available. "Full potential" signifies that the electronic density depends on all three spherical coordinates; "linearized augmented plane wave" indicates the functions are a linear combination of delocalized plane waves with the addition of non-plane wave options; and "local orbitals" allows the parity of a band to be determined.

Bibliography

[1] S. M. Koohpayeh, D. Fort, and J. S. Abell, Prog. Cryst. Growth Charact. Mater. **54**, 121 (2008).

[2] S.M. Koohpayeh, Prog. Cryst. Growth Charact. Mater. **62**, 22 (2016).

[3] K. E. Arpino, D. C. Wallace, Y. F. Nie, T. Birol, P. D. C. King, S. Chatterjee, M. Uchida, S. M. Koohpayeh, J.-J. Wen, C. J. Fennie, K. M. Shen, and T. M. McQueen, Phys. Rev. Lett. **112**, 017002 (2014).

[4] K. Momma and F. Izumi, J. Appl. Cryst. **44**, 1272 (2011).

[5] C. P. Poole, H. A. Farach, and R. J. Creswick, *Superconductivitiy* (Academic Press, San Diego, 1995).

[6] A. Tari, *The Specific Heat of Matter at Low Temperatures* (Imperial College Press, London, 2003), p. 270.

[7] A. P. Ramirez and G. R. Kowach, Phys. Rev. Lett. **80**, 4903 (1988).

3 Structure of Tl_5Te_3

The following chapter discusses the structure of Tl_5Te_3 including bonding, symmetry, and oxidation states. An unexpected charge of Tl^{2+} is found and the potential for charge disproportionation is discussed and evaluated. Structural data including laboratory x-ray powder diffraction, single crystal diffraction, high-resolution diffraction data, and neutron pair distribution data is presented. Structural themes introduced in this chapter will be relevant for the doped series presented in Chapters 6 and 7 as well as the physical properties, presented for Tl_5Te_3 in Chapters 4 and 5.

3.1 Methods

Polycrystalline Tl_5Te_3 samples were prepared by heating elemental Tl (Strem Chemicals, 99.9%) and Te (Alfa Aesar, 99.999+%) in a vacuum-sealed silica ampoule to 550°C, holding for 24 h, followed by either furnace cooling or controlled slow cooling. Elemental thallium was stored and handled in an inert atmosphere to prevent oxidization. Tellurium was purified by self-vapor transport and using an oxygen getter prior to use. Once synthesized, Tl_5Te_3 appears to be stable in air, as determined by laboratory XRD patterns as a function of exposure time. Experiments were therefore performed in air when relevant, though sample were stored long-term in an argon-filled glovebox to minimize any surface oxidation. Laboratory diffraction measurements were conducted under ambient conditions. Samples used in synchrotron and neutron beam lines were packed under air and taken at

the temperatures indicated.

3.2 Reported structure of Tl_5Te_3 and discussion

Tl_5Te_3 is a part of a large group of around forty binary tetragonal M_5X_3 compounds, known by the prototypical Cr_5Bi_3 structure type [1, 2]. The structure type is better understood as $M(1)M(2)_2X(1)X(2)_2$, where M(1) and X(2) exist in the *a*-*b* plane, the X(2) atoms stack above the M(1) atoms, and the M(2) atoms occur in the space between the X(1) and M(1)/X(2) layers [1, 3]. These compounds typically have spacegroup $I4/mcm$ [1]. Böttcher et al. note that this structural family ought to be divided into two subgroups on the basis of *c*/*a* ratio: the major subfamily, "Cr_5Bi_3", has a larger *c*/*a* ratio of about 1.85, while compounds with a smaller ratio of $c/a \approx$ 1.4-1.5 belong to the smaller "In_5Bi_3" subfamily [1]. The latter consists only of binary compounds In_5X_3 and ($c/a \approx$ 1.48-1.49) where X = Bi or Sb and Tl_5Ch_3 ($c/a \approx$ 1.41-1.42) where Ch = Te or Se, along with tertiary derivatives thereof.

This *c*/*a* ratio is notable because, while the bonding in the *a*-*b* plane is not greatly affected, smaller *c*/*a* ratios compress the unit cell uniaxially along the *c* axis. This compression introduces a chain of axial $M(1)$-$X(1)$ bonds; in Tl_5Te_3, the closest interionic distance is that of Tl-Te chains along the *c* axis. This compression therefore creates a three-dimensional bonding structure: the M(1) Tl atoms are bonded to the X(1) Te atoms along the *c* axis (bond length $\approx$ 3.15 Å) and to the X(2) Te atoms perpendicularly in the *a*-*b* plane (bond length $\approx$ 3.35 Å). This basic $TlTe_3$ framework can be described as a network of edge-sharing, tilted $TlTe_6$ octahedra compressed along the *c* direction. The empty cavities between octahedra are occupied by the M(2) Tl atoms. This lattice of octahedra corner-sharing in three dimensions with interstitial atoms is structurally analogous to a perovskite $[Tl_4]TlTe_3$. Perovskites are a large materials class with stoichiometry ABX_3, where A and B are generally metals and X is typically oxygen or a chalogen, though notable exceptions

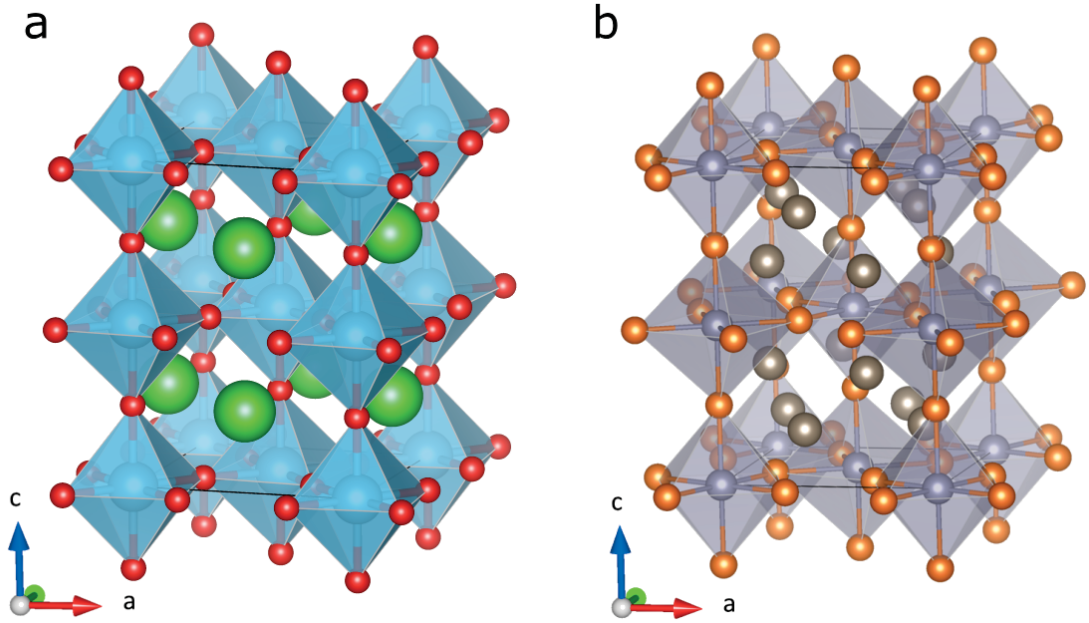

Figure 3.2.1: Structures of (a) a distorted perovskite $SrTiO_3$ [4] and (b) Tl_5Te_3. In (a), the green, blue, and red atoms are strontium, titanium, and oxygen respectively. In (b), the orange atoms are tellurium, the gray atoms in the cavities are M(2) thallium atoms, and the purple atoms at the octahedral centers are M(1) thallium atoms. Structures are visualized in the VESTA program [5].

exist. Structurally, peroskites consists of chains of corner-sharing BX_6 octahedra extending in three dimensions to form a BX_3 lattice which hosts A ions in the cavities between the octahedra. While the ideal perovskite stucture is cubic, perovskite material are commonly distorted by tilting or rotating the octahedra. Figure 3.2.1 compares the structures of Tl_5Te_3 and distorted perovskite $SrTiO_3$. The perovskite-style tilting of both is described in Glazer notation [8] as $a^0a^0c^-$: the letters indicate the lattice parameters (here aac due to a tetragonal structure), and the superscripts denote whether there is tilting about that axis (0 indicates no rotation, + indicates rotation that is the same for all layers perpendicular to that axis, - indicates rotation which alternates in consecutive layers along that axis). Tl_5Te_3 has alternating octahedral rotations of 20.1° about the c axis. Note that these alternating rotations are necessary to accommodate the geometry of the interstitial M(2) Tl atoms.

One can envision the arrangement of the M(2) Tl atoms in the octahedral cavities in a

number of ways:

1. As Tl_8 cubes, each cube encompassing a $TlTe_6$ octahedron. Each face of the Tl_8 cube frames a Te vertex of the $TlTe_6$ octahedron. These cubes are edge-sharing in the *a*-*b* plane and separated along the *c* axis. As the octahedra are rotated alternately along the *c* axis, so are the Tl_8 cubes.

2. As compressed, edge-sharing Tl_8 antiprisms between octahedra in the *c* direction. These antiprisms are compressed along the *c* axis and edge-sharing in the *a*-*b* plane. At their center is a M(1) Te atom.

3. As self-contained Tl_4 tetrahedra, one tetrahedron occupying each *A*-site of the traditional ABX_3 perovskite structure. These Tl_4 tetrahedra are a conceptual construct rather than an accurate description of the bonding environment: the tetrahedra's "bonds" (interatomic distance $\sim$3.5 Å) in the *a*-*b* plane actually correspond to an anti-bonding orbital.

4. As Tl-Te-Te chevrons composed of two M(2) Tl atoms and one M(2) Te atom, each extending off the *a*-*b* Te vertices of the $TlTe_6$ octahedra. As the octahedra are alternately rotated along the *c* axis, the chevrons point in alternate directions (e.g., clockwise about one octahedra, then counterclockwise about the next). The distances in these chevrons correspond with actual bond distances of $\sim$3.15 Å.

Methods 1 and 2 connect to the structural view of the greater Cr_5Bi_3 family and appeal to the geometrically minded; method 3 is a convenient if simplistic view; method 4 is most authentic to the actual bonding.

For consistency, this dissertation shall use the terms "octahedral centers" to refer to the M(1) Tl or substituant atoms, "axial" tellurium/chalcogen for the X(1) Te or substituant atoms, "equatorial" tellurium/chalcogen for the X(2) Te or substituant atoms, and "interstitial" or "Tl_4 clusters" for the M(2) Tl atoms in the Tl_5Te_3 compound and its derivatives.

3.2.1 Charge disproporionation and symmetry implications

Assigning a formal oxidation state of 2- to all tellurium atoms means that the five thallium atoms must share a total +6 charge, which can be decomposed into four Tl ions with formal charge 1+ and one Tl ion with formal charge 2+. A logical assignment of these formal oxidation states would be that the four interstitial Tl ions (the four M(2) ions) bear the 1+ charge while the Tl ion at the octahedral centers (the lone M(1) ion) bears the 2+ charge; this assignment of charges is supported by the symmetries which make the four interstitial Tl ions equivalent but separate from the one Tl ion at the octahedral centers. Nordell and Miller observed in their calculated density of states that the M(2) thalliums had more states lower in energy than the M(1) thalliums, which they note supports charge assignments of 1+ and 2+, respectively [2]. These formal oxidation states are also supported by the closest bonds observed in Tl_5Te_3: the Tl_2Te chevrons between interstitial Tl and the equatorial Te corresponds with each interstitial Tl having formal oxidation state 1+ and the equatorial Te having formal oxidation state 2-, and the TlTe chains extending along the *c* axis corresponds with the Tl at the octahedral centers having formal oxidation state 2+ and axial Te having formal oxidation state 2-. Bond-valence sums analysis consistently produces a higher charge for the octahedral Tl site than for the interstitial site. The range of possible tertiary derivatives provides further evidence for a 2+ formal charge on the octahedral site: compounds having stoichiometry $M Tl_4Te_3$ ($[Tl_4]MTe_3$) and $M Tl_9Te_6$ ($[Tl_4](M_{0.5}Tl_{0.5})Te_3$) are reported to exist only for 2+ (e.g., Sn and Pb) and 3+ (e.g., Bi and Sb) metal ions respectively [6].

It is surprising to observe a formal charge of 2+ on Tl because Tl^{2+} is a negative Hubbard-U ion prone to charge disproportionation. Chemically, the 2+ ($[Xe]s^1$) oxidation state is energetically unfavored relative to a mix of the 1+ ($[Xe]s^2$) and 3+ ($[Xe]s^0$) oxidation states: the half-filled *s* shell is less stable than either a completely full or empty one. Such relatively unstable ions tend to spontaneously charge disproportionate to the two more stable ions with an overall combined charge that satisfies the formal oxidation state.

In extended solids, this spontaneous pairing of electrons frequently gives rise to a charge density wave (CDW) in which the two more stable charges order in a fashion that is coherent on long-range scales. For example, $BaBiO_3$ is a distorted perovskite which has Bi^{4+}, an ion liable to charge disproportionation, at the octahedral *B*-site. (Similar to Tl^{2+}, Bi^{4+} charge disproportionates 3+ ([Xe]s^2) and 5+ ([Xe]s^0) oxidation states.) In $BaBiO_3$, charge disproportionation of the Bi octahedral centers causes alternatively smaller and larger octahedra having Bi^{3+} and Bi^{5+} at the octahedral centers respectively, giving rise to a classic charge density wave and a long-range pattern detectable by diffraction measurements. The literature is uncertain whether such a charge-ordered state exists in Tl_5Te_3.

After some early debate, Tl_5Te_3 has generally been agreed to belong to the *I*4/*mcm* spacegroup [1, 3]. Initially, the potential spacegroups included $I\bar{4}$ [9], *I*4/*m* [10], and *I*4/*mcm* [11, 12]. The latter two are nearly identical, with only an additional glide plane in the *I*4/*mcm* spacegroup which is absent from the *I*4/*m*. This glide plane imposes the condition that all octahedra must be symmetry equivalent. It is not possible for all octahedra to be equivalent if the octahedral centers charge disproportionate, as differently charged ions should have larger (Tl^{1+}) and smaller (Tl^{3+}) coordination spheres. The structural changes due to charge disproportionation can be accommodated through alternating octahedral sizes and/or by octahedral rotation on a long-range or local scale. It is therefore of interest to investigate the structure of Tl_5Te_3 thoroughly to confirm the presence of unexpected Tl^{2+} ions in this compound.

3.3 X-ray diffraction of Tl_5Te_3

In-house laboratory diffraction data of a sample of stoichiometric Tl_5Te_3 is shown in Figure 3.3.1. No violation of the *I*4/*mcm* symmetry is observed. The "Tl_5Te_3" compound appears to exists over a small range of compositions: structures with 62.5 atomic% thallium (stoichiometric Tl_5Te_3) to about 65 atomic% thallium can be targeted and form without

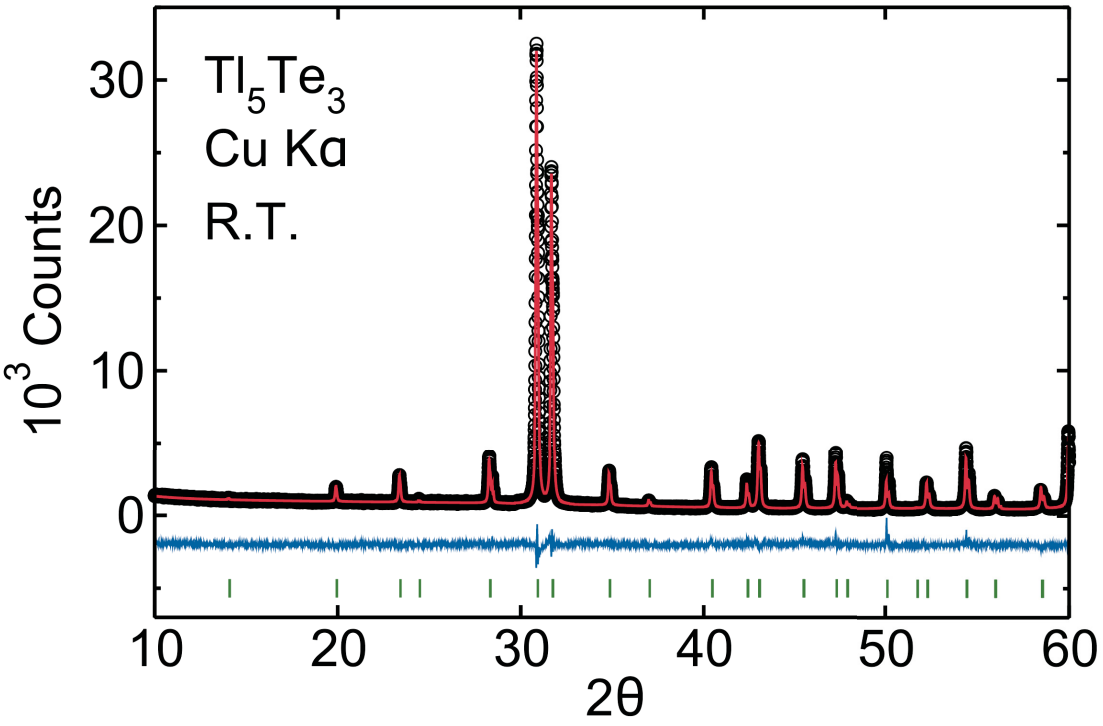

Figure 3.3.1: Laboratory XRD data taken on Tl_5Te_3 is well fit by the *I*4/*mcm* space-group. The difference between the data (black circles) and modeled fit (red line) is given as a blue line. Green tic marks denote allowed reflections.

Table 3.3.1: List of experiential Tl_5Te_3 lattice parameters as a function to atomic percent thallium.

Atomic % Tl	*a* **(Å)**	*c* **(Å)**	**c/a**	**unit cell volume (Å^3)**
62.5	8.92457	12.61159	1.413131389	1004.487286
65.5	8.954849	12.6114182	1.408333988	1011.301057

side products or any observable breaking of symmetry. We present our data in Table 3.3.1. This broadened phasewidth has been previously noted [3, 11, 13] and its implications on structure thoroughly investigated by Joubert and Feutelais [11].

Single crystal x-ray diffraction data on a small crystal of Tl_5Te_3 as a whole is well fit by the *I*4/*mcm* spacegroup. However, close examination of the precession images show faint signals which violate the systematic absences imposed by the glide plane symmetry element of spacegroup *I*4/*mcm*. Specifically, Figure 3.3.2 shows the 0*kl* diffraction image

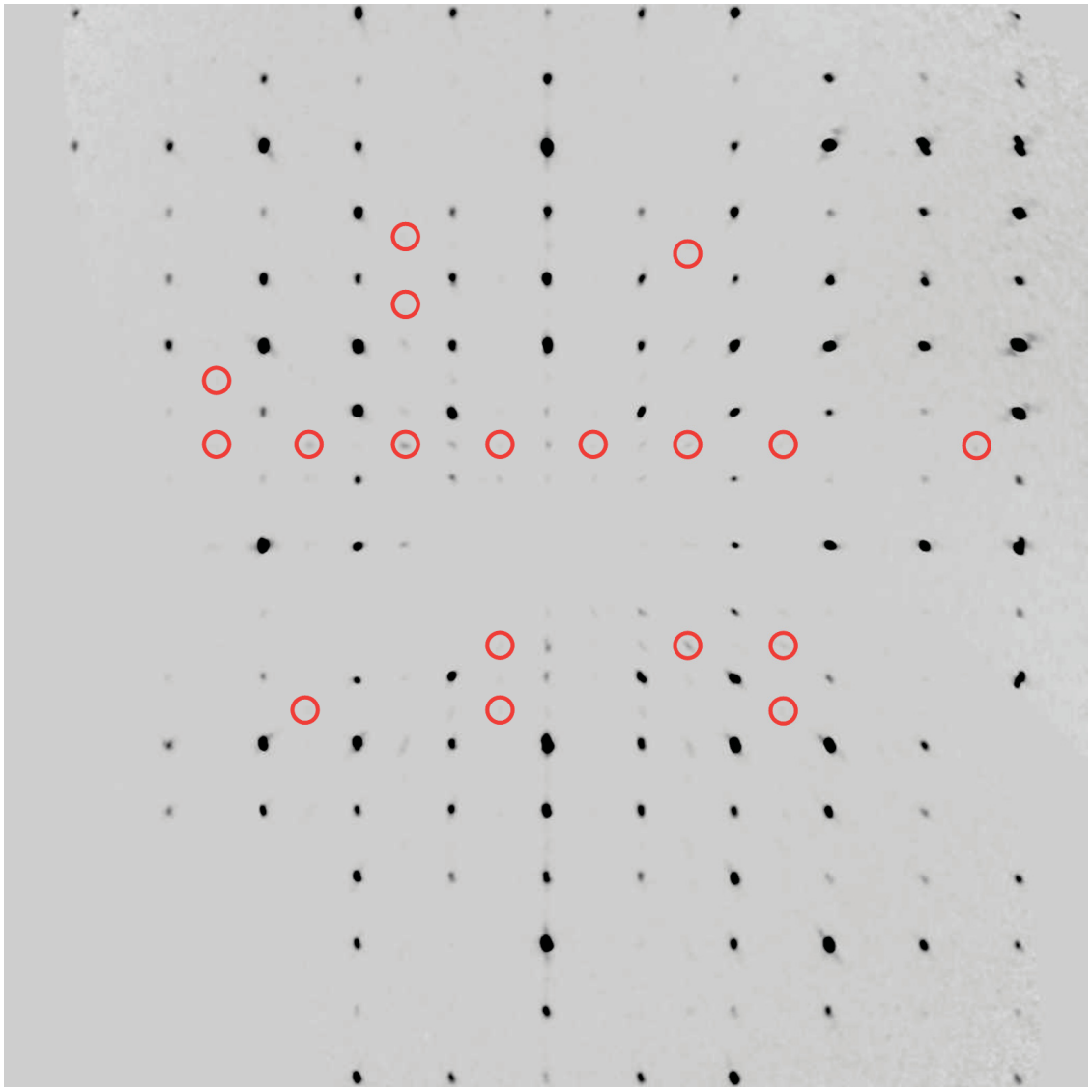

Figure 3.3.2: A $0kl$ precession image taken on Tl_5Te_3 shows faint, possible peaks (circled in red) which, if true peaks intrinsic to the material, violate the systematic absences imposed by the glide plane symmetry element of the *I*4/*mcm* spacegroup

with faint peaks at $0kl : k,l \neq 2n$ locations. If these signals are valid peaks, they could indicate a long-range coherent charge density wave, potentially from charge disproportionation of the Tl ions at the octahedral centers. It is possible, however, that these peaks may be spurious artifacts due to a small second crystal in the beam, or perhaps growth fault in the crystal. An astute reader might observe that the material is nearly pseudocubic: $c = \sqrt{2}a$, meaning the *a*-*b* face diagonal (the [110] direction) is approximately the same length as

the *c* axis, which opens up the possibility of growth faults. Because the intensities of these peaks are low and highly angle-dependent, our in-house powder diffractometer may be insufficient to detect the corresponding peaks in the powder x-ray diffraction pattern. We therefore employed the high resolution and intensity provided by the 11-BM beamline at Argonne National Lab to investigate the presence of these weak reflections as possible evidence for the existence of a charge-ordered state in Tl_5Te_3. Shown in Figure 3.3.3, high-resolution synchrotron data fits well to both *I*4/*mcm* and *I*4/*m* models and does not exhibit peaks at *hkl*'s allowed under the *I*4/*m* but not *I*4/*mcm* (Figure 3.3.3 inset). *I*4/*mcm* is therefore a better description of the structural symmetries of Tl_5Te_3; no periodic modulation of the octahedra is observed.

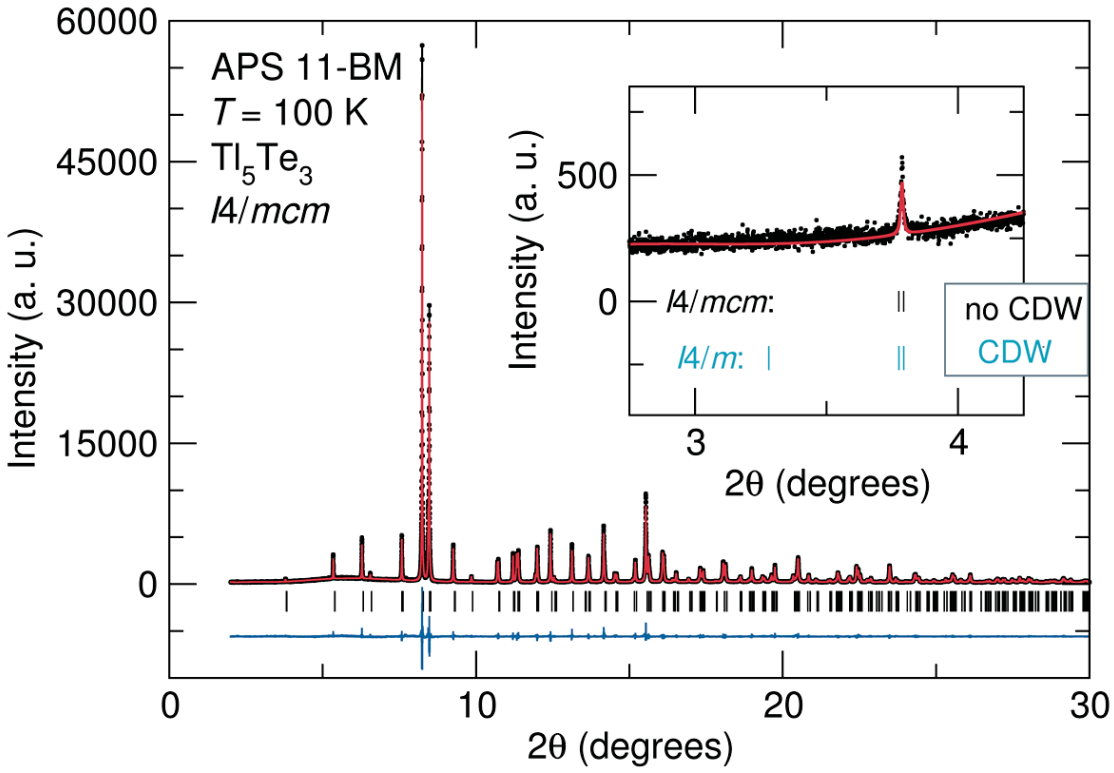

Figure 3.3.3: Reitveld refinement of high-resolution synchrotron XRD data taken at Argonne's 11-BM line on Tl_5Te_3. Data is given in black circles, the modeled fit by a red line, and the difference curve by a displaced blue line. Black and blue tic marks denote the symmetry allowed reflections of fit *I*4/*mcm* and *I*4/*m* spacegroups, respectively. No peaks which violate the *I*4/*mcm* glide plane are observed.

3.4 Pair distribution fuction of Tl_5Te_3

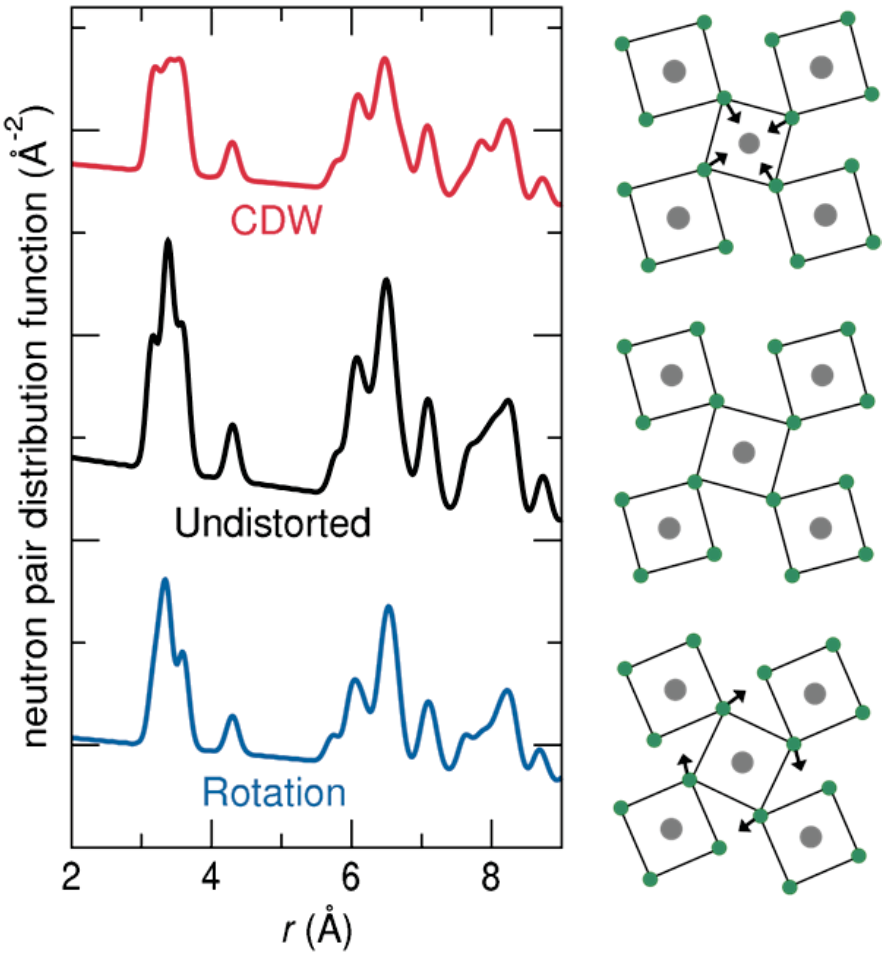

Figure 3.4.1: Simulations of nPDF local structure data are presented. The center black trace is the nPDF simulated for an undistorted *I*4/*mcm* Tl_5Te_3 structure. The red and blue traces simulate the effects of common modes of structural distortion which accommodate charge disproportionation. Right: cartoons of the *a*-*b* plane show exaggerations of the structural distortions in each mode.

In addition to long-range diffraction data, neutron pair distribution functions (nPDF) were measured for Tl_5Te_3. This local-structure data is capable of discerning if Tl^{2+} octahedral centers charge disproportionate in a random or incoherent fashion, which would average out and be undetectable in long-range diffraction methods. In Figure 3.4.1, the nPDFs for undistorted *I*4/*mcm* structure of Tl_5Te_3 is simulated along with two common

charge-disproportionation distortion modes, an octahedral rotation and a change in octahedral size. These distortion modes have a clearly observable effect on the simulated nPDFs.

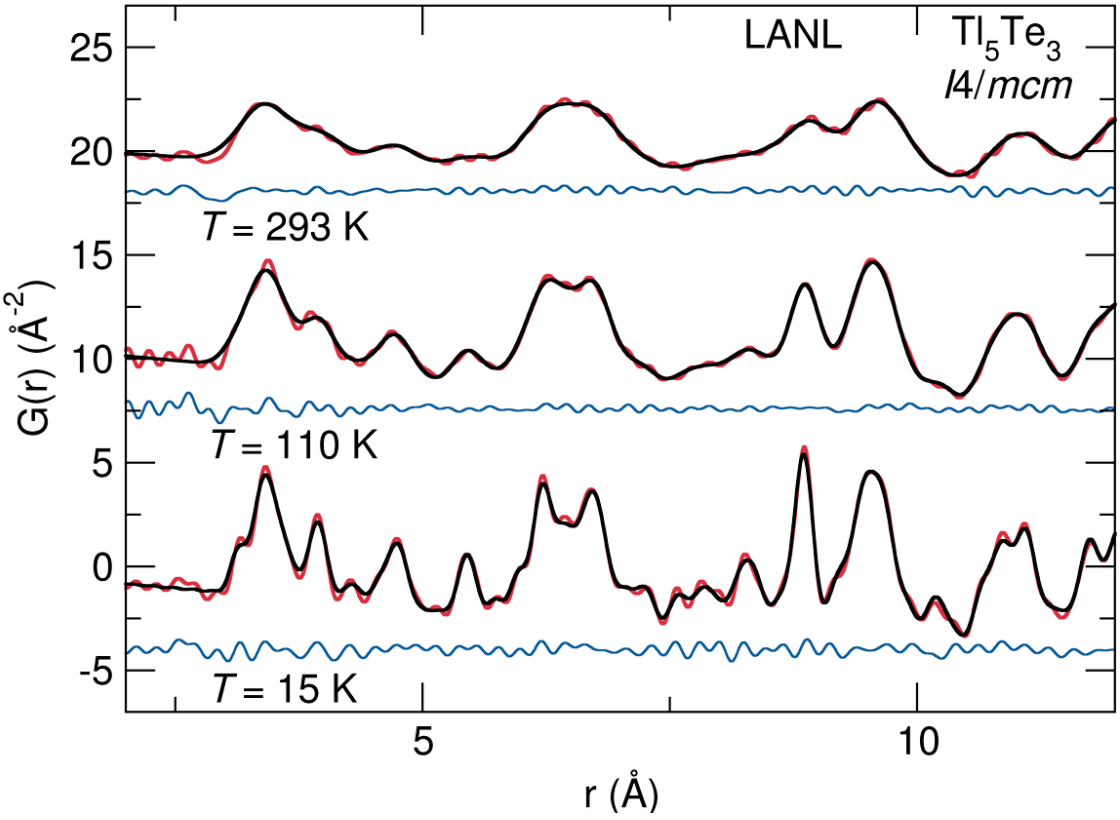

Figure 3.4.2: Local structure data of Tl_5Te_3 taken at Los Alamos National Lab indicate *I*4/*mcm* symmetry. Data taken at lower temperatures offer higher resolution and indicate no structural phase transitions down to $T = 15$ K.

Figure 3.4.2 shows the nPDFs collected on Tl_5Te_3 at three temperatures. The lower temperature data offers higher resolution of each pair distance due to decreased thermal parameters. These data show no evidence of charge disproportionation in the Tl_5Te_3 structure: an *I*4/*mcm* describes the local structure at all temperatures, and no splitting of any pair distances (as might be expected for a distribution of Tl^{1+}–Te and Tl^{3+}–Te bond lengths) is observed.

3.5 Discussion

Analysis of these data sets indicate that, to the best of our current knowledge, both long-range and local structural analysis of Tl_5Te_3 show no sign of a distortion that would accompany Tl^{2+} charge disproportionation. The work present in this chapter begs the question of what makes Tl^{2+} stable in Tl_5Te_3.

A likely reason for the relative stability of Tl^{2+} in Tl_5Te_3 is the nature of thallium-tellurium bonding. Another thallium telluride, TlTe, does not show charge disproportionation: the compound must have a net 2+ charge on the thallium atoms, but all thallium ions in the structure are symmetry-equivalent. In contrast, the thallium selenide compound TlSe has a very different structure type composed of $TlSe_2$ chains and lone Tl atoms in the channels between the chains. This structure allows for charge disproportionation: the bonding Tl atoms in the chains are likely Tl^{3+} due to their short bonds with selenium (Tl-Se = 2.784 Å, compared to a minimum distance of Tl-Se$>$ 2.9 Å in the $Tl_5Te_{3-x}Se_x$ and Tl_5Se_3 compounds discussed in Chapter 7) and the lone, non-interacting Tl atoms in the channels is likely Tl^{1+}. The difference between thallium selenide and thallium telluride may well be a function of bonding character: selenium, having a more dense electron cloud, might bond to thallium more covalently while tellurium atoms, having a larger electron cloud, might bond in a more intermetallic fashion.

Critical to the energetics of charge disproportionation in Tl_5Te_3 is the stability and bonding of Tl^{1+} ([Xe]s^2) and Tl^{3+} ([Xe]s^0) in this structure. The latter ought to pose no problems: highly charged cations bond more easily, and the spherical symmetry of a completely filled shell with no valence electrons imposes no structural/symmetry requirements on bonding. Presumably, the existence of MTl_9Te_6 compounds where M has formal charge 3+ indicates that Tl^{1+} ([Xe]s^2) is capable of occurring stably in the Tl_5Te_3 structure type. The nature and stability of this lone pair is then under question. Literature reports and experimental data adjacent to the research presented in this dissertation indicate that, at least for MTl_9Te_6 compounds, Tl^{1+} has a stereochemically *inert* lone pair in the Tl_5Te_3 structure

type: no structural changes are observed due to a stereochemically active lone pair, which would displace the thallium atom from the center of the octahedra, puckering the bonding in the *a*-*b* plane and reducing the symmetry to a primitive rather than body-centered unit cell (as seen in the structure of $SnTl_4S_3$). As first published by Orgel, a stereochemically active lone pair based in the spherically symmetric *s* orbitals cannot have purely *s* character – in order to displace off center, the state must admix to some extent with *p* orbitals – and Bersuker extended this observation, arguing that the filled anion *p* states admix with the filled cation *s* states of the lone pair [14, 15]. Seshadri has studied further what specifically gives rise to stereochemically *active* lone pairs in some transition metal and heavy *p*-block compounds and stereochemically *inactive*, *inert* lone pairs in others, finding that that empty cation *p* states intermediate the admixing of filled cation *s* states with filled anion *p* states [16–18]. Therefore structures with narrow, well-separated bands due to the cation *s* and *p* states display the inert-pair effect and are not stereochemically active, presumably like Tl^{1+} in MTl_9Te_6. However, in Tl_5Te_3 the Tl *p*, Tl *s*, and Te *p* states are all relatively broad bands near each other based on the DFT-predicted band structure (Figure 6.6.1).

3.6 Phonon modes and implications for the octahedral center

Heat capacity data on Tl_5Te_3, shown in Figure 3.6.1(a), show an Einstein mode. The data is fit to a Debye mode with $\theta_D = 115$ K and 7 oscillators and an Einstein mode with $\theta_E = 34$ K and 1 oscillator. The number of oscillators associated with each mode indicates the number of atoms per formula unit involved in that mode. The Einstein mode's single oscillator is therefore likely the octahedral center, or alternatively the axial tellurium. It is unlikely the two equatorial telluriums or four interstitial thallums separate in vibrational modes but no other observed physical property. Einstein modes are commonly observed in materials near structural instabilities, as well as ferroelectrics which frequently result from cation

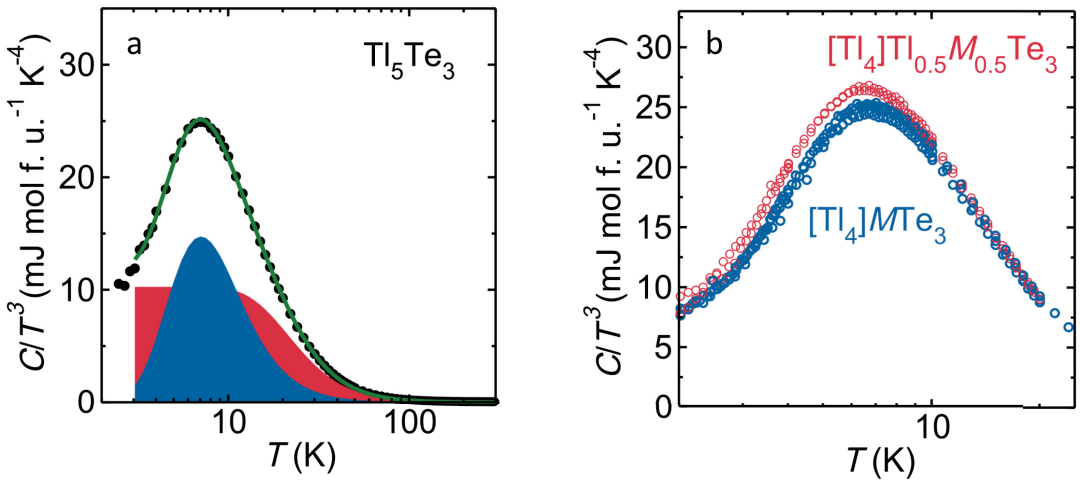

Figure 3.6.1: (a) The heat capacity of Tl_5Te_3 (black circles) is fit (green line) to a Debye mode (contribution shown as red shading) and an Einstein mode (contribution shown as blue shading). (b) The Einstein modes of $[Tl_4]MTe_3$ (blue, M = Sn, Pb, Tl) and $[Tl_4](M_{0.5}Tl_{0.5})Te_3$ (red, M = Bi, Sb) are compared. The choice of axes improves visualization of the two types of modes [19].

displacement from the polyhedral centers due to to stereoactive lone pair [20, 21]. Multiple structural derivatives of this structure can be envisioned: a charge density wave would result from long-range coherent charge disproportionation of Tl^{2+} at the octahedral centers to Tl^{3+} and an inert lone-pair Tl^{1+} ion, or off-centering of a stereochemically active Tl^{1+} lone pair could also result from charge disproportionation of Tl^{2+}. However, the origin of this mode is unclear: Figure 3.6.1(b) shows a similar Einstein modes in heat capacity data of MTl_4Te_3, where M = Sn and Pb, and MTl_9Te_6, where M = Bi and Sb, compounds. (The latter are plotted on a per mole formula $[Tl_4](M_{0.5}Tl_{0.5})Te_3$ unit scale in order to directly compare the datasets.) The ubiquitous presence of an Einstein mode questions whether this mode originates in the octahedral metal centers; rather, it could be due to the interstitial thallium sublattice, the only atoms in the structure whose charge and bonding is independent of the octahedral metals. However, all these substitutional metals are heavy p-block metals also susceptible to lone-pair effects including the inert pair effect, charge disproportionation, and stereochemically active lone pairs; it is possible all are susceptible to similar structural instabilities. While the MTl_9Te_6 data sets appear to overlap with each

other and the $M\mathrm{Tl}_4\mathrm{Te}_3$ data set with each other, the two groups appear to differ slightly from each other. The slight increase in both the height and breadth of the Einstein modes of the $M\mathrm{Tl}_9\mathrm{Te}_6$ data is difficult to fit simultaneously with a single Einstein mode (N.B., more intense Einstein modes are narrower), but can be fit more accurately by two similar Einstein modes with half an oscillator each, which would be the case if both M and Tl were proximal to a structural, charge, or ferroelectric instability.

3.7 Acknowledgments

Kate Page, formerly at Los Alamos National Lab, is thanked for technical assistance and helpful discussions.

Bibliography

[1] P. Böttcher, T. Doert, C. Druska, and S. Bradtmöller, J. Alloys Compd. **246**, 209 (1997).

[2] K. J. Nordell and O. J. Miller, J. Alloys Compd. **241**, 51 (1996).

[3] I. Schewe, P. Böttcher, and H. G. v. Schnering, Z. Kristallogr. **188**, 287 (1989).

[4] G. Celik and S. Cabuk, Central European Journal of Physics, **11**(3), 387 (2013).

[5] K. Momma and F. Izumi, J. Appl. Cryst. **44**, 1272 (2011).

[6] Y. V. Voroshilov, M. I. Gurzan, Z. Z. Kish, and L. V. Lada, Neorganicheskie Materialy **24**, 1479 (1988).

[7] G. Thornton and A. J. Jacobsen, Acta Cryst. B **34**, 351 (1978).

[8] A. M. Glazer, Acta Cryst. B **28**, 3384 (1972).

[9] L. I. Man, Kristallografia, **16**(1), 122 (1971).

[10] A. Abba Toure, G. Kra, R. Eholie, J. Olivier-Fourcade, and J.-C. Jumas. J. Sol. State Chem. **87**, 229 (1990).

[11] J.-M. Joubert and Y. Feutelais, Calphad **26**(3), 427 (2002).

[12] R. E. Marsh, J. Sol. State Chem. **92**, 594 (1991).

[13] E. Cruceanu and S. Sladaru, J. Mater. Sci. **4**, 410 (1969).

[14] L. E. Orgel, J. Chem. Soc. **4**, 3815 (1959).

[15] I. B. Bersuker, *The Jahn-Teller Effect and Vibronic Interactions in Modern Chemistry* (Plenum, New York, 1984).

[16] U. V. Waghmare, N. A. Spaldin, H. C. Kandpal and R. Seshardri, Phys. Rev. B **67**, 125111 (2003).

[17] M. W. Stoltzfus, P. M. Woodward, R. Seshardri, J.-H. Klepeis, and B. Bursten, Inorg. Chem. **46**, 3839 (2007).

[18] R. Seshardri, in *ICMS-ICMR Winder School on Chemistry and Physics of Materials, 2007*.

[19] A. P. Ramirez and G. R. Kowach, Phys. Rev. Lett. **80**, 4903 (1988).

[20] P. W. Anderson, in *Proceedings of the All-Union Conference on the 'Physics of Dielectrics', Academy of Science, USSR, Moscow, 1958* p. 290.

[21] W. Cochran, Adv. in Phys. **9**, 387 (1960).

4 Superconducting properties of Tl_5Te_3

Portions of the following chapter are based on the article "Evidence for Topologically Protected Surface States and a Superconducting Phase in $[Tl_4]Tl_{1-x}Sn_xTe_3$ Using Photoemission, Specific Heat, and Magnetization Measurements, and Density Functional Theory" by K. E. Arpino, D. C. Wallace, Y. F. Nie, T. Birol, P. D. C. King, S. Chatterjee, M. Uchida, S. M. Koohpayeh, J.-J. Wen, C. J. Fennie, K. M. Shen, and T. M. McQueen published in Physical Review Letters 112, 017002 (2014). [1]

As introduced in Section 1.4, Tl_5Te_3 is a bulk superconductor [2, 3]. This chapter details our characterization of the superconducting properties of Tl_5Te_3, including adherence to BCS theory and a strong anisotropy of the lower critical field that is not well described by Ginzburg-Landau theory. A full characterization of the parent compound's superconductivity lays the framework for additional research into superconducting domes in multiple isovalant doping series and the coexistence of superconductivity with topological surface states.

4.1 Methods

Polycrystalline Tl_5Te_3 samples were prepared in the manner described in Section 3.1. For anisotropic measurments, single crystals were prepared using a modified Bridgman method

described in Section 2.1 in an optical floating-zone furnace (Crystal Systems Inc.) using 2.5% excess Te as a flux. The use of a Te flux was necessitated by the phasewidth of the Tl_5Te_3 compound discussed in Section 3.2. Crystals grown without a flux tended to be Tl-rich, presumably due to the loss of Te due to some vaporization (commonly found in beads on the side of the tube) and/or possible TlTe side product. In contrast, crystals grown using a Te flux were found by laboratory XRD to be precisely stoichiometric. The precise stoichiometry is relevant to this chapter as we find T_c is optimized for the stoichiometric compound and decreased or quenched entirely in Tl-rich samples (see data in Section 4.2)

Physical property measurements down to $T = 1.8$ K were performed on a Quantum Design, Inc. Physical Property Measurement System using the heat capacity and ACMS options. Low-temperature heat capacity data from T = 0.15 K to 4 K were collected with the aid of a dilution refrigerator.

4.2 Magnetic susceptibility of Tl_5Te_3

Figure 4.2.1 shows the magnetic response of Tl_5Te_3 powder samples under a small, constant, applied magnetic field. At temperatures below $T_c = 2.4$ K, the stoichiometric Tl_5Te_3 exhibits a magnetic response that opposes the applied field; this is a diagnostic characteristic of superconductors as described in Sections 1.3.1 and 2.3.1. The strength of the response $4\pi\chi_{\mathrm{cgs}} = \chi_{\mathrm{SI}} \approx 1$ indicates bulk superconductivity: the magnetization of the material (generated in response to the applied field) is roughly equal to the magnetic field strength of the applied field. Here the zero-field cooled stoichiometric sample appears to have a magnetization response which exceeds the applied field ($4\pi\chi_{\mathrm{cgs}} = \chi_{\mathrm{SI}} \approx 1.25 > 1$). Such a response is physically unlikely, instead it is more probable that there may have been a remnant field on the order of a few Oe, resulting in an error of up to 30% when an H = 10 Oe field is applied. The field-cooled curve of the stochiometric sample indicates a markedly lower superconducting fraction. This could indicate a large amount of defects

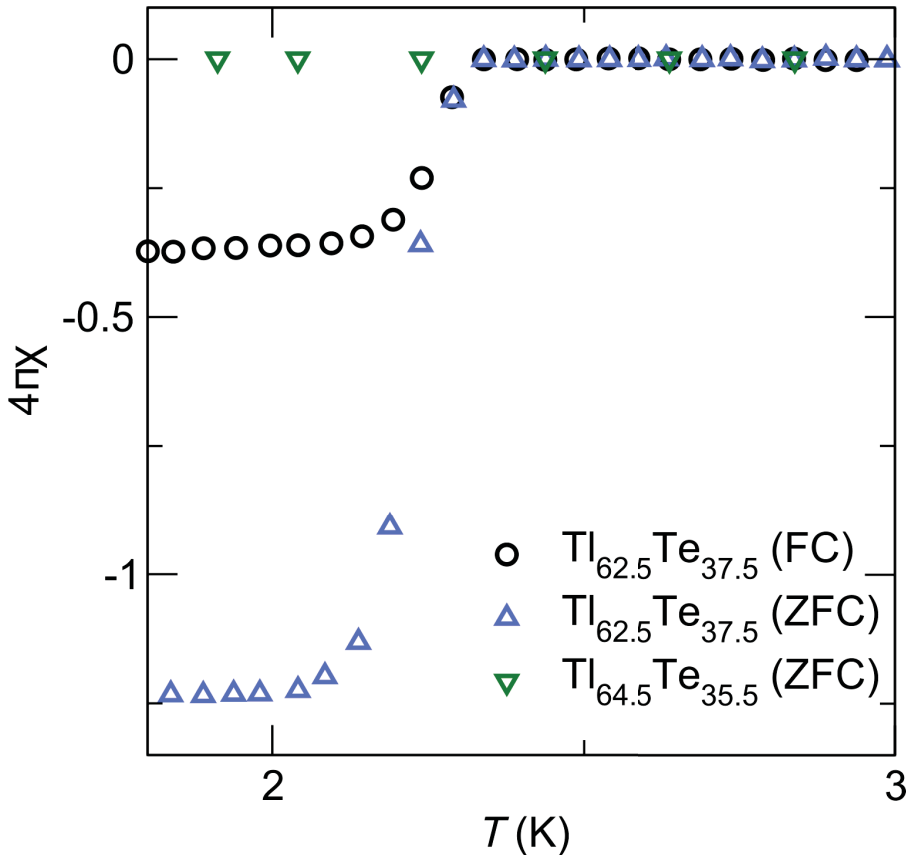

Figure 4.2.1: The magnetic susceptibility χ (in Gaussian-cgs units) of stochiometric Tl_5Te_3 ($Tl_{62.5}Te_{37.5}$, black circles and purple triangles) and a Tl-rich sample ($Tl_{64.5}Te_{35.5}$, green triangles) are shown at low temperatures. The data on the stoichiometric compound indicates bulk superconductivity below $T_c = 2.4$ K. Data is shown for both field-cooled ("FC," black circles) and zero field field cooled ("ZFC," purple triangles) measurements. The Tl-rich sample does not display superconductivity in the measured temperature range.

and/or impurities, though the heat capacity data (Section 4.3) will argue against impurities. It is also possible that the applied field $H = 10$ Oe exceeds the lower critical field H_{c1} for a portion of this sample (will be shown in Section 4.4), reducing the superconducting fraction measured under fields.

In contrast to the bulk or at least largely superconducting stoichiometric sample, a Tl-rich sample (shown as green triangles in Figure 4.2.1) does not exhibit any superconducting response in the range of temperatures measured. The phasewidth of Tl_5Te_3 has previously been noted and studied [4–6], though its impact on the compound's physical properties has

not been appreciated. These findings indicate the importance of sample quality and stoichiometry as a major consideration when studying physical properties in this compound.

4.3 Heat capacity of Tl_5Te_3

Low-temperature specific heat data collected on a polycrystalline Tl_5Te_3 flake under zero magnetic field reveal a clear λ-anomaly, shown in Figure 4.3.1. An applied field of $H = 5,000$ Oe is sufficient to quench superconductivity entirely; below $T = 1.5$ K, temperatures at which any complex phonon structure should be negligible, these field-applied data were fit to the low-temperature approximation of heat capacity $C \approx \gamma T + \beta_3 T^3$ (Equation 2.6, Section 2.3.2), where γT is the electronic contribution and $\beta_3 T^3$ is the lattice phonons heat capacity [**?**]. This fit returns $\gamma = 9.34(4)$ mJ mol f.u.$^{-1}$ K^{-2} and $\beta_3 = 6.82(5)$ mJ mol f.u.$^{-1}$ K^{-4}, which corresponds to a Debye temperature of $\theta_D = 132(1)$ K [7].

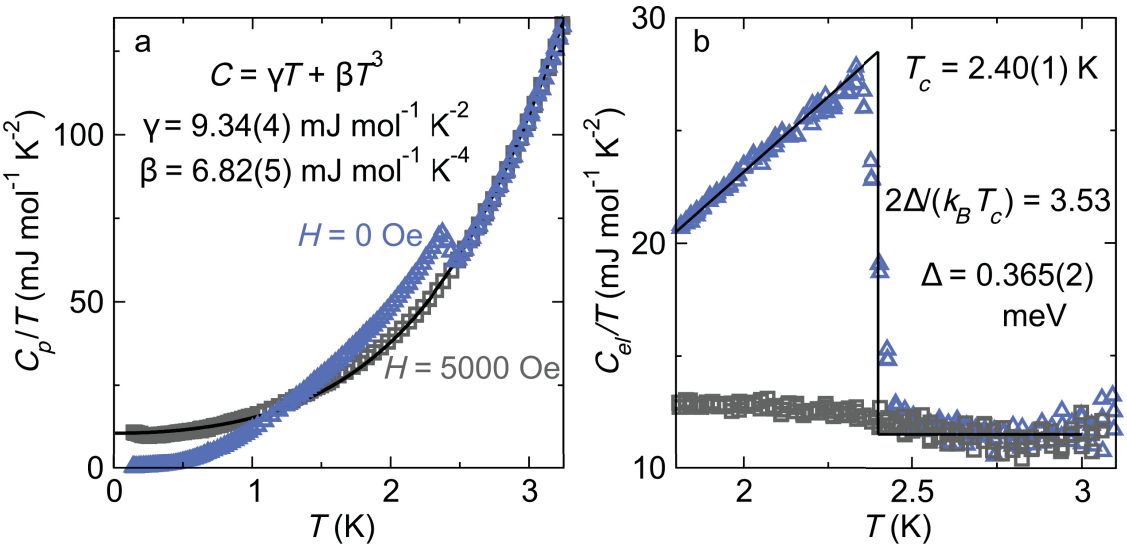

Figure 4.3.1: Heat capacity data of Tl_5Te_3 display a lambda anomaly indicating a superconducting transition. (a) Low-temperature heat capacity data taken on a polycrystalline flake under $H = 0$ Oe (purple triangles) and 5,000 Oe (gray circles) is shown. The zero-field data show a lambda anomaly corresponding with the superconducting transition. Data taken under a field did not exhibit superconducting behavior and were fit (black line) to an approximate model of low-temperature electronic and phononic heat capacity. (b) An equal-entropy construction (black lines) determines T_c precisely.

Subtracting the low-temperature lattice specific heat fit from the zero-field data gives the electronic specific heat, plotted in Figure 4.3.1(b). The black lines show an equal-entropy construction (Section 2.3.2) which indicates bulk superconductivity with $T_c = 2.40(1)$ K. This value of T_c predicts a superconducting energy gap of $\Delta = 0.365(2)$ meV using the BCS relation $\frac{2\Delta}{k_B T_c} = 3.53$ (Equation 1.2, Section 1.3.1) [8, 9]. Additionally using γ from the low-temperature fit and estimating ΔC_{el} from the equal-entropy construction, we calculate the ratio $\Delta C_{el}/(\gamma T_c)$ = 1.63, which is close to the weak coupling Bardeen-Cooper-Schrieffer (BCS) value of 1.43. [8, 9] The gradual softening of the lambda-anomaly peak with small fields (not shown) confirm type II superconductivity.

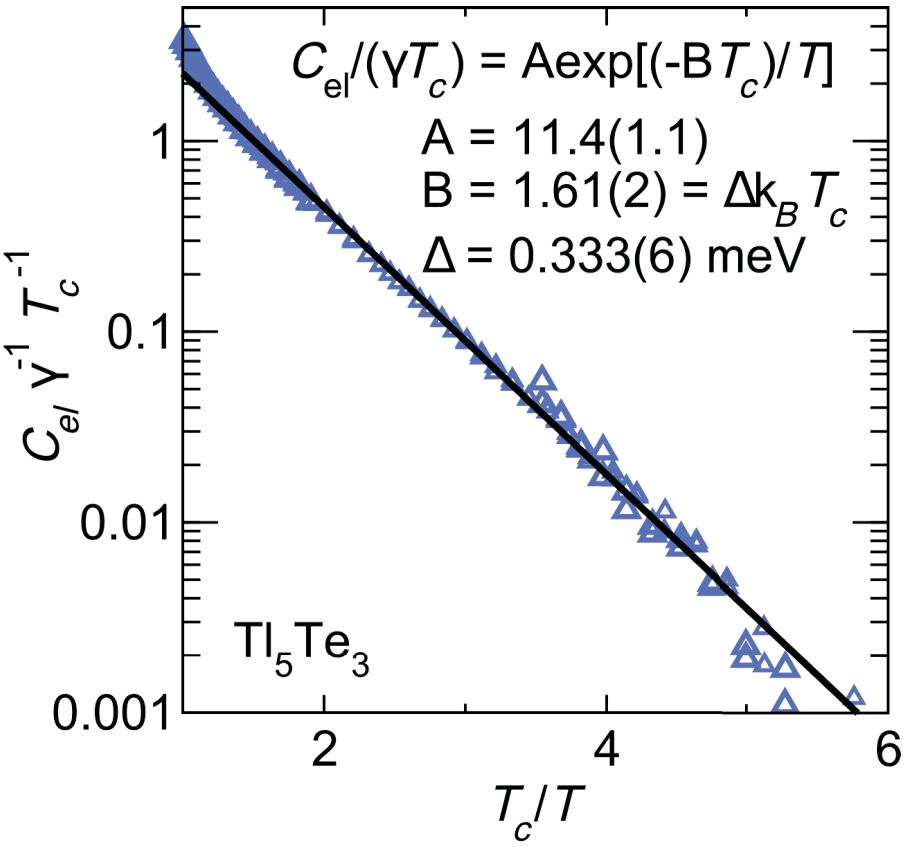

Figure 4.3.2: The electronic specific heat of polycrystalline Tl_5Te_3 (purple triangles) fits the BCS relationship (black line) for a single-gap *s*-wave superconductor.

Previously, it was suggested that two-gap superconductivity might explain some discrepancies observed in the bulk superconductivity of Tl_5Te_3 [3]. To investigate whether

Tl_5Te_3 can be well described by the BCS model of a single-gap *s*-wave superconductor, the electronic specific heat was fit to the single-gap equation [7, 8]:

$$\frac{C_{el}}{\gamma T_c} = Ae^{-B/T} \tag{4.1}$$

with $A = 11.4(1.1)$ and $B = 1.61(2)$, which holds for $T_c/T \gtrsim 2$ (Figure. 4.3.2). Note that a superconductor with multiple gaps would have an $Ae^{-B/T}$ term for each gap on the righthand side of the equation. A value of $B = \Delta k_B T_c = 1.61(2)$ predicts a superconducting gap of Δ = 0.333(6) meV [7, 8]. This value, based on the electronic specific heat data, agrees with the superconducting gap of $\Delta = 0.365(2)$ meV predicted above using the critical temperature. The agreement of these values indicate a robust analysis under BCS theory. In conjuction with the ratio $\Delta C_{el}/(\gamma T_c)$ = 1.63 determined above, we conclude that the specific heat of Tl_5Te_3 agrees with the BCS theory of single-gap *s*-wave behavior. We note that being a fully gapped bulk superconductor is a prerequisite for a candidate topological superconductor [10].

4.4 Anisotropic measurements of Tl_5Te_3

Isothermal dc magnetization measurements taken at $T = 1.8$ K on powder Tl_5Te_3 and on a single crystal with the field oriented parallel to the [110] and [100] crystal directions are shown in Figure 4.4.1. The direction-dependent measurements were taken on an approximately cubic oriented single crystal (Figure 4.4.1 image inset). Demagnetization factors of $N = 1/3$ were applied to the single crystal data to account for the shape of the oriented single crystal (see Subsection 2.3.1) [9], but were not applied to the powder sample as it is presumably compose of a set of crystallites of random size and orientation relative to the applied field. Fitting $\chi = \lim_{dH\to 0} dM/dH$ for either directional measurement, shown as a dashed line in the graphical inset of Figure 4.4.1, results in values of χ which correspond to bulk (<95%) superconductivity (i.e., $4\pi\chi_{\text{cgs}} > 0.95$ approaches unity). The value of χ

for the data taken on the powder sample is not shown, as the data curves gently for fields up to H_{c1} and the value of χ therefore varies from ∼50-70% based on the range used to estimate the limit. However, it is clear that the value of χ is less for the powder data than it is for the oriented crystal (∼60% superconducting for the powder data vs. $> 95\%$ for superconducting for the single crystal). It is highly unlikely that this could be a result of sample quality: the powder sample is a piece of the crystal which had been broken off and ground up, and laboratory XRD data indicate the powder sample is of high quality. It is instead more likely that the behavior of the powder data is a result of the anisotropy of Tl_5Te_3's superconducting behavior.

4.4.1 Anisotropic Ginzburg-Landau analysis

The graphical inset of Figure 4.4.1 shows a sizeable anisotropy of H_{c1}: data taken with the field applied parallel to the c axis (the [001] crystal direction) have a lower critical field H_{c1} below $H = 10$ Oe, while those data taken with the field applied perpendicular to the c axis in the [110] crystal direction have a higher lower critical field, $H_{c1} \approx 25$. This anisotropy may explain the reduced χ of the powder data. Powder should, in the absence of preferred direction, be randomly oriented, which would correspond to about half as much field being applied along the c-axis as applied is perpendicularly to it. In other words, one should observe about 2/3 "perpendicular to c-axis" behavior (higher H_{c1}) and 1/3 "parallel to c-axis" (lower H_{c1}) behavior in the powder data, which would result in roughly 67% superconducting fraction at fields above $H_{c1,[001]}$ and below $H_{c1,[110]}$.

While the directional lower critical fields differ by a factor of greater than three, the upper critical fields appear to be the same within error (Figure 4.4.1). This discrepancy is not due to a demagnetization effect – it cannot be resolved by using any combination of physical ($0 \leq N \leq 1$) demagnetization factors on the two orientations. This difference in anisotropy between upper and lower critical fields can be evaluated with the anisotropic equations of Ginzburg-Landau theory [9]. Generally speaking, a direction which has a

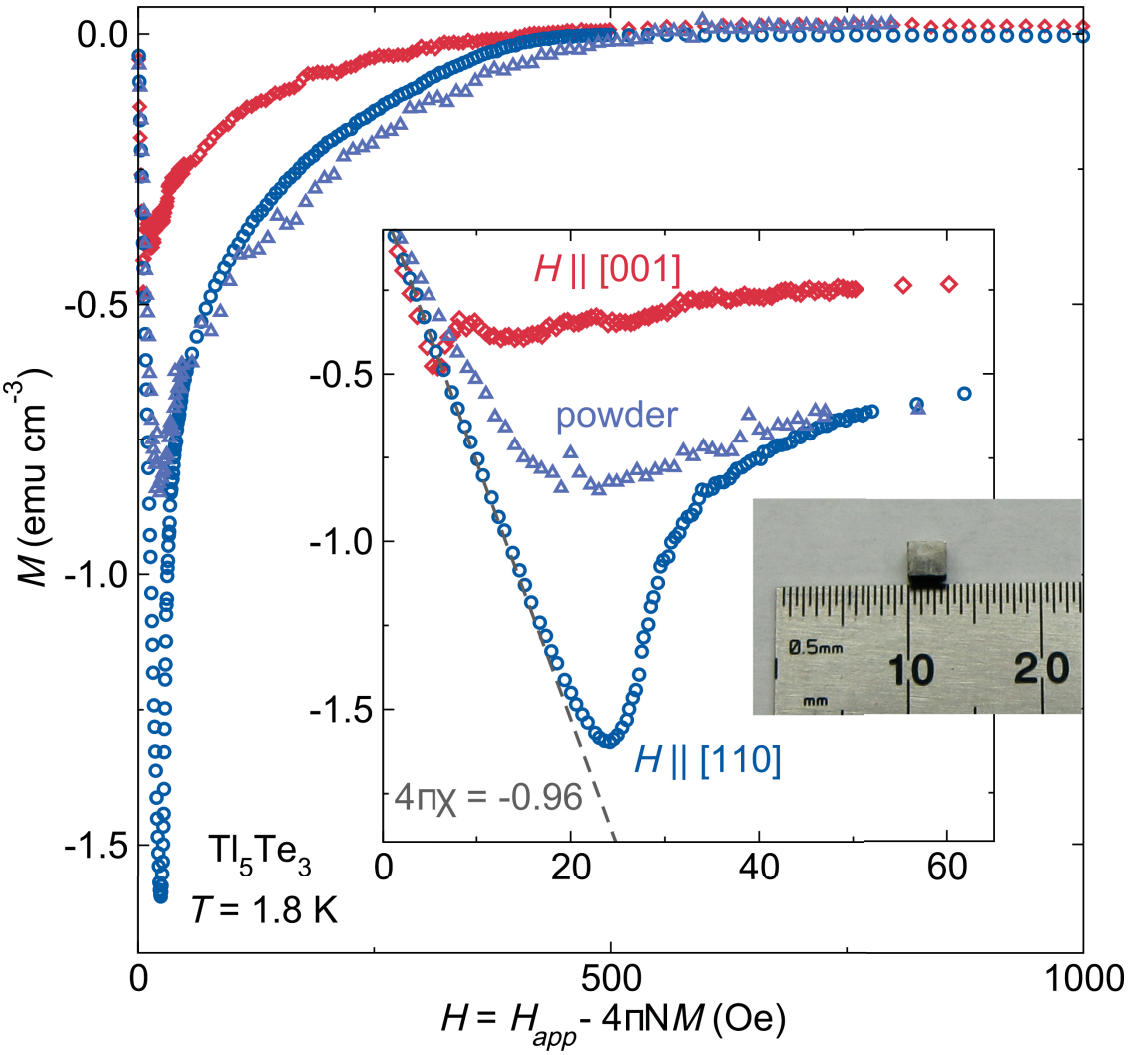

Figure 4.4.1: Isothermal magnetization data collected on an oriented single crystal at T = 1.8 K with the field applied parallel to the [001] direction (red diamonds) and [110] direction (blue circles) are plotted with powder data (purple triangles). A demagnetization factor of N = 1/3 has been applied to the single crystal data to account for the approximately cubic shape of the 100 mg single crystal sample (image inset). A zoomed view of the magnetic response at low fields (graph inset) illustrates the anistropy of H_{c1} and the bulk nature of the superconducting response (χ shown a gray dashed lines).

lower lower critical field $H_{c1,i}$ has a higher upper critical field $H_{c2,i}$ in order to satisfy the uniform bulk thermodynamic critical field $H_{c_{\mathrm{Th}}}$. This can be seen in the relationship:

$$\frac{H_{c1,i} \cdot H_{c2,i}}{ln\kappa_i} = {H_{c_{\mathrm{Th}}}}^2. \tag{4.2}$$

Because $H_{c_{\mathrm{Th}}}$ is a thermodynamic quantity independent of direction, Ginzburg-Landau theory therefore requires that

$$\frac{H_{c1,[110]} \cdot H_{c2,[110]}}{ln\kappa_{[110]}} = {H_{c_{\mathrm{Th}}}}^2 = \frac{H_{c1,[001]} \cdot H_{c2,[1001]}}{ln\kappa_{[001]}}. \tag{4.3}$$

Because $H_{c2,[110]} \approx H_{c2,[001]}$, Equation 4.3 becomes

$$\frac{H_{c1,[110]}}{H_{c1,[001]}} = \frac{ln\kappa_{[110]}}{ln\kappa_{[001]}}. \tag{4.4}$$

Given that $H_{c1,[110]}$ is approximately three times $H_{c1,[001]}$, Equation 4.4 simplifies to $\kappa_{[110]} = (\kappa_{[001]})^3$. Ginzburg-Landau theory additionally requires that

$$H_{c2,i} = \sqrt{2}k_i H_{c_{\mathrm{Th}}}, \tag{4.5}$$

which implies that $\kappa_{[110]} \approx \kappa_{[001]}$ because $H_{c2,[110]} \approx H_{c2,[001]}$. Thus Equations 4.3 and 4.3 can only be simultaneously satisfied by $\kappa_{[110]}, \kappa_{[001]} \approx 1$. These values agree with those calculated by ratio of upper to lower criticial fields:

$$\frac{H_{c2,i}}{H_{c1,i}} = \frac{\kappa_i^2}{ln\kappa_i} \tag{4.6}$$

which yields $\kappa_{[110]} = 1.09$ and $\kappa_{[001]} = 1.02$. These values of $\kappa > 1\sqrt{2}$ support type II superconductivity. We note the analytical equations of Ginzburg-Landau theory deviate at values of κ near 1 (due to $ln1 = 0$).

The apparent oscillations at $H_{c1} < H$ in the data set taken with H applied along the c axis exceed the experimental error, occur repeatedly, and are unexplained.

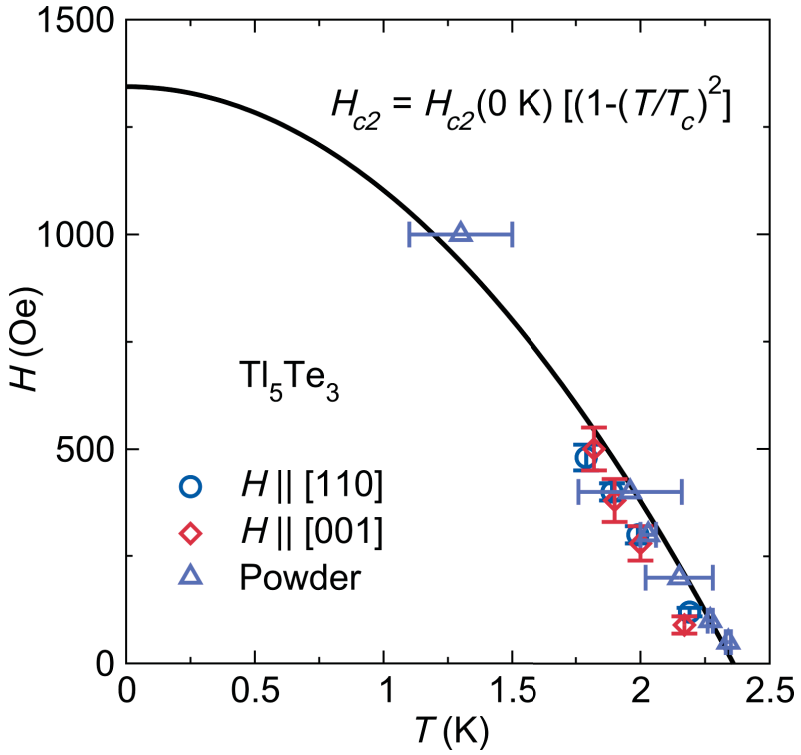

Figure 4.5.1: The field-temperature superconducting phase diagram of Tl_5Te_3 shows H_{c2} as determined by specific heat (purple triangles) and orientation-dependent isothermal DC magnetization (blue circles and red diamonds), along with a two-fluid model fit (black line) to the data.

4.5 Superconducting phase diagram of Tl_5Te_3

The superconducting phase diagram of Tl_5Te_3 is shown in Figure 4.5.1. The directional and powder data, gathered from isothermal magnetization measurements and heat capacity, appear to agree. The conglomerated values of H_{c2} are fit to a BCS two-fluid model:

$$H_c = H_{c,0\,\mathrm{K}} \cdot \left[1 - \left(\frac{T}{T_c}\right)^2\right] \tag{4.7}$$

No deviation from the BCS model is observed. This chapter therefore shows the superconducting properties of Tl_5Te_3 follow BCS theory for a single-gap superconductor with a strong anisotropy of the lower critical field.

Bibliography

[1] K. E. Arpino, D. C. Wallace, Y. F. Nie, T. Birol, P. D. C. King, S. Chatterjee, M. Uchida, S. M. Koohpayeh, J.-J. Wen, C. J. Fennie, K. M. Shen, and T. M. McQueen, Phys. Rev. Lett. **112**, 017002 (2014).

[2] A. Juodakis and C. R. Kannewurf, J. Appl. Phys. **39**, 3003 (1968).

[3] W. H. Haemmerle, W. A. Reed, A. Juodakis, and C. R. Kannewurf, J. Appl. Phys. **44**, 1356 (1973).

[4] E. Cruceanu and S. Sladaru, J. Mater. Sci. **4**, 410 (1969).

[5] I. Schewe, P. Böttcher, and H. G. v. Schnering, Z. Kristallogr. **188**, 287 (1989).

[6] J.-M. Joubert and Y. Feutelais, Calphad **26**(3), 427 2002.

[7] A. Tari, *The Specific Heat of Matter at Low Temperatures* (Imperial College Press, London, 2003).

[8] J. C. Bardeen, L. N. Cooper, and J. R. Schrieffer, Phys. Rev. **108**, 1175 (1957).

[9] C. P. Poole, H. A. Farach, and R. J. Creswick, *Superconductivitiy* (Academic Press, San Diego, 1995).

[10] J. D. Sau, R. M. Lutchyn, S. Tewari, and S. Das Sarma, Phys. Rev. B **82**, 094522 (2010).

5 Prediction and Discovery of Topological Properties in the $[Tl_4]MTe_3$ family

The following chapter is based on the article "Evidence for Topologically Protected Surface States and a Superconducting Phase in $[Tl_4]Tl_{1-x}Sn_xTe_3$ Using Photoemission, Specific Heat, and Magnetization Measurements, and Density Functional Theory by K. E. Arpino, D. C. Wallace, Y. F. Nie, T. Birol, P. D. C. King, S. Chatterjee, M. Uchida, S. M. Koohpayeh, J.-J. Wen, C. J. Fennie, K. M. Shen, and T. M. McQueen published in Physical Review Letters 112, 017002 (2014). [**?**]

In this chapter, we report the discovery of Dirac-like surface states in the perovskite superconductor Tl_5Te_3 as observed by angle-resolved photoemission spectroscopy (ARPES). Density functional theory (DFT) predicts these surface states to be $\mathbb{Z}_2$ topologically protected due to a spin-orbit-driven band parity inversion at the Z time reversal invariant momentum (TRIM) point of the first Brillouin zone. This discovery is groundbreaking as it is possibly the first known material in which intrinsic bulk superconductivity and $\mathbb{Z}_2$ topological surface states exist. Moreover, ARPES measurements reveal Dirac-like surface states in the non-superconducting tin-doped derivative $Sn_xTl_{1-x}Tl_4Te_3$. DFT predicts fully doped $SnTl_4Te_3$ to be $\mathbb{Z}_2$ topologically trivial, which suggests the possibility of a chemical doping-mediated topological phase transition in the $Sn_xTl_{1-x}Tl_4Te_3$ series.

5.1 Prediction of topological character of $[Tl_4]TlTe_3$

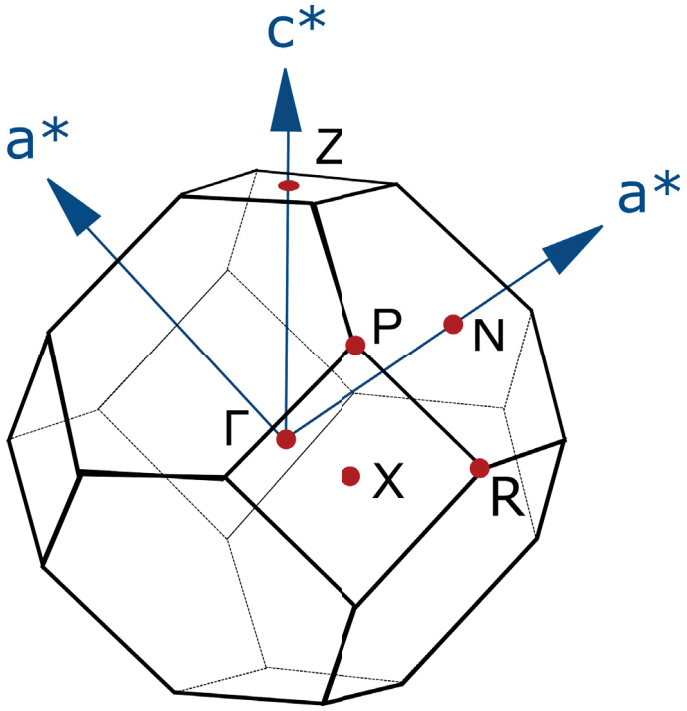

Figure 5.1.1: The Brillouin zone of a body-centered tetragonal unit cell with the lattice parameters of Tl_5Te_3 is shown. Only one of each special momentum point is shown.

The pervoskite-like $[Tl_4]MTe_3$ compounds have a tetragonal symmetry; specifically, parent structure $[Tl_4]TlTe_3$ is body-centered tetragonal with spacegroup $I4/mcm$. There are several ways in which the symmetry of $[Tl_4]MTe_3$ can produce topologically protected surface states. First, the mirror planes which protect surface states in rock salt topological crystalline insulators such as SnTe are also present in the basic perovskite structure of this family; the appropriate band inversions at points protected by mirror symmetry similarly may yield a topological crystalline insulator state in body-centered tetragonal symmetry. Second, strong $\mathbb{Z}_2$ topologically protected surface states result from an odd number of band parity inversions [2]. The body-centered tetragonal crystal class of the $[Tl_4]MTe_3$ structure has four sets of time-reversal invariant points: one Γ, four N, two X, and one Z, shown in Figure 5.1.1. A single inversion of bands of opposite parity at either the Γ or

Z point, but not both, would therefore produce strong $\mathbb{Z}_2$ topologically protected surface states. It is a reasonable to assume that spin-orbit coupling would cause any such band inversion based on the heavy elements that comprise $[Tl_4]TlTe_3$, and also based on the cause of band-inversion in known topological matters. Calculation of the band structure with and without accounting for spin-orbit coupling will predict whether spin-orbit coupling does indeed cause an odd number of band-parity inversions in $[Tl_4]MTe_3$.

To investigate these possibilities, first principles (DFT) calculations were performed with full-potential linear augmented wave formalism as implemented in WIEN2k [3]. Exchange-correlation energies are calculated with Perdew-Burke-Erzenhof (PBE) functionals [4]. An $8\times8\times8$ unshifted k-point grid is used in the Brillouin zone of the primitive body-centered tetragonal cell. Results reported were double-checked by repeating calculations in Projector Augmented Wave (PAW) formalism, as implemented in VASP, and no disagreements were found [5]. The $I4/mcm$ cell used for the calculations was determined by Rietveld refinements of neutron powder diffraction data collected on Tl_5Te_3 at $T = 295$ K, 100 K, and 15 K on the nPDF instrument at the Los Alamos Neutron Science Center shown in Chapter 3. These data are consistent with the structural data obtained from synchrotron x-ray diffraction at higher temperatures, also shown in Chapter 3.

Band structures resulting from first principles (DFT) calculations on Tl_5Te_3 with and without spin-orbit coupling are shown in Figure 5.1.2. Spin-orbit coupling induces a single band inversion between valence and conduction band states at the Z point approximately 0.5 eV above the calculated Fermi level, highlighted in Figure 5.1.2(c). This inversion is between opposite-parity states, the conduction band involving states from the interstitial thalliums and the valence band involving mainly states from axial Te atoms and the Tl ions at the octahedral centers. The orbital contribution to the valence bands is shown in Figure 5.1.3; the shading of these lines indicate the extent of each orbital contribution. These results indicate a $\mathbb{Z}_2$ non-trivial topology. To confirm the non-trivial bulk band topology, we have calculated the $\mathbb{Z}_2$ invariant (Subsection 1.3.2, Equation 1.5) to be -1 by taking the

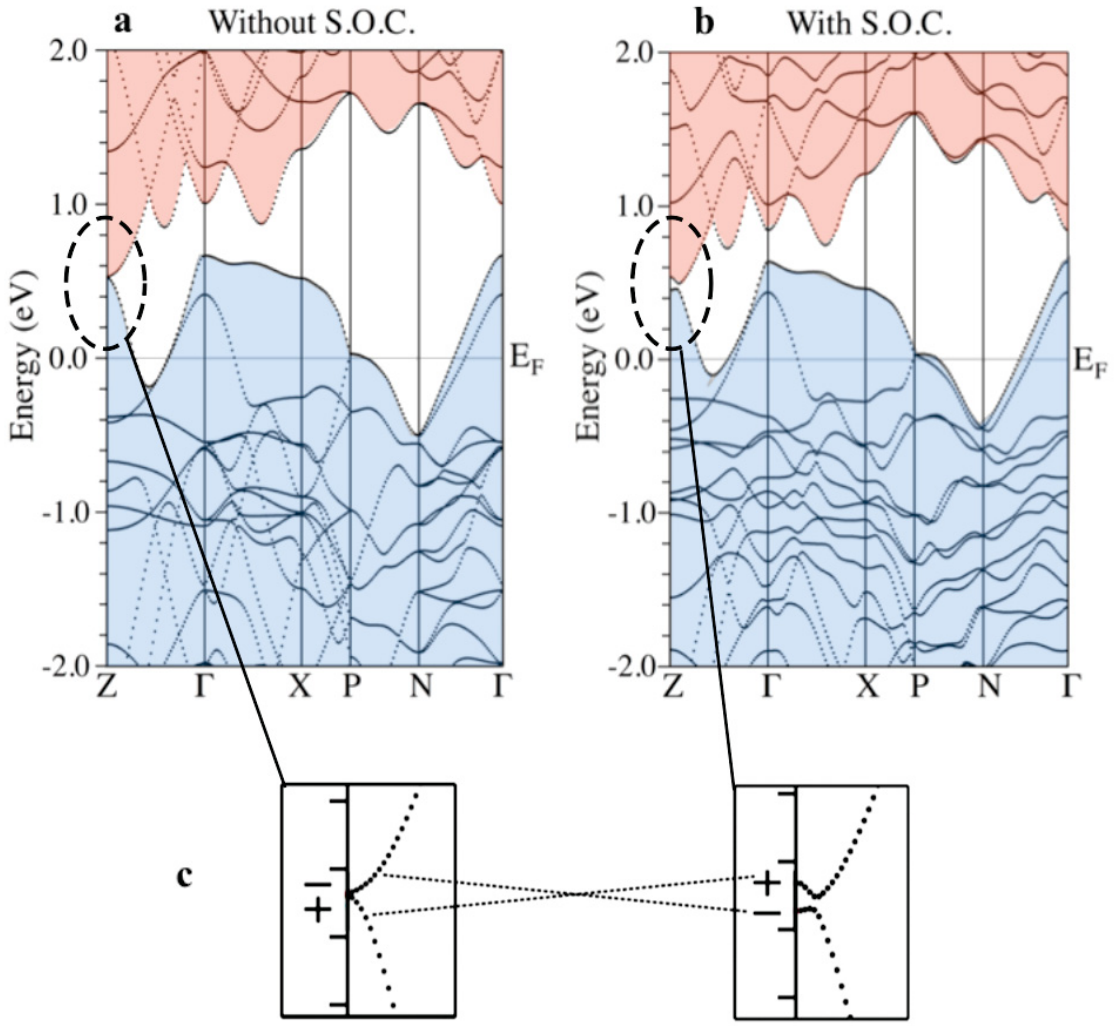

Figure 5.1.2: The band structure ofTl_5Te_3, calculated from first principles DFT both without (a) and with (b) spin-orbit interactions. Shading denotes bands arising from valence (blue) and conduction (pale red) band states. The spin-orbit interaction produces a single band parity inversion approximately 0.5 eV above the E_F at the Z point, shown close-up in (c). Band parities are indicated by + and - signs.

product of the parity of all the bands at the Γ and Z points that connect to the occupied valence bands, including two bands above the Fermi level at the Γ point. Therefore, DFT predicts Tl_5Te_3 to have surface states protected by a non-trivial $\mathbb{Z}_2$ topology.

Note this band structure has two features which prevent Tl_5Te_3 from being a candidate "topological insulator." First, the E_F is clearly below the top of the valence band, indicating Tl_5Te_3 is a metal (this is empirically confirmed by the material's silvery luster and color).

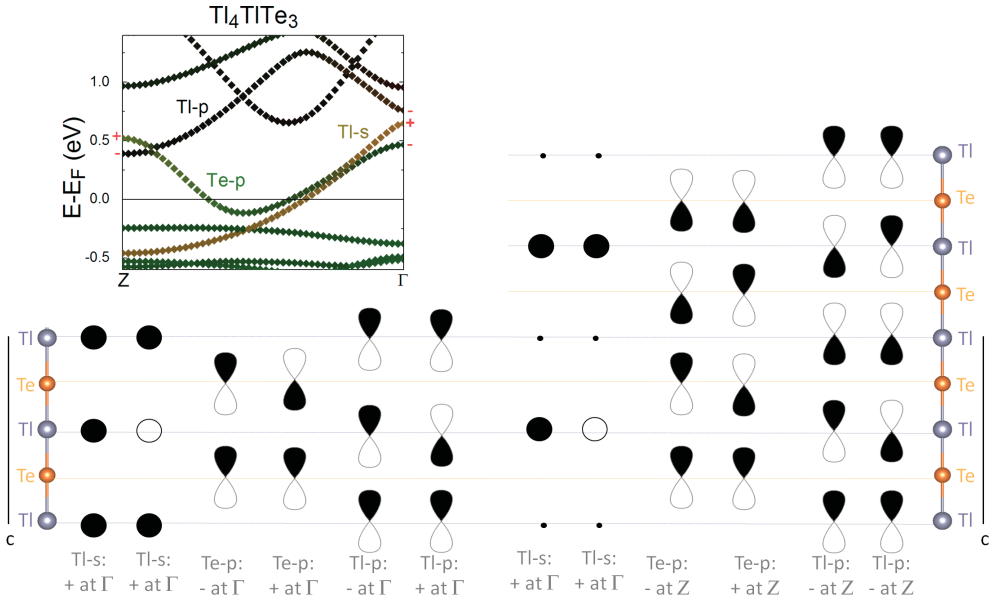

Figure 5.1.3: The orbital contribution to bands at TRIM points Z and Γ in Tl_5Te_3 are shown. The graphical inset shows the band structure with orbital contribution denoted by color. Band parities are indicated by + and - signs at the TRIM points.

Second, the bandgap above the E_F is not sufficient to be an insulator; if doped to that point, the material would best be described as a semi-metal. Therefore Tl_5Te_3 cannot be said to be a candidate topological insulator on the basis that it cannot be an insulator. However, there does appear to be sufficient evidence to suggest that Tl_5Te_3 may host $\mathbb{Z}_2$-protected, topologically non-trivial surface states. If electron-doped up to the gap at Z, this system would be a topological semi-metal due to high-lying valence band states at the Γ point. The resulting situation is thus similar to that found in pure antimony, which is a semi-metal with topologically protected surface states that becomes a topological insulator when doped with Bi [6].

5.2 Experimental visualization of a surface state

To confirm this prediction experimentally, we have synthesized crystals of Tl_5Te_3 and related electron-doped compounds for study of their electronic structure using angle-resolved

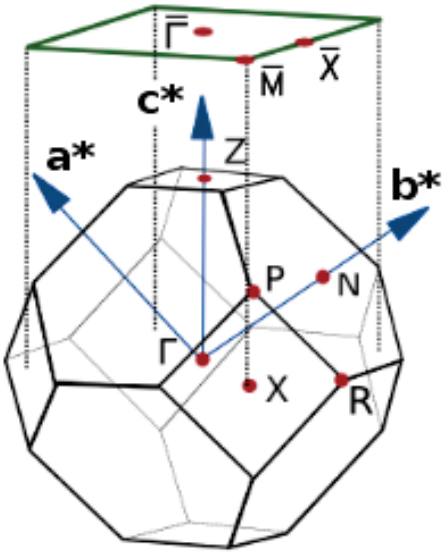

Figure 5.2.1: The three-dimensional bulk Brillouin zone of a body-centered tetragonal unit cell with the two-dimensional surface Brillouin zone projection expected for a c face cut is shown. The 2DBZ zone center is the $\overline{\Gamma}$, which is the projection of both the Γ and Z time-reversal invariant points of the three-dimensional bulk Brillouin zone.

photoelectron spectroscopy (ARPES, see Section 2.4). Single crystals were prepared in the manner described in Section 4.1 using a modified Bridgman method in an optical floating-zone furnace (Section 2.1). ARPES measurements were performed at the Synchrotron Radiation Center in Wisconsin at the U3 beamline with a VG Scienta R4000 electron analyzer at a base temperature of $T = 30$ K and a pressure of 8×10^{-11} torr as well as a lab-based ARPES system with a VG Scienta R4000 analyzer and VUV5000 helium plasma discharge lamp ($h\nu$ = 21.2 and 40.8 eV) and monochromator at a temperature of $T = 20$ K and a base pressure of 6×10^{-11} torr. Samples were cleaved *in situ* along the c axis in ultra-high vacuum in order to expose atomically clean surfaces.

Note that ARPES measurements, being surface measurements, are taken in two dimensions. Practically, this measurement technique means that instead of directly probing the bulk Brillouin zone, the two-dimensional surface Brillouin zone is measured (sometimes called 2DBZ). The projection from bulk to surface Brillouin zone for a c face cut is illustrated in Figure 5.2.1. In the 2DBZ zone center is the $\overline{\Gamma}$, which is the projection of both the Γ and Z time-reversal invariant points of the three-dimensional bulk Brillouin zone. A band parity inversion at Z in the three-dimensional bulk Brillouin zone will manifest in linearly

dispersing surface states around $\overline{\Gamma}$ in the two-dimensional surface Brillouin zone of the *c* face.

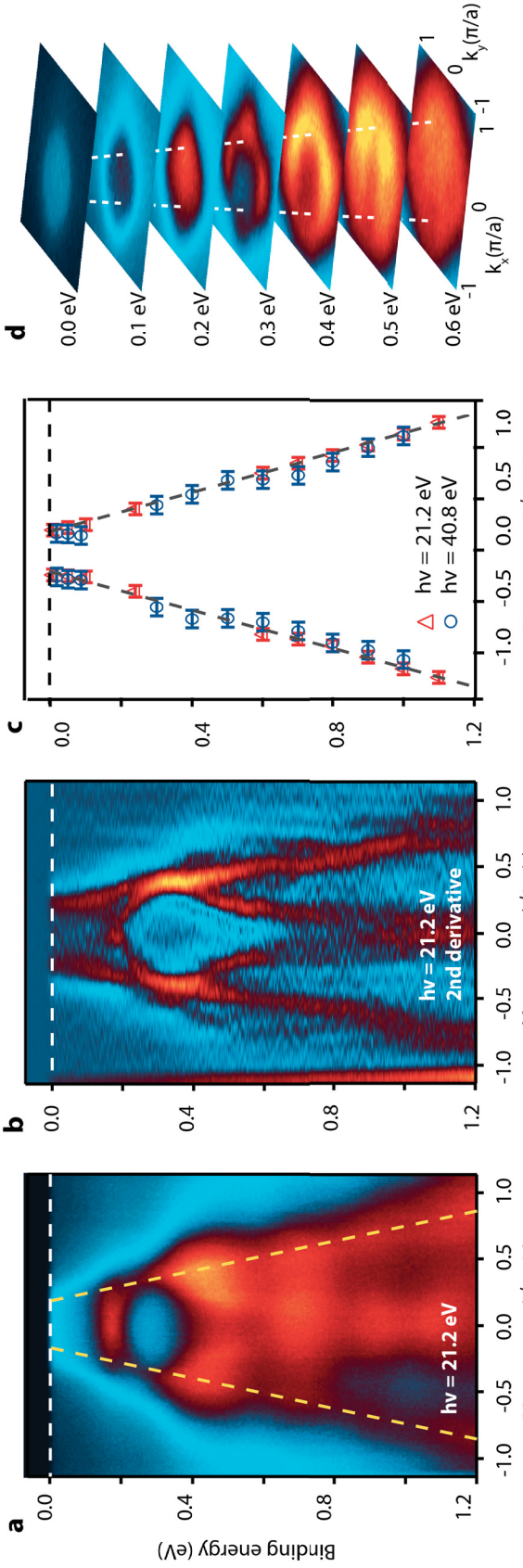

Figure 5.2.2: Dirac-like surface states (dashed lines) in the topological superconductor Tl_5Te_3. (a) ARPES spectrum taken with He Iα ($h\nu = 21.2$ eV) photons along the (0,0) – (π, π) direction showing the coexistence of prominent bulk states (heavy curved features) and a linearly dispersing surface state (yellow dashed lines) near E_F. (b) Second derivative plot of the measured experimental data shows the the surface state (linear features) more clearly resolved, as well as the bulk states (curved features). (c) Momentum-dispersion-curve fits for the data taken with He Iα and He IIα ($h\nu = 21.2$ eV and 40.8 eV) photons show no substantial dependence of the surface state on photon energy, i.e., it is "linearly dispersed" (dashed lines). (d) Iso-energy maps of intensity versus momentum in the k_x-k_y plane at a series of binding energies illustrate the presence of a single Dirac cone feature (white dashed lines) centered at the zone center. The Dirac cone exhibits fourfold warping away from the Dirac point, consistent with the tetragonal crystal symmetry of these materials.

In Figure 5.2.2, we show ARPES data for Tl_5Te_3 measured at $T = 20$ K and 30 K using a helium discharge lamp and monochromatic synchrotron radiation. The most prominent feature is an intense, linearly dispersing (Dirac-like) band centered at a momentum of (k_x = 0, k_y = 0), or $\overline{\Gamma}$ of the two-dimensional surface Brillouin zone. We observe this feature at the center of numerous 2DBZs, and only a single such feature in each zone. We identify this feature as a surface state based on several distinct pieces of evidence. First, the values of its extracted Fermi velocity and Fermi wavevector are insensitive to incident photon energy in both compounds (Figure 5.2.2(c)), indicating that these states are non-dispersive in k_z, characteristic of a surface state. In contrast, we additionally observe broad diffuse bands showing substantial changes with photon energy, as expected for bulk valence bands which disperse strongly along k_z. These observed bulk states are consistent with our first-principles calculations (Section 5.1), as well as the three-dimensional structure of these compounds. Furthermore, the Dirac-like feature is present and always centered at (0,0) of the 2DBZ, rather than the center of the three-dimensional bulk Brillouin zone as would be expected for a bulk-derived state.

We therefore detect a surface state in Tl_5Te_3 consistent with DFT predictions of spin-orbit driven band parity inversion at the Z time-reversal invariant momentum, which indicates non-trivial $\mathbb{Z}_2$ topology. However, one must consider the possibility a surface state exists in this material due to some other mechanism. A defining characteristic of a $\mathbb{Z}_2$ topological surface state is that it is spin-momentum locked; thus, in a mapping of the Brillouin zone such as ARPES provides, there is only one spin band at each momentum. In contrast, most electronic states exist in duplicate, having both spin-up and spin-down electrons. Evidence that the surface state contains only one spin band at any given momentum would therefore strongly suggest the state to be a $\mathbb{Z}_2$ topological surface state. To this end, we observe that the surface state shows no detectable Rashba-type spin splitting despite the strong spin-orbit coupling of these materials, a fact which strongly suggests that the surface state is spin-polarized.The Rashba effect is when, due to spin-orbit coupling,

the two composite spin-up and spin-down bands of a surface state are split as a function of momentum. Because the effect scales with the force of atomic spin-orbit coupling, if there were two spin bands in the surface state in question, one would expect the Rashba splitting to be apparent due to the heavy elements of Tl_5Te_3. The lack of Rashba splitting therefore suggests the surface state is spin-momentum locked, denoting a $\mathbb{Z}_2$ topological surface state. Spin-resolved ARPES is a potential future avenue to prove the spin-polarized nature of these surface states.

The existence of a single such non-spin-degenerate Dirac cone centered at the (0,0) time-reversal invariant point of the surface Brillouin zone is a hallmark of a surface state protected by a $\mathbb{Z}_2$ topology. As such, our measurements provide direct experimental evidence for the existence of topologically protected surface states in Tl_5Te_3. First principles DFT calculations support this conclusion. We therefore establish $[Tl_4]MTe_3$ as an entirely new materials system to host $\mathbb{Z}_2$ topologically non-trivial phases, and the first to additionally host bulk, intrinsic superconductivity.

The Tl_5Te_3 topological surface state displays a number of attractive features. As in the bismuth chalcogenide topological insulators [7], there is only a single topological state per surface Brillouin zone in Tl_5Te_3. Only the bottom section of the Dirac cone is visible, and the extrapolated Dirac point sits 0.21(1) eV above the Fermi level. The Dirac cones exhibit a four-fold warping away from the Dirac point consistent with the material's tetragonal symmetry (Figure 5.2.2(d)), akin to the six-fold warping in known trigonal topological insulators [8]. Additionally, the physical surface appears experimentally to be more robust against the effects of adsorbates than the bismuth chalcogenides [9], with no significant time- or pressure-dependent changes of this doping level observed during ARPES measurements, which may prove to be an attractive feature for utilizing these surface states in future applications.

5.3 Topological character of $[Tl_4]Tl_{1-x}Sn_xTe_3$

Several different $[Tl_4]MTe_3$ compounds were synthesized and prepared for ARPES. As ARPES relies on a freshly cleaved surface (Section 2.4) and $[Tl_4]MTe_3$ has a highly three-dimensional perovskite-like structure (Chapter 3) (which does not always cleave perfectly at the intended face), the only compounds for which we achieved sufficient reproducible data were Tl_5Te_3 and $Sn_xTl_{1-x}Tl_4Te_3$. $Sn_xTl_{1-x}Tl_4Te_3$ samples were prepared by heating elemental Tl, Te, and Sn (NOAH Technologies, 99.9%) in a vacuum-sealed silica ampuole to 540°C, holding for 24 h, followed by slow cooling (2°C/h). Single crystals of $Sn_xTl_{1-x}Tl_4Te_3$ suitable for ARPES measurements were obtained from the ingot after slow cooling. Compositions of the single crystals were assumed to be homogenous with the bulk ingot, the composition of which was determined to be $[Tl_4](Tl_{0.4}Sn_{0.6})Te_3$ by comparison to Rietveld refinement of high-resolution synchrotron x-ray diffraction data. ARPES data were taken in the same manner as for Tl_5Te_3 (Section 5.2).

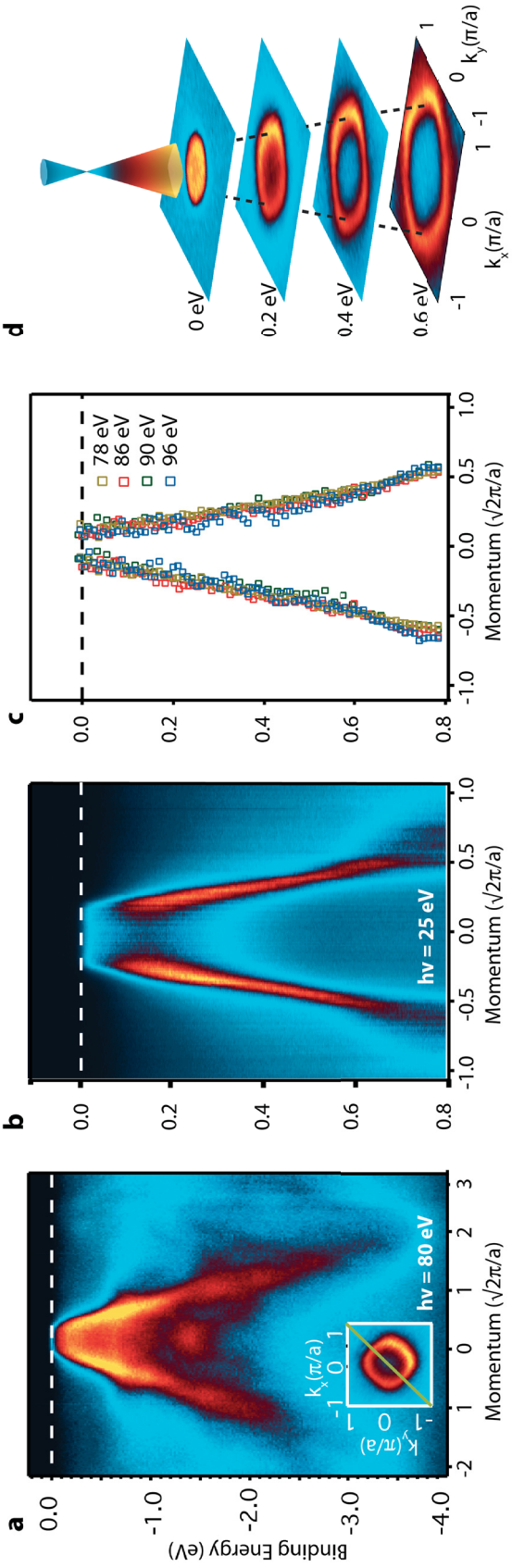

Figure 5.3.1: Dirac-like surface state in $[Tl_4](Tl_{0.4}Sn_{0.6})Te_3$. (a) ARPES spectrum taken along the (0,0) – (π,π) shows the electronic states over a wide energy range, including bulk states and a linearly dispersing surface state which evolves into a surface resonance upon intersecting the bulk states. (b) Expanded view of the Dirac-like surface state within the projected bulk band gap. (c) Fits to the dispersion at various photon energies reveal no substantial dispersion along k_z. (d) Momentum-resolved intensity maps plotted at different binding energies, which suggest the bottom portion of a single Dirac cone centered at the zone center, consistent with a topological surface state, with a square warping at higher binding energies, reflecting the tetragonal crystal symmetry.

These ARPES results (Figure 5.3.1) show that the Dirac-like surface states observed in Tl_5Te_3 survive in the tin-doped derivative, $[Tl_4](Tl_{0.4}Sn_{0.6})Te_3$. Like in Tl_5Te_3, we observe a single intense, linearly dispersing band with no Rashba splitting centered at $\overline{\Gamma}$ in the 2DBZ in a number numerous 2DBZs. There is significantly less bulk state signature evident in the measurements, suggesting a bulk band gap. The extrapolated Dirac cones of $[Tl_4](Tl_{0.4}Sn_{0.6})Te_3$ and Tl_5Te_3 are similar. Both exhibit a four-fold warping away from the Dirac point (Figures 5.2.2(d) and 5.3.1(d)) Interestingly, there is only a small change in the position of the Fermi level relative to the extrapolated position of the Dirac point: the extrapolated Dirac point sits 0.21(1) eV and 0.20(2) eV above the Fermi level for Tl_5Te_3 and $[Tl_4](Tl_{0.4}Sn_{0.6})Te_3$, respectively. The primary experimental effect observed upon doping with tin is an increase in the dispersion of the surface state: the extracted Fermi velocity of 3.0(2) eV Å for Tl_5Te_3 increases to 4.6(2) eV Å in $[Tl_4](Tl_{0.4}Sn_{0.6})Te_3$, and the wavevector correspondingly decreases from 0.07(1) $Å^{-1}$ to 0.04(1) $Å^{-1}$.

DFT calculations shown in Figure 5.3.2 on $SnTl_4Te_3$ explain these observations. Because Sn favors a 2+ oxidation state, it replaces the Tl^{2+} octahedral metal center isovalently, and thus the electronic structure is not greatly affected. One expects the E_F to increase relative to the bands because Sn has more valence electrons than Tl (4 compared to 3, or, considering Sn^{2+} and Tl^{2+}, 2 compared to 1). In contrast to Tl_5Te_3, in $SnTl_4Te_3$ a $\sim$0.7 eV band gap is predicted at the Z point: the separation between the valence and conduction bands increases with increasing x in $Sn_xTl_{1-x}Tl_4Te_3$, and prevents spin orbit coupling from inducing a band parity inversion. Consequently, for some value of x in the $[Tl_4](Tl_{1-x}Sn_x)Te_3$ series, there is a topological phase transition, similar to what is found for the $Bi_{1-x}Sb_x$ solid solution [6]. As long as x is less than the threshold value, the spin-orbit driven band inversion is maintained, but the dispersion of the surface state increases with increasing x, as experimentally observed. The position of the Fermi level relative to the Dirac point therefore changes little because, even though electrons are being added to the system, the number of states per unit energy is decreasing due to the increased disper-

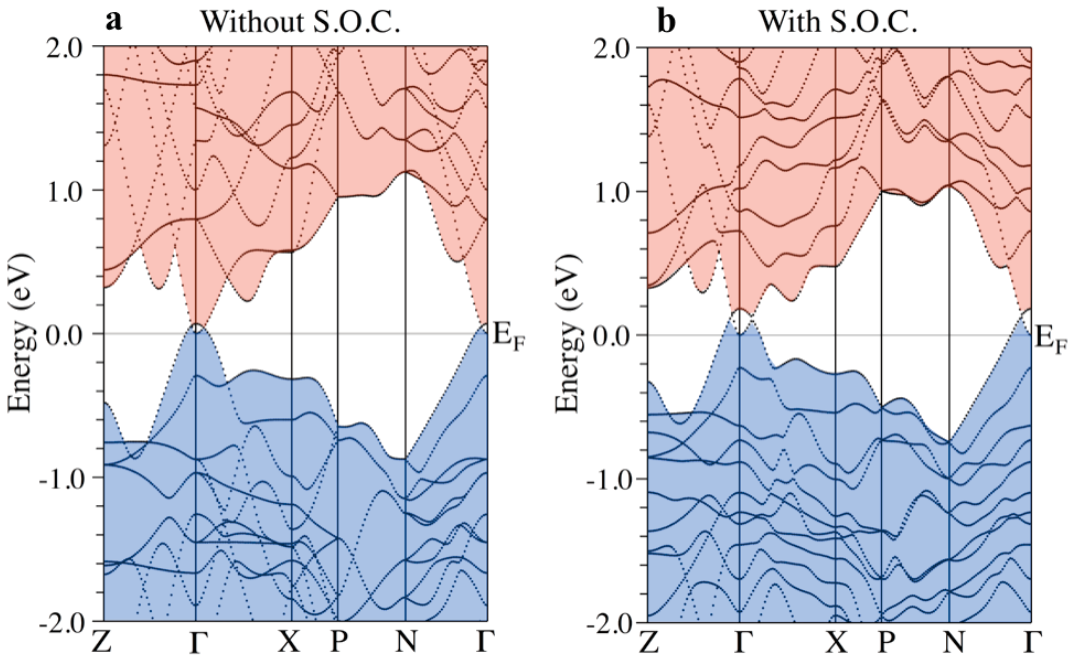

Figure 5.3.2: The band structure of $SnTl_4Te_3$, calculated from first principles DFT both without (a) and with (b) spin-orbit interactions. Shading denotes bands arising from valence (blue) and conduction (pale red) band states. Unlike the band structure of Tl_5Te_3, no band parity inversion at the Z point occurs due to spin-orbit coupling; rather, there is a bandgap at the Z momentum point between states of the same parity.

sion.

The bandstructure resulting from DFT calculations on the endmember $SnTl_4Te_3$ does not have a spin orbit driven band parity inversion at the Z point as for the Tl_5Te_3 endmember. There does appear to be a band inversion at the Γ point for $SnTl_4Te_3$, but this inversion is not driven by spin-orbit coupling as it is present in band structures calculated without spin-orbit coupling interactions. This inversion of bands is between orbitals of the same parity and therefore the $SnTl_4Te_3$ endmember is not indicated to be topologically non-trivial under the $\mathbb{Z}_2$ invariant (this is discussed in further detail in Section 6.6).

5.4 Conclusions and implications

5.4.1 Topological surface states in a new material and material class

Charge carriers in Dirac-like bands have a linear energy-momentum relationship described by the Dirac equation; they offer the unique opportunity to investigate the intersection of special relativity and quantum mechanics. However, materials exhibiting Dirac-like states are relatively rare, the most notable examples being graphene [10], $\mathbb{Z}_2$ topological insulators [11], and topological crystalline insulators [12]. In this chapter, we show the discovery of $\mathbb{Z}_2$ topological surface states a new material, the $[Tl_4]MTe_3$ (MTl_4Te_3) family. This family has an entirely different crystal structure than the known $\mathbb{Z}_2$ topological insulators, which all have trigonal symmetry in the active units, and moreover is a member of the largest known material structure type, perovskites.

Additionally, the physical surface of these materials appears experimentally to be more robust against the effects of adsorbates than the bismuth chalcogenides [9]. No significant time- or pressure-dependent changes of this doping level are observed during ARPES measurements, which may prove to be an attractive feature for utilizing these surface states in these materials in future applications.

Related to the work presented in this chapter, we note that $PbTl_4Te_3$ and $BiTl_9Te_6$ have been computationally predicted to be strong topological insulators [13].

5.4.2 First coexistence with bulk intrinsic superconductivity

Tl_5Te_3 is the first known material to host non-trivial $\mathbb{Z}_2$ topology and bulk, instrinsic superconductivity. Materials which combine non-trivial band topologies with superconductivity have the ability to test the predictions of new states of matter and open the field for new technologies such as quantum computing [14–17], but producing such materials has been a challenge [18–20]. This material has the additional advantages that it is relatively straight-

forward to synthesize and, being stoichiometric, to computationally model. (Attempts at inducing superconductivity in known $\mathbb{Z}_2$ topological insulators through doping or proximity [18–20] cannot be easily modeled with DFT.) It must be noted, however, that we have only observed $\mathbb{Z}_2$ topological surface states and superconductivity in the same material; we have not observed the two correlated electronic phenomena simultaneously. It is possible that Tl_5Te_3 and/or others it the $[Tl_4]MTe_3$ family undergo a transition between the superconducting temperatures ($T_c = 2.4$ K for stoichiometric Tl_5Te_3) and those temperatures at which surfaces states were detected ($T = 20$ K and 30 K). A structural transition in Tl_5Te_3 is unlikely based on the data we have already gathered: nPDF data (Section 3.4) show no evidence of a structural transition down to $T = 15$ K, and heat capacity shows no abrupt transitions other than the lambda-anomaly associated with the superconducting transition (Section 4.3). It therefore is a reasonable but unproven assumption that superconductivity and topological surface states may exist in this material. Nicholas Laurita in the Armitage lab of the Johns Hopkins University is performing microwave cavity measurements on the superconducting samples which provide preliminary evidence of the superconductivity coexisting with a surface state in this family.

Samples of Tl_5Te_3 and $Sn_xTl_{1-x}Tl_4Te_3$ have been provided to collaborator Nicholas Laurita, who is employing highly sensitive microwave cavity perturbation measurements using a He-3 superconducting microwave cavity resonator system to study the superfluid density of Tl_5Te_3 and $Sn_xTl_{1-x}Tl_4Te_3$ series in order to study the low energy electrodynamics of superconductivity in Tl_5Te_3 system.

5.4.3 Chemical bonding effecting topological phase transitions

The discovery of $\mathbb{Z}_2$ topological surface states in $[Tl_4]MTe_3$ (MTl_4Te_3) has broad implications and applications in the field of topological insulator research: the wide range of cations reported to substitute for the M site (and anions for tellurium) present a versatile range of experimentally accessible doping levels and resultant properties to examine. Pre-

liminary calculations indicate that the topological nature of $M\mathrm{Tl}_4\mathrm{Te}_3$ is very sensitive to structural parameters, suggesting that temperature-, pressure-, and/or strain-induced topological transitions may also exist in this material family. Already the $\mathrm{Sn}_x\mathrm{Tl}_{1-x}\mathrm{Tl}_4\mathrm{Te}_3$ series shows likely topological phase transition as a function of doping. DFT calculations (Section 5.3) suggest that a bandgap opening at the Z point prevents a band-parity inversion there from inducing non-trivial $\mathbb{Z}_2$ topology. The Z point of the Brillouin zone is the momentum, which, for this symmetry, correlates in real space to the c-axis. As shown in Chapter 3, the axial bonds (along the c axis) of the metal octahedra are distinct from the equatorial bond (in the a-b plane). I will show in Chapters 6 and 7 that these axial M-Ch bonds can be uniquely controlled and affected by chemical doping, which in turn affects the superconductivity and topology. Thus $[\mathrm{Tl}_4]M\mathrm{Te}_3$ is an ideal material in which to study the interplay of bonding, topology, and materials properties such as superconductivity, and affecting the bonding by chemical substitution offers an avenue to effect a topological phase transition.

Bibliography

[1] K. E. Arpino, D. C. Wallace, Y. F. Nie, T. Birol, P. D. C. King, S. Chatterjee, M. Uchida, S. M. Koohpayeh, J.-J. Wen, C. J. Fennie, K. M. Shen, and T. M. McQueen, Phys. Rev. Lett. **112**, 017002 (2014).

[2] L. Fu and C. L. Kane, Phys. Rev. B **76**, 045302 (2007).

[3] P. Blaha, K. Schwarz, G. K. H. Madsen, D. Kvasnicka, and J. Luitz, J. WIEN2k, An Augmented Plane Wave + Local Orbitals Program for Calculating Crystal Properties. (Vienna University of Technology, Vienna, Austria, 2001).

[4] J. P. Perdew, K. Burke, and M. Ernzerhof, Phys. Rev. Lett. **77**, 3865 (1996).

[5] G. Kresse and J. Furthmüller, Phys. Rev. B **54**, 11169 (1996).

[6] D. Hsieh, D. Qian, L. Wray, Y. Xia, Y.S. Hor, R. J. Cava and M. Z. Hasan, Nature **452**, 970 (2008).

[7] H. Zhang *et al.*, Nature Phys. **5**, 438 (2009).

[8] Y. L. Chen *et al.*, Science **325**, 178 (2009).

[9] M. Bianchi *et al.*, Nature Comm. **1**, 128 (2010).

[10] A. K. Geim and K. S. Novoselov, Nature Mat. **6**, 183 (2007).

[11] L. Fu, C. L. Kane, and E. J. Mele, Phys. Rev. Lett. **98**, 106803 (2007).

[12] L. Fu, Phys. Rev. Lett. **106**, 106802 (2011).

[13] M. Klintenberg, J. T. Haraldsen, and A. V. Balatsky, Applied Physics Research **6**(4), 31 (2014).

[14] A. C. Potter and P. A. Lee, Phys. Rev. B **85**, 094516 (2012).

[15] J. Linder, Y. Tanaka, T. Yokoyama, A. Sudbo, and N. Nagaosa, Phys. Rev. Lett. **104**, 067001 (2010).

[16] J. D. Sau, R. M. Lutchyn, S. Tewari, and S. Das Sarma, Phys. Rev. B **82**, 094522 (2010).

[17] S. Tewari, T. D. Stanescu, J. D. Sau, and S. Das Sarma, New J. Phys. **13**, 065004 (2011).

[18] G. Koren, T. Kirzhner, E. Lahoud, K. B. Chashka, and A. Kanigel, Phys. Rev. B **84**, 224521 (2011).

[19] Y. S. Hor *et al.*, Phys. Rev. Lett. **104**, 057001 (2010).

[20] S. Sasaki *et al.*, Phys. Rev. Lett. **109**, 217004 (2012).

6 Evolution of Structure, Physical Properties, and Topology in the $Sn_xTl_{1-x}Tl_4Te_3$ Series

The following chapter is based on the invited article "Superconducting Dome and Crossover to an Insulating State in $Sn_xTl_{1-x}Tl_4Te_3$ by K. E. Arpino, B. D. Wasser, and T. M. McQueen published in APL Materials Physical 3, 041507 (2015). [1]

This research investigates the $Sn_xTl_{1-x}Tl_4Te_3$ series, which our previous research suggests may topological phase transition [2]. The structural, superconducting, and electronic phase diagram of $Sn_xTl_{1-x}Tl_4Te_3$ is reported. Magnetization and specific heat measurements show bulk superconductivity exists for $0 \leq x \leq 0.4$. Resistivity measurements indicate a crossover from a metallic state at $x = 0$ to a doped insulator at $x = 1$. Universally, there is a large non-Debye specific heat contribution, characterized by an Einstein temperature of $\theta_E \approx 35$ K. Density functional theory calculations predict $x = 0$ to be a topological metal, while $x = 1$ is a topological crystalline insulator. The disappearance of superconductivity correlates with the transition between these distinct topological states.

6.1 Introduction

With the discovery of topological insulators, the importance of spin-orbit coupling in driving electronic phenomena has moved to the forefront of condensed matter physics [3–5]. Breaking time-reversal or inversion symmetry in a crystalline material can lift Kramers degeneracy of spins, resulting in chiral locking of spin and momentum displayed by topological features such as Dirac cones in the surface states of topological insulators and, more recently, in the three-dimensional cone of Dirac semi-metals [6–11]. Topological materials are now known to offer an exciting array of physical phenomenon, such as Fermi arc surface states and Majorana fermions, with a wealth of potential applications [12–15]. Many of these phenomena are predicted to occur at the convergence of topological states and other emergent states of matter. More recently, several candidate materials combining topological surface states and bulk superconductivity, including $Cu_xBi_2Se_3$ [16], Au_2Pb [17], and Tl_5Te_3 [2] have been experimentally proposed.

Topological phase transitions and their attendant effects, such as fractional charge and spontaneous mass acquisition, have been previously examined in $(Bi_{1-x}In_x)_2Se_3$ [18] and $BiTl(S_{1-x}Se_x)$ [19, 20]. The $Sn_xTl_{1-x}Tl_4Te_3$ series is also predicted to exhibit a doping-induced topological phase transition: calculations have indicated that $[Tl_4]TlTe_3$, but not $[Tl_4]SnTe_3$, harbors a non-trivial $\mathbb{Z}_2$ topological invariant when appropriately electron doped [2]. This series has the additional interest of harboring bulk superconductivity, as end-member $[Tl_4]TlTe_3$ superconducts below $T_c = 2.4$ K while $[Tl_4]SnTe_3$ does not superconduct.

Here we report the structural and electronic phase diagram of $[Tl_4]Tl_{1-x}Sn_xTe_3$ ($Sn_xTl_{1-x}Tl_4Te_3$) over the entire solid solution range $0 \leq x \leq 1$. Samples were prepared as previously reported [2], yielding cleavable polycrystalline boules. Magnetization and specific heat measurements show a superconducting dome upon substitution of Sn for Tl, with a maximum $T_c = 2.73(4)$ K at $x = 0.1$. From resistivity measurements, this superconducting dome is proximal to a crossover to an insulating state around $x \approx 0.5$. Throughout

the entire solid solution, there is a large non-Debye contribution to the lattice specific heat. Band structure calculations consistent with these experimental observations suggest that the system is transformed from a $\mathbb{Z}_2$ topological metal at x = 0 to a topological crystalline insulator at $x = 1$.

6.2 Structure of $Sn_xTl_{1-x}Tl_4Te_3$

Rietveld refinement of laboratory and synchrotron XRD data shows the entire $[Tl_4]Tl_{1-x}Sn_xTe_3$ ($Sn_xTl_{1-x}Tl_4Te_3$) series shares the perovskite-like structure of the $[Tl_4]TlTe_3$ (Tl_5Te_3) endmember, described in Chapter 3 (inset of Figure 6.2.1). Substitution of Sn for Tl occurs at the octahedral metal centers, resulting in $(Tl_{1-x}Sn_x)Te_6$ octahedra [2, 22]. No change of *I*4/*mcm* symmetry is observed across the $Sn_xTl_{1-x}Tl_4Te_3$ series. Though Sn has a smaller ionic radius than Tl, the structure seems robust even when small ions occupy the octahedral centers: full substitution of Sn in $SnTl_4Te_3$ is possible, and MTl_4Te_3 variants doped with even small first-row transition metal ions have been reported [21]. No periodic modulation of the octahedral centers due to size is expected if Sn substitutes in randomly. Moreover, substitution of Sn for Tl, full or partial, should not allow the negative Hubbard-U ion Tl^{2+} to relax to a more stable 1+ or 3+ oxidation state (the way that Bi^{3+} does in $BiTl_9Te_6$) because 2+ is a stable oxidation state for Sn and both 3+ and 1+ are not.

6.2.1 Lattice parameters

Figure 6.2.1 shows the evolution of lattice parameters as a function of Sn content. There has been some question about the doping limit and location, with previous reports variously claiming the maximum possible Sn content as ranging from 0.8 to 1.1 molar equivalents [22, 24, 26]. Our data clearly show a continuous evolution of lattice parameters up to $x = 1.0$, followed by a plateau when $x > 1$, demonstrating that substitution of up to one

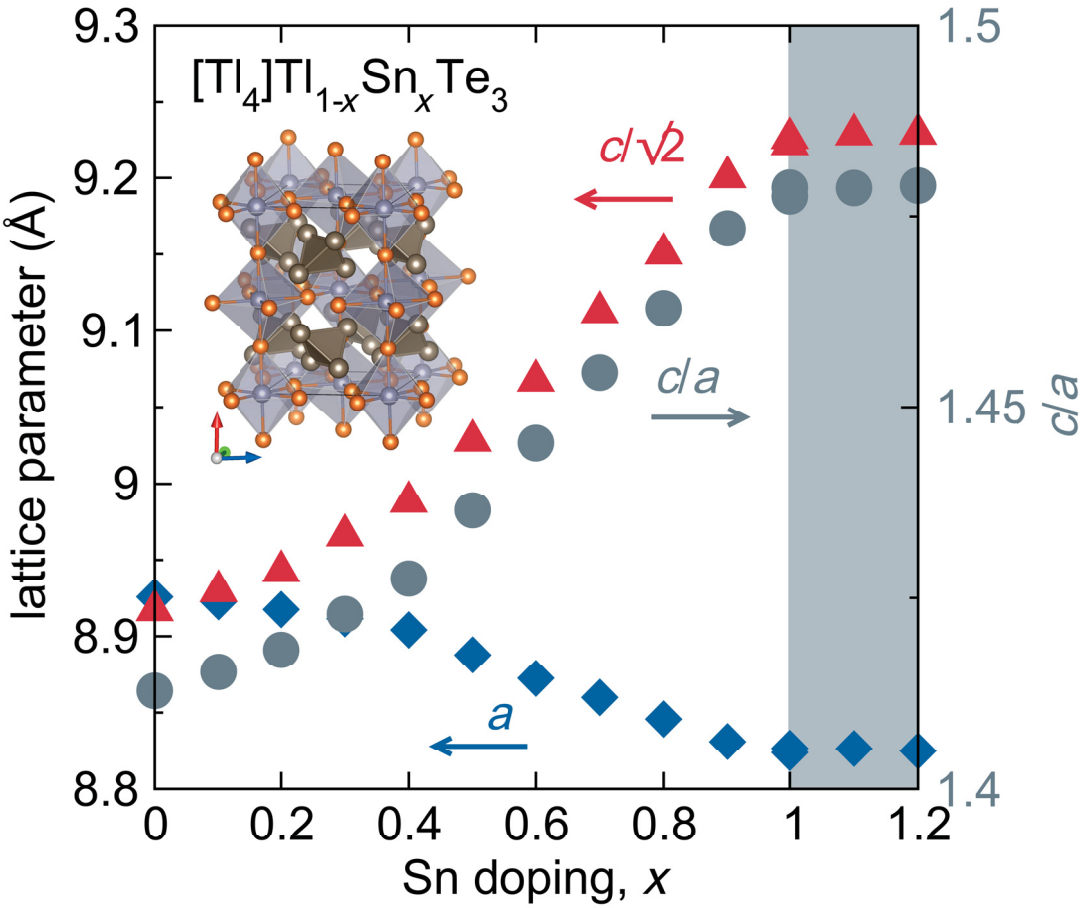

Figure 6.2.1: The lattice parameters of $[Tl_4]Tl_{1-x}Sn_xTe_3$ show continuous, but non-linear, evolution with increasing Sn content, with a solid solubility limit at $x = 1$. The c lattice parameters (red triangles) divided by a factor of $\sqrt{2}$ (a measure of tetragonal pseudo-cubicity) and the a lattice parameters (blue diamonds) are plotted on the leftmost axis, while the c/a ratio (gray circles) is plotted on the right axis. Inset: The material is a perovskite analogue, with $(Tl_{1-x}Sn_x)Te_6$ octahedra and interstitial $[Tl_4]$ tetramers. The octahedra are significantly rotated in an $a^0a^0c^-$ fashion [2, 23, 24]. The structure is visualized in the VESTA program [25].

molar equivalent of Sn for Tl is possible. The limit of $x = 1$ is consistent with charge counting: assuming dianionic Te, the formal charges are $[Tl_4]^{4+}$, Tl^{2+}, and Te^{2-}; divalent Sn^{2+} is then able to substitute for all divalent, but not monovalent, Tl, i.e, up to one molar equivalent. Though the trends in lattice parameters up to doping $x = 1.0$ is monotonic, they exhibit pronounced deviations from the linear behavior expected from Vegard's law. Rietveld analysis of powder diffraction data was used to elucidate the specific structural

changes with composition.

6.2.2 Bond lengths and intra-cellular changes

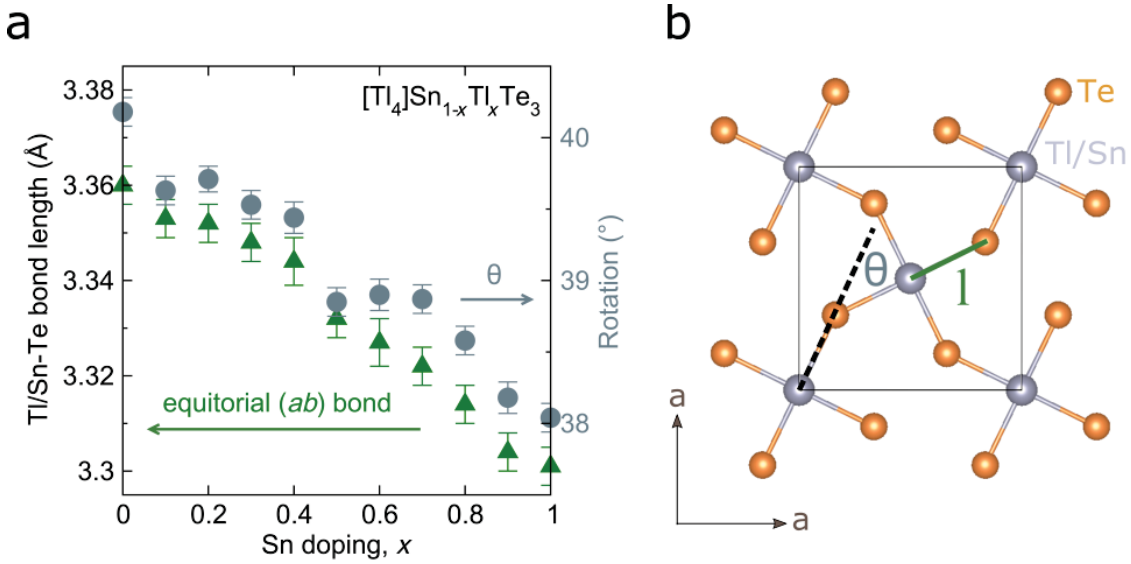

Figure 6.2.2: Detailed structural changes in the *a*-*b* plane as a function of doping in the $[Tl_4]Tl_{1-x}Sn_xTe_3$ series. (a) Equatorial (in-plane) octahedral bond distances between the metal center and tellurium in the *a*-*b* plane (green triangles) exhibit a linear decrease. The octahedral rotation (degrees different from straight) is plotted on the right axis, showing a linear decrease. (b) A figure of the structure illustrates the bond length and octahedral rotation measured. The structure is visualized in the VESTA program [25].

The non-linearity of the *a* lattice parameter arises due to a combination of two structural effects in the *a*-*b* plane highlighted in Figure 6.2.2. First, there is a linear reduction of the in-plane octahedral metal-tellurium distance (equatorial), as expected given the smaller size of Sn versus Tl. Second, there is a concomitant linear reduction of the degree of the octahedral rotations about the *c* axis, which likely arises from the need to maintain optimal bonding geometry to the interstitial Tl atoms. This linear decrease in rotation angle corresponds to a non-linear-decease in the distance between octahedral metal centers in the same plane (the *B*-sites), resulting in the non-linearity of the *a* lattice parameter.

More interesting is the non-linear, and positive, change of the *c* axis upon Sn substi-

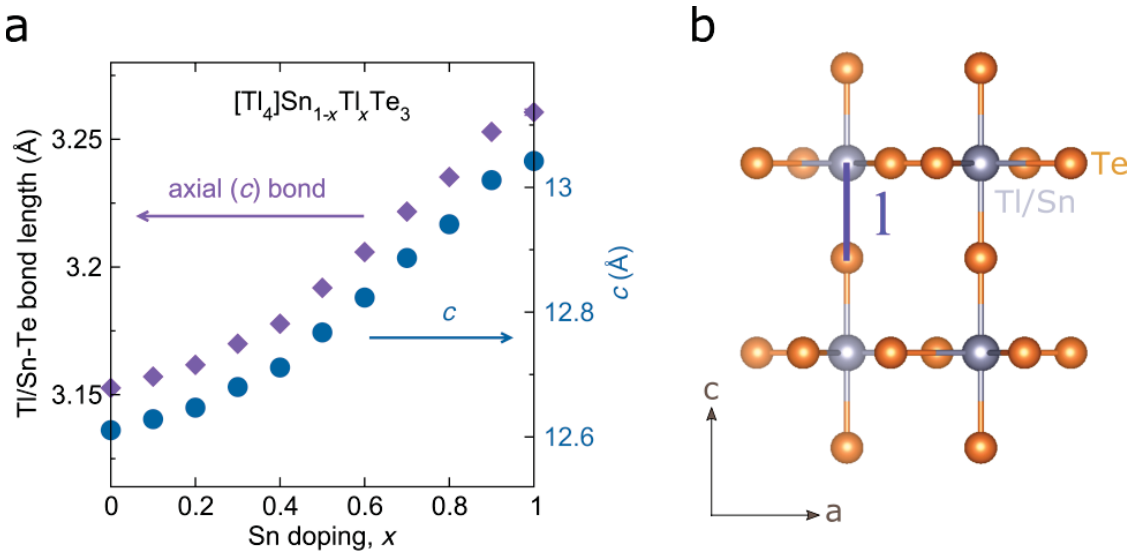

Figure 6.2.3: Detailed structural changes in the *c*-axis ("out of plane") as a function of doping in the $[Tl_4]Tl_{1-x}Sn_xTe_3$ series. (a) Octahedral bond distances between the metal center and the out-of-[*a*-*b*-]plane tellurium along the *c*-axis (purple diamonds) decrease non-linearly. (b) A figure of the structure illustrates the bond length measured. The structure is visualized in the VESTA program [25].

tution. Given the smaller size of Sn relative to Tl and their isovalency, a linear decrease is expected upon Sn substitution; instead, a non-linear increase is observed. Figure 6.2.3 shows the axial (out-of-plane) octahedral metal-tellurium distance increasing non-linearly with Sn substitution, which mirrors the change in *c*. In the reported *I*4/*mcm* unit cell, there are no internal degrees of freedom along this axis: octahedral metal centers occur at Wyckoff position at (0, 0, 1/2) and axial tellurium occur at Wyckoff position (0, 0, 1/4). The corresponding bond distance is therefore required to be precisely one-fourth of the lattice parameter *c* of the unit cell. However, the direct mirroring is not an artifact of an incorrect choice of symmetry: refining in lower-symmetry space group *I*4/*m*, which allows for movement of the axial Te along the *c* axis, does not offer a significant change in the bond length. Instead this trend likely reflects the differences in the covalency between Tl-Te and Sn-Te bonding.

6.3 Superconductivity in $Sn_xTl_{1-x}Tl_4Te_3$: a superconducting dome

The isovalent replacement of Tl^{2+} by Sn^{2+} at the octahedral metal center site dramatically modulates the physical properties. Figure 6.3.1(a) shows low field ac magnetization measurements for $0 \leq x \leq 0.4$, measured using a quantum design physical properties measurement system (QD-PPMS). Consistent with previous reports, [2, 28], the $x = 0$ endmember is superconducting with $T_c = 2.36(6)$ K. T_c increases initially with Sn substitution, to a maximum of $T_c = 2.73(4)$ K at $x = 0.1$, before falling for greater dopings of x. Only traces of superconductivity remain for $x > 0.4$. This is an example of a "superconducting dome" present in a variety of superconductors which may indicate a number of things, including proximity to a charge-density wave or a hidden quantum critical point. The bulk nature of the superconductivity is confirmed by the presence of a lambda anomaly in the low-temperature electronic specific heat [Figure 6.3.1(b)], measured using the semi-adiabatic pulse technique as implemented in a Quantum Design PPMS. The specific heat jump at T_c, $\Delta C_{el}/(\gamma T_c) = 1.6$, changes little as a function of doping and is close to the weak coupling Bardeen-Cooper-Schrieffer (BCS) value of 1.43 [29].

6.4 Resistivity measurements

Resistivity measurements (Figure 6.4.1) collected using a Quantum Design PPMS with a four-probe geometry and a constant excitation current show a non-monotonic change in electrical conductivity as a function of Sn content. Data below $T = 3$ K have been excluded due to the superconductivity of the low-x doped samples. The magnitude of the resistivity over most of the series is consistent with a semi-metallic or metallic state, while the highest doping ($x = 1$) is consistent with the behavior expected for a doped semiconductor. This transition from metallic towards insulating behavior upon Sn doping is in agreement with

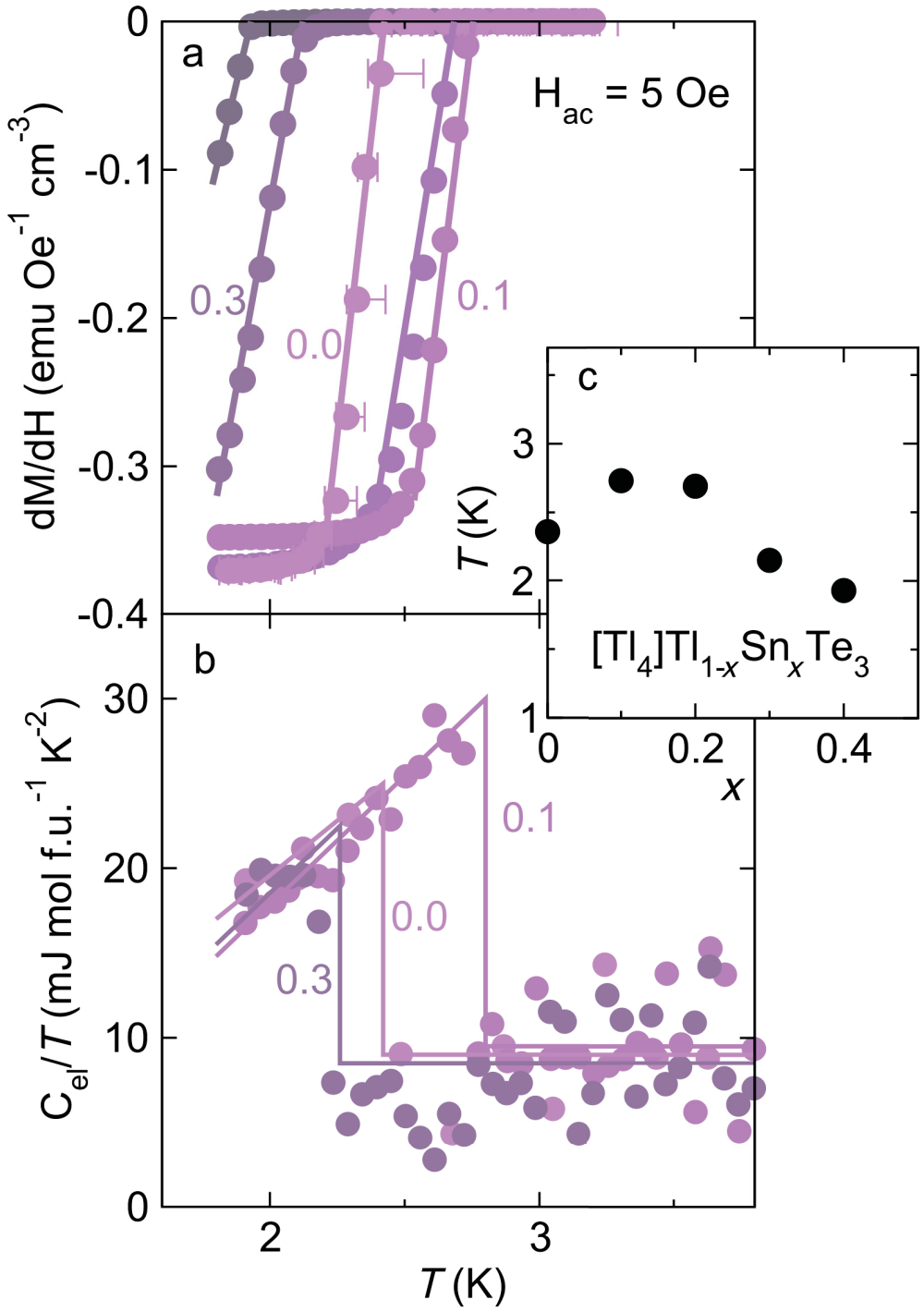

Figure 6.3.1: The superconductivity of compounds $0 \leq x \leq 0.4$ is shown in (a) the negative ac magnetic susceptibility response and (b) low-temperature heat capacity measurements. Equal entropy constructions on the electronic heat capacity illustrate the bulk nature of the superconductivity. (c) Plotting T_c as a function of doping x illustrates the so-called "superconducting dome."

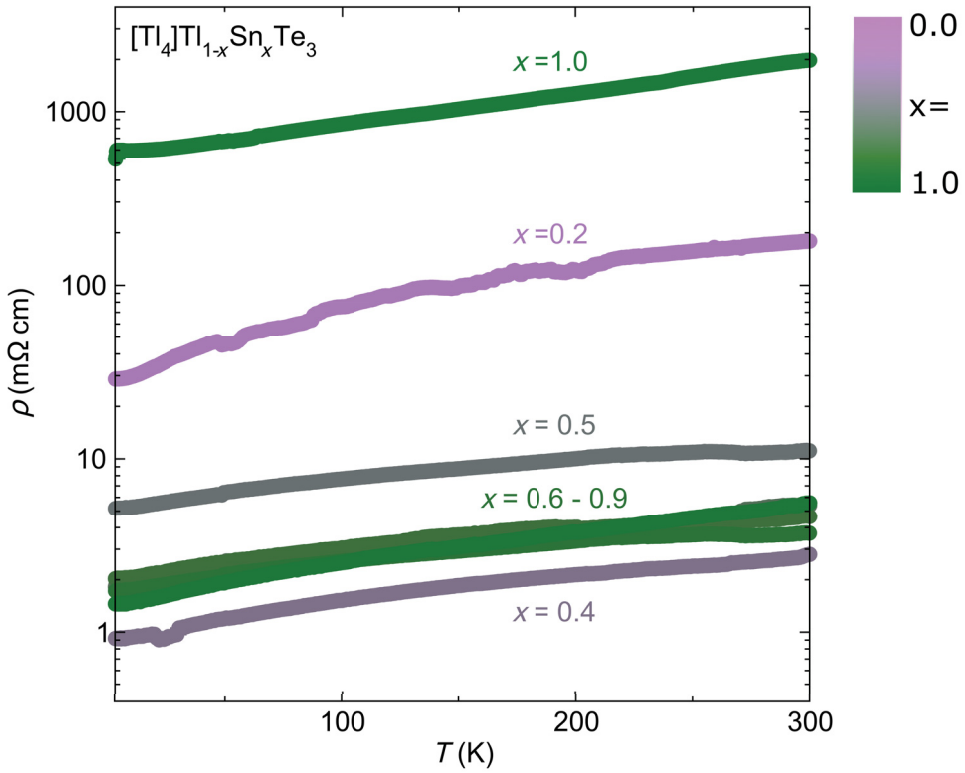

Figure 6.4.1: Resistivity measurements of the $Sn_xTl_{1-x}Tl_4Te_3$ series show a non-monotonic change in electrical conductivity for $T \geq 3K$ as a function of Sn content. Data from the fully Sn-doped end member is consistent with a semiconductor, while that of the majority of the series indicates semi-metallic or metallic states.

previous measurements [26]. There is a concomitant change in the shape of the temperature dependence which suggests a change in the dominant scattering mechanism across the series.

6.5 Heat capacity measurements

In addition to the structural changes, a substantial non-Debye lattice contribution was observed in the specific heat of all samples; Figure 6.5.1 shows the specific heat for the series of samples, plotted as C/T^3 vs. lnT [31]. The specific heat data are well described above T_c as one Debye mode, one Einstein mode, and an electronic heat contribution given by the Sommerfeld term [32]. The large Einstein contribution at low temperature obscures the

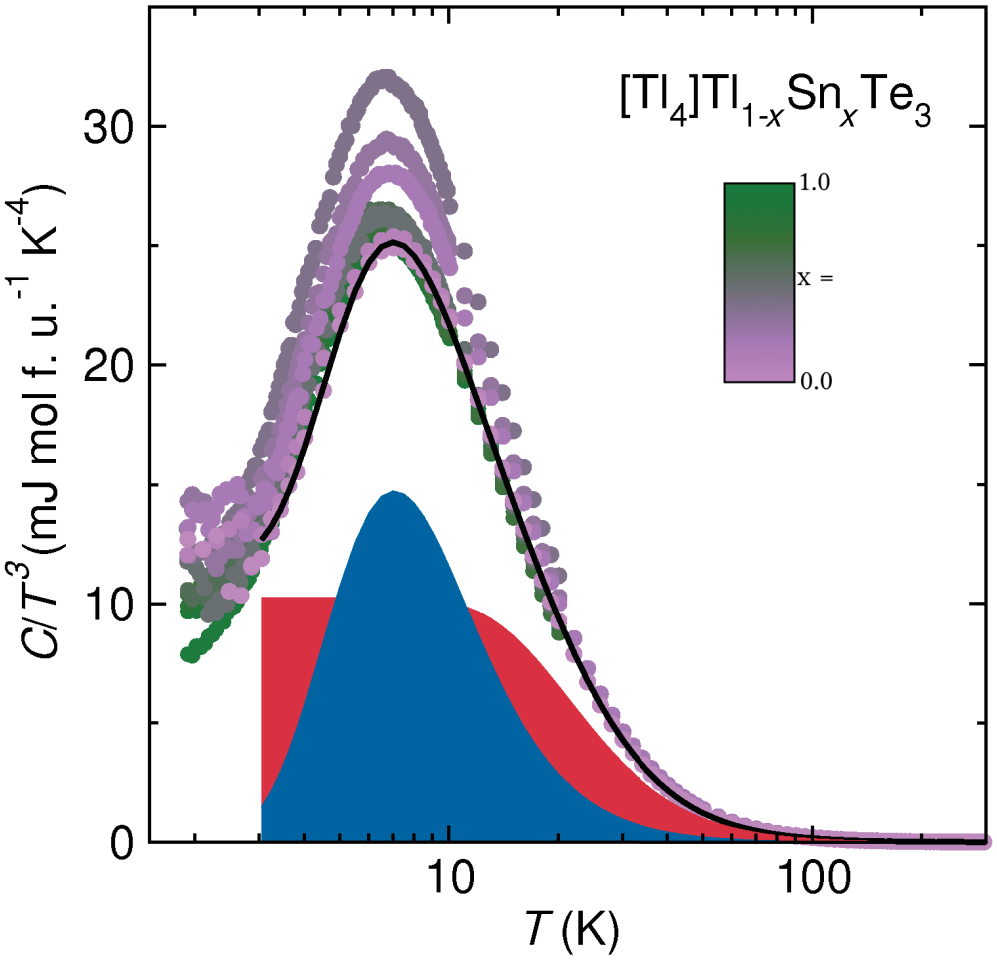

Figure 6.5.1: The lattice contributions to the heat capacity only vary slightly as a function of Sn content. However, there is a substantial non-Debye contribution centered at $T \approx 7$ K, which is well described as a single Einstein oscillator. The overall fit (black line) for $x = 0$, with corresponding Debye (red) and Einstein (blue) components, is shown.

precise behavior of the Sommerfeld coefficient with composition, but the electronic contribution appears to correlate with the superconducting T_c, with both showing a maximum at $x = 0.1$. The Debye component is characterized by a Debye temperature of $\theta_D = 97$ K - 117 K and 6.5 - 6.9 oscillators per formula unit. An increase in the Debye temperature upon Sn substitution is expected due to the lighter mass of Sn relative to Tl. The Einstein mode has parameters Einstein temperature of $\theta_E = 37$ K -33 K and 1.1 - 1.5 oscillators per formula unit, with a maximal contribution for $x = 0.4$, and likely originates from a low-lying optic

phonon mode. Such modes are commonly observed in ferroelectrics and materials near structural instabilities [33, 34]. As Tl^{2+} is a negative-U ion favoring charge disproportionation and Sn^{2+} can be lone-pair active, it is alluring to ascribe this Einstein contribution to a propensity toward charge order ($x = 0$) or off-centering of the *B*-site cation ($x = 1$). However, such an assignment is unlikely in this case since the total Einstein contribution shows little dependence on composition: it would be quite a coincidence for two different origins to produce a low-lying optic mode at the same energy. Instead, the fact that this contribution is consistent for all $0 \leq x \leq 1$ suggests the origin of instead lies within the interstitial [Tl_4] framework, the only units not directly disturbed by the Sn substitution at the *B*-site.

6.6 Prediction of toplogical character by DFT calculations

To gain insight into the origins of the changes across the series, density functional theory (DFT) calculations were performed on the two end-members using LDA+U as implemented in the full potential linearized augmented plane wave plus local orbitals (FP-LAPW-LO) code elk [35] and a 6x6x4 k-point mesh; the resulting band structures are plotted in Figure 6.6.1(a) (x =0) and Figure 6.6.1(b) (x = 1). These calculations were performed independently of those reported in Section 5.1. In agreement with the previous calculations that did not include the negative U effect of Tl^{2+} [2], [Tl_4]$TlTe_3$ is found to contain both electron and hole pockets, and is best described as a metal. Due to the *I*4/*mcm* symmetry, to calculate the $\mathbb{Z}_2$ topological invariant, it is only necessary to consider the states at the Γ and Z time reversal invariant points in the Brillouin zone. Multiplying the parities of all *occupied* states at Z and Γ for [Tl_4]$TlTe_3$ give a total parity of $\mathbb{Z}_2 = 1$; i.e., Tl_5Te_3 is topologically nontrivial. This is due to a strong covalency between Tl *s* and Te *p* states that pushes a negative-parity Te-*p* derived band above E_F at the Γ point. In contrast, $SnTl_4Te_3$

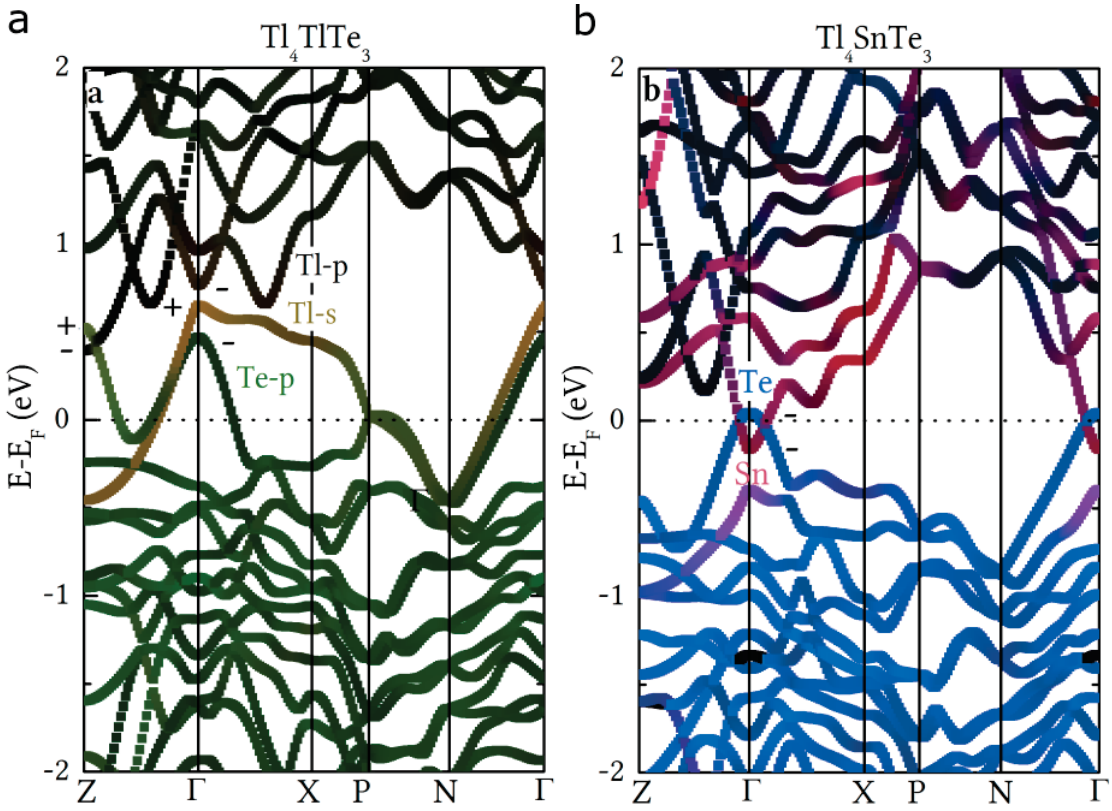

Figure 6.6.1: DFT-calculated band structures accounting for spin orbit coupling for (a) $[Tl_4]TlTe_3$, U = 5 eV, and (b) $[Tl_4]SnTe_3$. Shading in (a) indicates contributions from atomic orbital contributions (labeled in respective colors in figure), while shading in (b) indicates contributions from the atoms (labeled in respective colors in figure). The parity of states near the Fermi level relevant to determining the topological class are given by $\pm$ symbols. $[Tl_4]TlTe_3$ is found to have a $\mathbb{Z}_2$ invariant of -1 and is a topological metal, while $[Tl_4]SnTe_3$ is topologically trivial but has an inversion of Sn and Te derived states at Γ that produce a topological crystalline insulator state.

is topologically trivial under the $\mathbb{Z}_2$ invariant: there is a band inversion at the Γ point, but it is between two bands of negative parity and does not affect the $\mathbb{Z}_2$ invariant. (Additionally, recalling Figure 5.3.2, one sees that this inversion is not due to spin-orbit coupling, which is commonly believed to drive band inversions in non-trivial $\mathbb{Z}_2$ topological surface states.) However, the inversion at Γ does move Sn p states into the valence band and Te p states into the conduction band. The result is analogous to the band inversion in SnTe, and is expected to give rise to topological crystalline insulator state [6]. Note that such a change in topological class may obfuscate the origin of surface states detected in $Sn_xTl_{1-x}Tl_4Te_3$

samples; either a single band parity inversion could cause non-trivial $\mathbb{Z}_2$ surface states or crystalline symmetry elements could cause topological crystalline insulator states.

6.7 $Sn_xTl_{1-x}Tl_4Te_3$ phase diagram

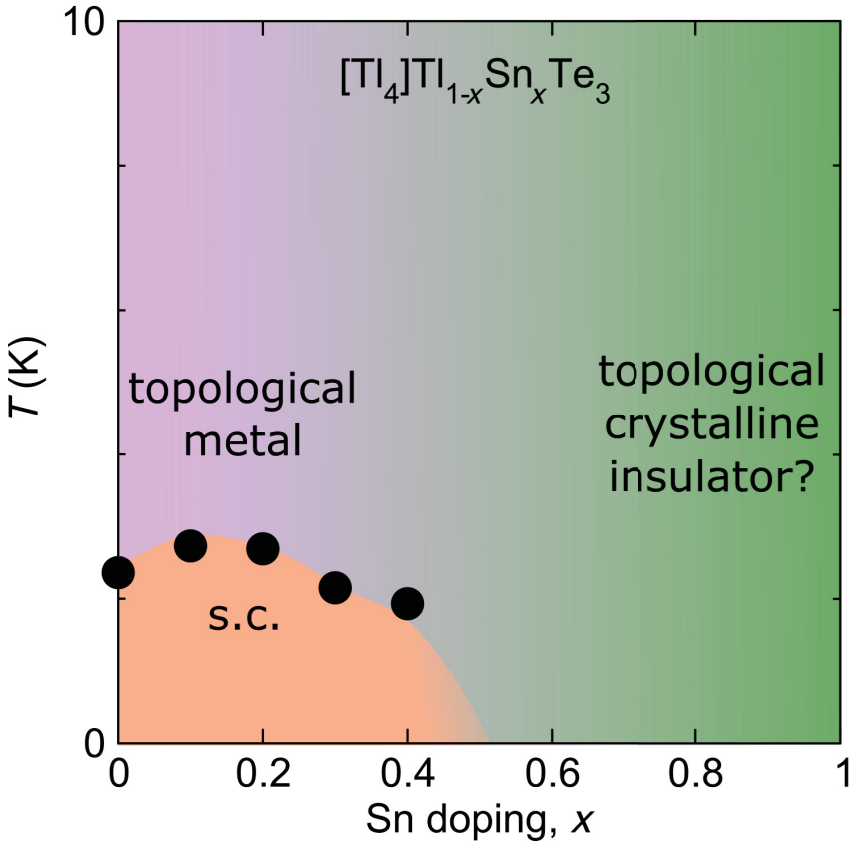

Figure 6.7.1: Phase diagram of $Sn_xTl_{1-x}Tl_4Te_3$ showing the superconducting dome proximal to a transition from a topological metal to topological crystalline insulator.

A summary of these experimental and computational results is presented in Figure 6.7.1. Substitution of Sn for Tl in $[Tl_4]TlTe_3$ results in the rise and fall of superconductivity in proximity to a crossover between a topological metal and a topological crystalline insulator. Further work is required to elucidate the precise origin of the large non-Debye lattice contribution to the specific heat observed across the series. We expect these results to mo-

tivate significant additional studies into materials that couple topological surface states to other degrees of freedom.

6.8 Acknowledgments

This work in this chapter was supported by the David and Lucile Packard Foundation and benefited from structural studies performed using beamlines 11-BM-B and 11-ID-B of the Advanced Photon Source, a U.S. Department of Energy (DOE) Office of Science User Facility operated for the DOE Office of Science by Argonne National Laboratory under Contract No. DE-AC02-06CH11357. David Wallace and John Sheckelton are acknowledged and thanked for technical assistance.

Bibliography

[1] K. E. Arpino, B. D. Wasser, and T. M. McQueen, APL Mat. **3**, 041507 (2015). (invited)

[2] K. E. Arpino, D. C. Wallace, Y. F. Nie, T. Birol, P. D. C. King, S. Chatterjee, M. Uchida, S. M. Koohpayeh, J.-J. Wen, C. J. Fennie, K. M. Shen, and T. M. McQueen, Phys. Rev. Lett. **112**, 017002 (2014).

[3] L. Fu, C. L. Kane, and E.J. Mele, Phys. Rev. Lett. **98**, 106803 (2007).

[4] D. Hsieh, D. Qian, L. Wray, Y. Xia, Y.S. Hor, R. J. Cava and M. Z. Hasan, Nature **452**, 970 (2008).

[5] Y Xia, D. Qian, D. Hsieh, L. Wray, A. Pal, H. Lin, A. Bansil, D. H. Y. S. Grauer, Y. S. Hor, R. J. Cava, and M. Z. Hasan, Nat. Phys. **5**, 398 (2009).

[6] L. Fu, Phys. Rev. Lett. **106**, 106802 (2011).

[7] Z. K. Liu, J. Jiang, B. Zhou, Z. J. Wang, Y. Zhang, H. M. Weng, D. Prabhakaran, S-K. Mo, H. Peng, P. Dudin, T. Kim, M. Hoesch, Z. Fang, X. Dai, Z. X. Shen, D. L. Feng, Z. Hussain, and Y. L. Chen, Nat. Mater. **13**, 677 (2014).

[8] M. Neupane, S.-Y. Xu, R. Sankar, N. Alidoust, G. Bian, C. Liu, I. Belopolski, T.-R. Chang, H.-T. Jeng, H. Lin, A. Bansil, F. Chou, and M. Z. Hasan, Nat. Comm. **5**, 3786 (2014).

[9] S. Borisenko, Q. Gibson, D. Evtushinsky, V. Zabolotnyy, B. Buechner, and R. J. Cava, Phys. Rev. Lett. **113**, 027603 (2014).

[10] Z. K. Liu, B. Zhou, Y. Zhang, Z. J. Wang, H.M. Weng, D. Prabhakaran, S.-K. Mo, Z. X. Shen, Z. Fang, X. Dai, Z. Hussain, and Y .L. Chen, Science **343**, 864 (2014).

[11] Q. D. Gibson, L. M. Schoop, L. Muechler, L.S. Xie, M. Hirschberger, N. P. Ong, R. Car, and R. J. Cava, unpublished, arXiv:1411.0005 (2014).

[12] A. C. Potter and P.A. Lee, Phys. Rev. B **85**, 094516 (2012).

[13] X. Wan, A. M. Turner, A. Vishwanath, and S. Y. Savrasov, Phys. Rev. B **83**, 205101 (2011).

[14] J. D. Sau, R. M. Lutchyn, S. Tewari, and S. Das Sarma, Phys. Rev. B **82**, 094522 (2010).

[15] D. E. Kharzeev and H.-U. Yee, Phys. Rev. B **88**, 115119 (2013).

[16] S. Sasaki, M. Kriener, K. Segawa, K. Yada, Y. Tanaka, M. Sato, Y. Ando, Phys. Rev. Lett. **107**, 217001 (2011).

[17] L. M. Schoop, L. S. Xie, R. Chen, Q. D. Gibson, S. H. Lapidus, I. Kimchi, M. Hirschberger, N. Haldolaarachchige, M. N. Ali, C. A. Belvin, T. Liang, J. B. Neaton, N. P. Ong, A. Vishwanath, and R. J. Cava, unpublished, arXiv:1412.2767 (2014).

[18] M. Brahlek, N. Bansal, N. Koirala, S-Y. Xu, M. Neupane, C. Liu, M. Z. Hasan, and S. Oh, Phys. Rev. Lett. **109**, 186403 (2012).

[19] S.-Y. Xu, Y. Xia, L. A. Wray, S. Jia, F. Meier, J.H. Dil, J. Osterwalder, B. Slomski, A. Bansil, H. Lin, R. J. Cava, and M. Z. Hasan, Science, **332**, 560 (2011).

[20] T. Sato, K. Segawa, K. Kosaka, S. Souma, K. Nakayama, K. Eto, T. Minami, Y. Ando and T. Takahashi, Nature Phys., **7**, 840 (2011).

[21] T. Doert, S. Höffkes, C. Klein, and P. Böttcher, Supplemental issues of Z. Kristallogr. **3**, 52 (1991).

[22] S. Bradtmöller and P. Böttcher, Z. anorg. allg. Chem. **619**, 1155 (1993).

[23] A .M. Glazer, Acta. Cryst. B **28**, 3384 (1972).

[24] P. Böttcher, Th. Doert, Ch. Druska, and S. Bradtmöller, J. Alloys Compd. **246**, 209 (1997).

[25] K. Momma and F. Izumi, J. Appl. Cryst. **44**, 1272 (2011).

[26] B. A. Kuropatwa, A. Assoud, and H. Kleinke, J. Alloys Compd. **509**, 6768 (2011).

[27] K. Momma and F. Izumi, J. Appl. Cryst. **44**, 1272 (2011).

[28] A. Juodakis and C. R. Kannewurf, J. Applied Physics **39**, 3003 (1968).

[29] J.C. Bardeen, L.N. Cooper, and J.R. Schrieffer, Phys. Rev. **108**, 1175 (1957).

[30] L. Vegard, Z. Phys. **5**, 17 (1921); A. R. Denton and N. W. Ashcroft, Phys. Rev. A **43**, 3161 (1991).

[31] A. P. Ramirez and G. R. Kowach, Phys. Rev. Lett. **80**, 4903 (1988).

[32] A. Tari, *The Specific Heat of Matter at Low Temperature* (Imperial College Press, London, 2003).

[33] P. W. Anderson, in *Proceedings of the All-Union Conference on the 'Physics of Dielectrics', Academy of Science, USSR, Moscow, 1958* 290.

[34] W. Cochran, Adv. in Phys. **9**, 387 (1960).

[35] http://elk.sourceforge.net

7 Structure and Superconducitivity of the $Tl_5Te_{3-x}Se_x$ Series

In this chapter, the $Tl_5Te_{3-x}Se_x$ substitutional series is investigated. Previously in Chapter 3 it was shown by both long-range and local structure diffraction data that Tl adopts the unusual oxidation state of 2+ at the octahedral sites in Tl_5Te_3. Because thallium-selenium bonds should exhibit a higher degree of covalency than thallium-tellurium bonds, the selenium-doped analogue may be more likely to undergo charge disproportionation. Though the nature of endmember Tl_5Se_3 remains unsolved, the $Tl_5Te_{3-x}Se_x$ series exhibits site-specific preferential substitution and a superconducting dome.

7.1 Structure of $Tl_5Te_{3-x}Se_x$

In-house x-ray diffraction data collected on the $Tl_5Te_{3-x}Se_x$ series are shown in Figure 7.1.1 along with Rietveld refinement fits to the Tl_5Te_3 structure in the $I4/mcm$ spacegroup. Refinements show that both the structure and symmetry of Tl_5Te_3 are preserved for selenium substitution up to $x = 2.3$. At this level of substitution, hints of peaks which violate the symmetries of both $I4/mcm$ and $I4/m$ begin to grow in; these peaks become clear in the diffraction patterns of samples with higher x as well as a secondary phase of TlSe in the $x = 2.7$ sample. The largest of these peaks (e.g, at $2\theta = 27.2$ and $30.7°$) are present for the Tl_5Se_3 endmember and can be fit to one of the indicated spacegroups, $P4/n$

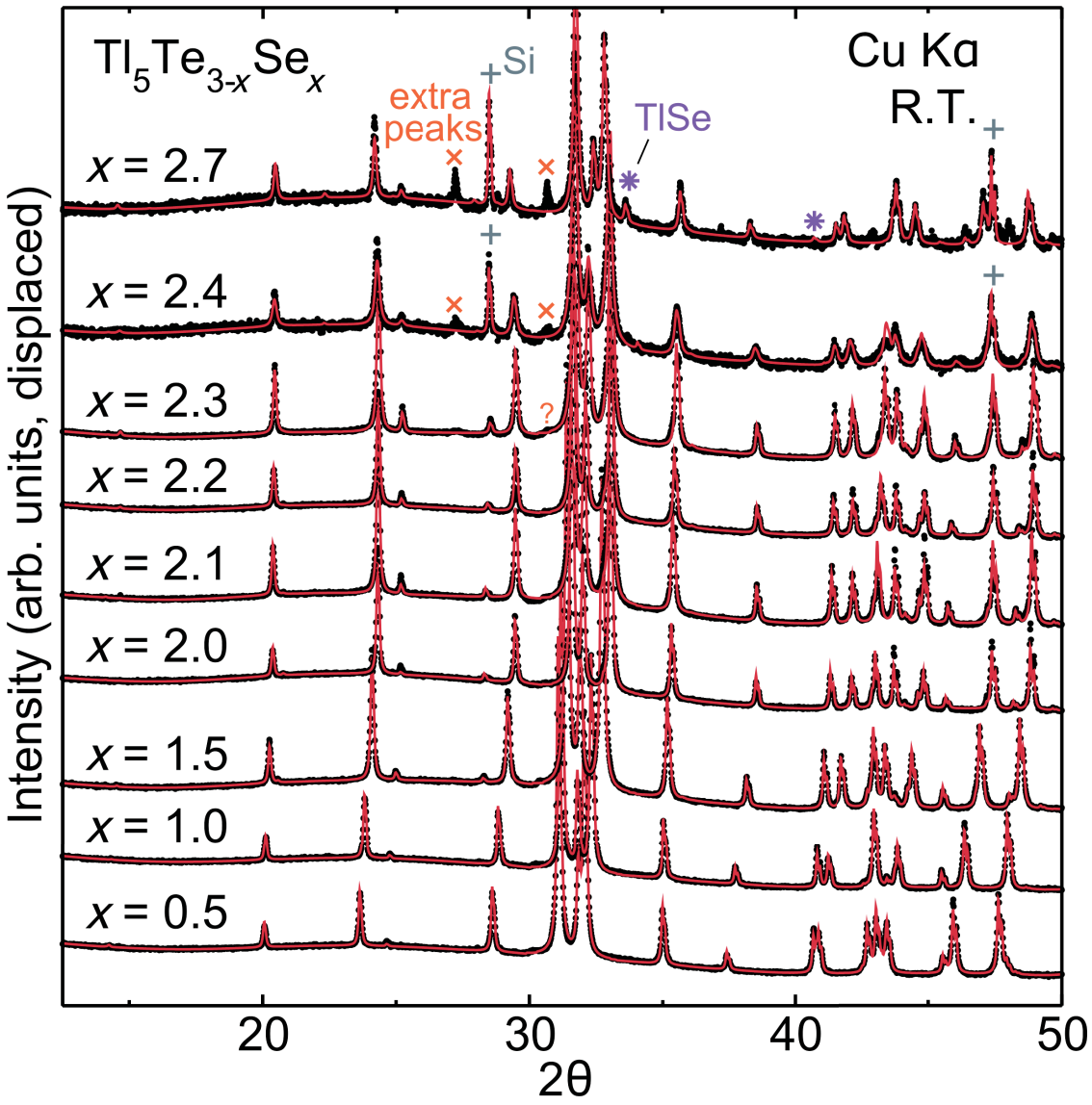

Figure 7.1.1: X-ray diffraction patterns of $Tl_5Te_{3-x}Se_x$ (black circles) with Rietveld refinements (red lines) in *I*4/*mcm*. While samples with $x \leq 2.3$ are well modeled, extra peaks violating the *I*4/*mcm* spacegroup (orange X's) are clearly seen samples with the highest levels of selenium substitution. Additionally, TlSe is observed in the $x = 2.7$ sample, with peaks marked by purple asterisks. Silicon, a common lattice parameter standard, was added to some samples; associated peaks are indicated by gray crosses.

(see Figure 7.3.2). The appearance of Se-rich secondary phase and structural origins of these peaks and secondary phase are discussed in detail in Section 7.3; here we suffice to acknowledge that the changes in structure are likely due to approaching the fully selenide

endmember which has a distorted structure. It is also possible that these peaks may be due to a secondary phase growing in as a function of doping: if the end member were unstable, phases of relatively Se-rich TlSe and some Tl-rich compound may occur.

Figure 7.1.2 shows the lattice parameters, bond lengths, and occupancies extracted from Rietveld refinement in $I4/mcm$ to the XRD data of the $Tl_5Te_{3-x}Se_x$ series. Refinements in spacegroups $I4/mcm$, $I4/m$, and $P4/n$ all return similar parameters. Collectively, the parameters in Figure 7.1.2 all show a dramatic change at $x = 2.0$ subsitution level which can be explained by Se substituting preferentially on the equatorial site ($0 \leq x \leq 2$) before the axial chalcogen site ($x > 2$). The sharp changes in the trends at $x = 2.0$ indicates that the preferential selenium substitutes occurs almost exclusively with minimal anion mixing between the equatorial and axial sites. Note that because samples with highest values of x have the beginnings of a structure change, the refined parameters for these samples are not reliable (and are denoted with empty or shaded symbols): because the refinement model fails to correctly describe the symmetries, other parameters of the refinement may change falsely and/or unphysically to optimize the fit mathematically. With this caveat, these parameters are still presented for consideration of the trends.

7.1.1 Lattice parameters

The in-plane lattice parameter a decreases linearly with selenium substitution up to $x = 2$ for a total decrease of >0.25 Å, while the axial lattice parameter c increases slightly (<0.03 Å) over the same doping range. These trends are consistent with selenium substituting preferentially on the equatorial position: selenium is a smaller anion than the tellurium it is replacing, and the equatorial site mainly affects the a-b plane with minimal effects on the perpendicular c axis. For $x > 2$, the lattice parameter a is minimally affected, while c decreases dramatically (< 0.22 Å). This behavior is consistent with the smaller selenium anion substituting on the axial sites for this range of x.

Incidentally, we note that the changes in lattice parameters increase the c/a ratio (dis-

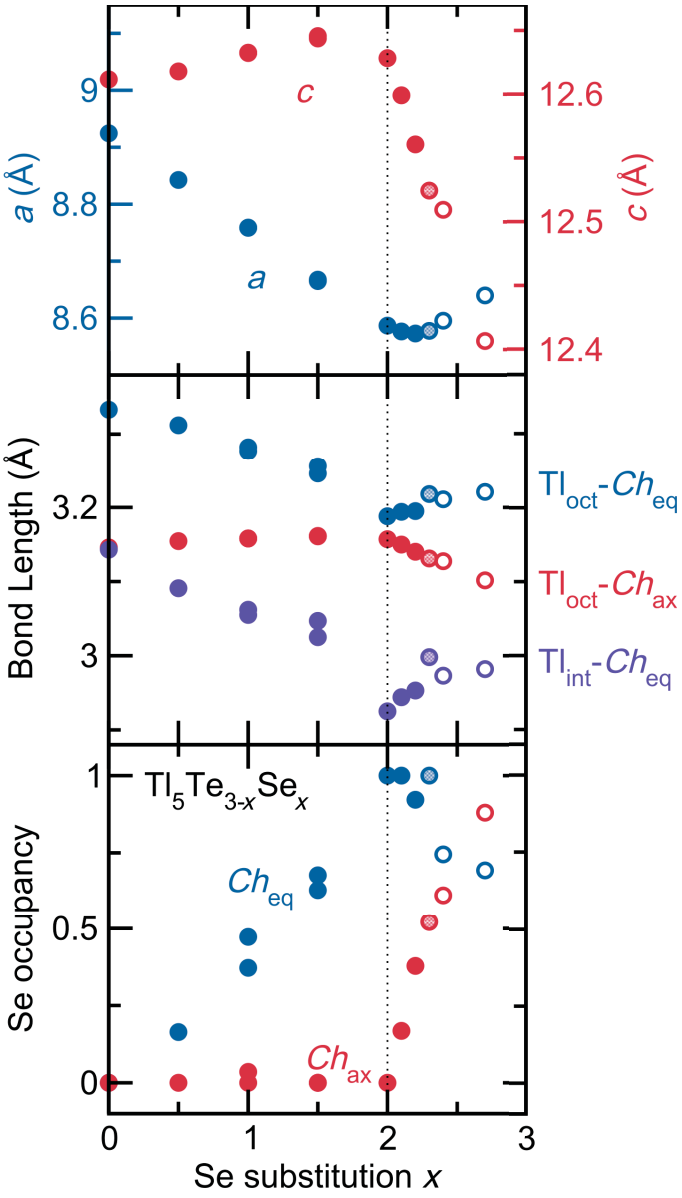

Figure 7.1.2: Lattice parameters (top), bond lengths (middle) and selenium occupancies of the anion sites (bottom) of the $Tl_5Te_{3-x}Se_x$ series as a function of substitution x. The dotted line at $x = 2.0$ demarcates the substitutional level at which the trends change. Parameters are extracted from Rietveld refinements in *I*4/*mcm* spacegroup; filled symbols represent data sets which were well fit by a *I*4/*mcm* model, shaded symbols represent a dataset for which there was a possible deviation from the *I*4/*mcm* model, and empty symbols represent datasets which showed clear deviations from the *I*4/*mcm* model. Blue symbols show trends involving the *a*-*b* plane and the equatorial chalcogen position, while red symbols show trends involving the *c*-axis and the axial chalcogen position. The abbreviations Tl_{oct}, Tl_{int}, Ch_{eq}, and Ch_{ax} refer to the octahedral center thallium, the interstitial thallium, the equatorial chalcogen, and the axial chalcogen respectively. The total occupancy at each chalcogen site was constrained to unity; however, the overall Te:Se ratio (the value of x) was not constrained. Statistical errors are contained within the symbols

cussed in Section 3.2) with x for the $0 \leq x \leq 2$ range then decreases with x for $x > 2$, reaching an overall maximum of c/a = 1.47 at $x = 2$. This c/a ratio far exceeds the typical values of $c/a \approx$ 1.41-1.42 for the Tl_5Te_3 family and approaches the values for In_5X_3 ($c/a \approx$ 1.48-1.49). The change in this ratio does not signify a weakening of the axial bonds because the lattice parameter c is minimally affected; instead, it reflects the anisotropic selenium substitution, shrinking lattice parameter a.

7.1.2 Bond lengths

The bond lengths of the three closest Tl-*Ch* distances are presented in Figure 7.1.2. There are two Tl-$Ch_{\text{equatorial}}$ bonds, one with the thallium at the octahedral centers, and one with the interstitial thallium atoms. Both these bonds decrease linearly with x up to $x = 2$, while the axial bond is largely unaffected for this range of selenium substitution x. For $x > 2$, the axial bond decreases linearly. This behavior is again consistent with the smaller anion selenium substituting on the equatorial sites first, then on the axial sites when the equatorial sites are fully occupied.

There appears to be a small increase in the trends for bonds to the equatorial site for samples with $x > 2$, which is consisent with the slight upswing observed in lattice parameter a for these x. However, the $2.0 \leq x \leq 2.2$ data are within error bars for the equatorial octahedral bond, and the higher x data are not reliable as the Rietveld model no longer encompasses the correct structure(s).

7.1.3 Anion occupancies

Rietveld refinement of anion sites occupancies (Figure 7.1.2) constrained to unity reveals the ratio of chalcogens occupying each anion site. This analysis confirms that the selenium substitutes with 90% or greater exclusivity on the equatorial site for substitution up to $x =$ 2.0: only the equatorial site sees appreciable selenium occupancies for these levels of x, and the occupancy appears to increase roughly linearly with x. Above $x = 2$ doping, selenium

must substitute appreciably onto the axial site if the overall structure is maintained: the selenium occupancy of the axial site does indeed increase for these $x > 2$ in what appears to be a linear trend.

For the $2.0 \leq x \leq 2.3$ samples, the equatorial chalcogen site refines to $> 90\%$ Se occupancy ($< 10\%$ Se occupancy), but this value drops for the $x \geq 2.4$ samples. Strictly interpreted, these refinements signify a mix of selenium and tellurium on both sites; or, put differently, that selenium substitutes onto the equatorial site *less* preferentially in these high-x samples than it does for the $x \leq 2.3$ samples. Such a result would explain the slight upwards trend in a and bonds to the equatorial chalcogens in $x > 2$ samples by the presence of the larger chalcogen, tellurium, in the a-b plane. However, we again note that the refined parameters for samples with the highest substitutional levels x are unreliable. Further, the total occupancy of each anion site was constrained to be unity (the site must be fully filled). As we will discuss in Section 7.3, it is possible that in the fully selenide structure is marked by anion vacancies; it is not unrealistic that the high-x samples also have vacancies that contradict the applied constraint.

No violations of the $I4/mcm$ spacegroup are observed up to $x = 2.2$, indicating that, within the detection limits of our XRD, an upper limit of $\sim 35 - 50\%$ selenium substitution on the axial site is stable. Whether the structure change results from nature of axial thallium-selenium bonding chains or due to other factors is revisited in Subsection 7.3.1.

7.2 Implications of anisotropic isovalent anion substitution

It is interesting that the goodness of fit is not practically improved for refinements in the $I4/m$ spacegroup, nor do fits in this lower symmetry group appear better by eye. $I4/mcm$ has an additional glide plane symmetry element which requires that all octahedra be equivalent while $I4/m$ lifts this requirement, allowing alternating octahedral sizes. As discussed

in Chapter 3, the Tl^{2+} at the octahedral centers is theoretically likely to charge disproportionate is the thallium, so $I4/m$ should better describe the symmetries of a Tl_5Te_3-based structure which undergoes a charge-density wave due to charge disproportionate. Does the lack of observed charge-density wave indicate there is no underlying instability towards a charge disproportionation?

Knowing the pattern by which selenium substitution occurs adds to the understanding of the structure, and may help explain the relationship between bonding and charge disporportionation in this structure. For samples of $0 \leq x$ stoichiometry, virtually all the selenium substitution occurs at the equatorial sites. The bond between the equatorial site and the Tl^{2+} octahedral center ($Tl_{\text{octahedral}}$-$Ch_{\text{equatorial}}$) is the longest, and therefore presumably weakest, bond in the structure. Therefore, substituting on the equatorial site is the anion substitution which has the least effect on the ion prone to charge disproportionation. The bond which most affects the Tl^{2+} ion is the one between the axial site and the octahedral center ($Tl_{\text{octahedral}}$-Ch_{axial}), which hosts selenium substitution for only $2.0 < x \leq 2.2$ before the structure changes visibly in the XRD pattern. It is possible that the structural changes include charge disproportionation; options are discussed further in Section 7.3. However, if the octahedral centers do indeed host an energetically unstable Tl^{2+} ions bonding stongly along the c-axis, it is counterintuitive that the substitution would occur preferentially in a fashion which protects, rather than alleviates, this instability.

We note that the anisotropic substitution of Se^{2-} for Te^{2-} is particularly interesting in that the substitution is isovalent. For several MTl_4Se_3 compounds halogens can be made to substitute for chalcogens at the axial position only, reaching a maximum compound formula of MTl_4Se_2X, X = Cl, Br, and I (see also Section 1.4). Such non-isovalent substitution driven by charge balancing, and therefore is highly likely to be site-specific. A 1- anion should prefer to substitute at those sites which primarily affect the octahedral Tl^{2+} centers, as it can relieve this oxidation state by forming Tl^{1+}-X^{1-} chains extending along the c-axis. In contrast, there exists no such similar driving force for isovalent substitution to

occur directionally.

Another point of interest in this series is the effect on the interstitial thallium ions. Selenium substitution on the equatorial site shortens the $Tl_{interstitial}$-$Ch_{equatorial}$ bond, effectively drawing the interstitial thalliums closer to the planes at (x,y,0) and (x,y,1/2). Because selenium does not substitute appreciably at the axial site for $0 \leq x \leq 2$, the unit cell does not decrease in c, so the interstitial thalliums grow further apart for this range. The interstitial thallium atoms are maximally apart (the Tl_4 clusters or the Tl_8 antiprisms are tallest) in the $x = 2$ compound. The effect of distorting the connectivity of these interstitial thalliums on the physical properties has not been investigated; however, these thallium atoms do contribute to density of states at the Fermi level, and the $x = 2$ compound is the apex of the superconducting trends discussed in Section 7.4. DFT calculations varying the positions of the interstitial thallium atoms could investigate the potential changes to the band structure.

7.3 Structure of Tl_5Se_3

The structure, symmetry, and even stoichiometry of the Tl_5Se_3 endmember has been debated and remains undetermined. The structure appears to be similar to the Tl_5Te_3 structure, but is clearly distorted. It is agreed that the thallium metal centers in Tl_5Se_3 pucker slightly out of the plane of the equatorial anions, displacing thallium from the center of the octahedra. This structural distortion can be described by lowering the symmetry from a body-centered to primitive unit cell with a dispaced origin (Figure 7.3.1). The first two studies on Tl_5Se_3 assigned spacegroups $P4/ncc$ [1] and $P4/n$ [2]; multiple subsequent studies [3–6] have been unable to show either one conclusively. A major structural reason for this confusion is the question of the true selenium stoichiometry in the endmember (whether it is Tl_5Se_3 or $Tl_5Se_{3-\delta}$), and then, if there are selenium vacancies, to what extent and in what pattern(s). The first study on "Tl_5Se_3" concluded there are selenium vacancies corresponding with $Tl_5Se_{3-\delta}$ with $\delta = 0.5$ [1]. They found these vacancies occur solely

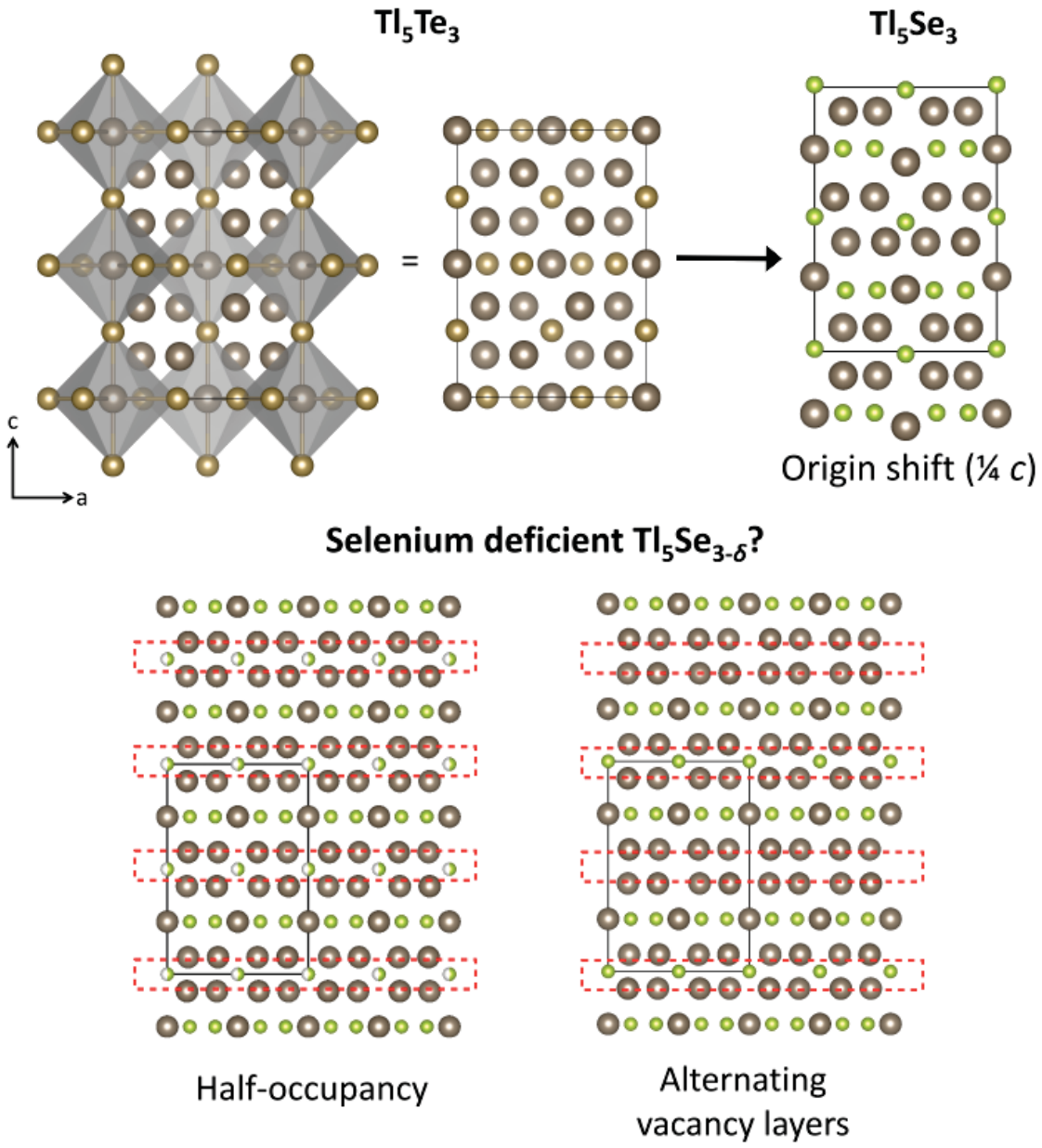

Figure 7.3.1: The possible structures of Tl_5Se_3 reported by the literature are shown. The top row relates the primitive-centered unit cell proposed in the literature to the structure and unit cell of Tl_5Te_3. The bottom row illustrates proposed patterns of selenium vacancies in $Tl_5Se_{3-\delta}$, highlighted by red boxes. Structures are visualized in the VESTA program [7].

on the axial selenium site, making these site half-occupied, and are arranged as alternating layers of occupied and unoccupied axial sites. The second study, published three decades years later and presumably able to more accurately resolve the diffraction data, concluded

there are no vacancieS [2]. The third study on this compound, however, concluded there are indeed selenium vacancies, $Tl_5Se_{3-\delta}$ $\delta \approx 0.5$, which occur randomly on the axial selenium sites [3]. The following studies agree that some selenium deficiency occur with $0 < \delta < 1$, but cannot determine conclusively the precise stoichiometry or if/how these vacancies order (though Böttcher et al. do list the effects of vacancy ordering on the spacegroup, raising the additional possible spacegroup of *P*4*cc*) [4–6]. These possible structures of Tl_5Se_3 and $Tl_5Se_{3-\delta}$ are shown in Figure 7.3.1 with that of Tl_5Te_3 for perspective.

Laboratory XRD results taken in-house on Tl_5Se_3 disagree with both suggested spacegroups *P*4/*n* and *P*4/*ncc* (Figure 7.3.2). Spacegroup *P*4/*n* accounts for several peaks which *P*4/*ncc* does not (e.g., at $2\theta = 30.5°$), but still fails to capture some of the smallest peaks near the baseline and, despite refining occupancies and other parameters such as crystallite size, does not accurately capture the peak intensities. Further, a minor phase of TlSe is repeatedly and consistently observed upon XRD analysis, indicating the main product to be selenium-deficient. Employing a number of synthetic approaches, including quenching, annealing, vapor transport, and selenium insertion, has thus far not produced single-phase stoichiometric Tl_5Se_3. Targeting compositions $Tl_{60}Se_{40}$ through $Tl_{70}Se_{30}$ revealed a what appears to be a single-phase compound at approximately $Tl_{67}Se_{33}$ ($Tl_5Se_{3-\delta}$ with $\delta = 0.5$, or Tl_2Se), while other targeted stoichiometries had visible evidence of elemental thallium or TlSe in the XRD pattern or in the product mixture (elemental thallium is too malleable to grind well for XRD analysis: when such pieces were found, their contribution to the product mixture was estimated by mass in conjunction with Reitveld refinement of phase contributions of the powder). In-house diffraction patterns of phase-pure Tl_2Se shows a better agreement with space group *P*4/*n*, but still the refinement is of poor quality (Figure 7.3.2, bottom panel).

Samples of targeted compositions Tl_5Se_3 and Tl_2Se were sent for high-resolution synchrotron x-ray diffraction (SXRD) to achieve better insight into the possible structure(s) of these compounds. The resultant patterns did not show the same phase in both with excess

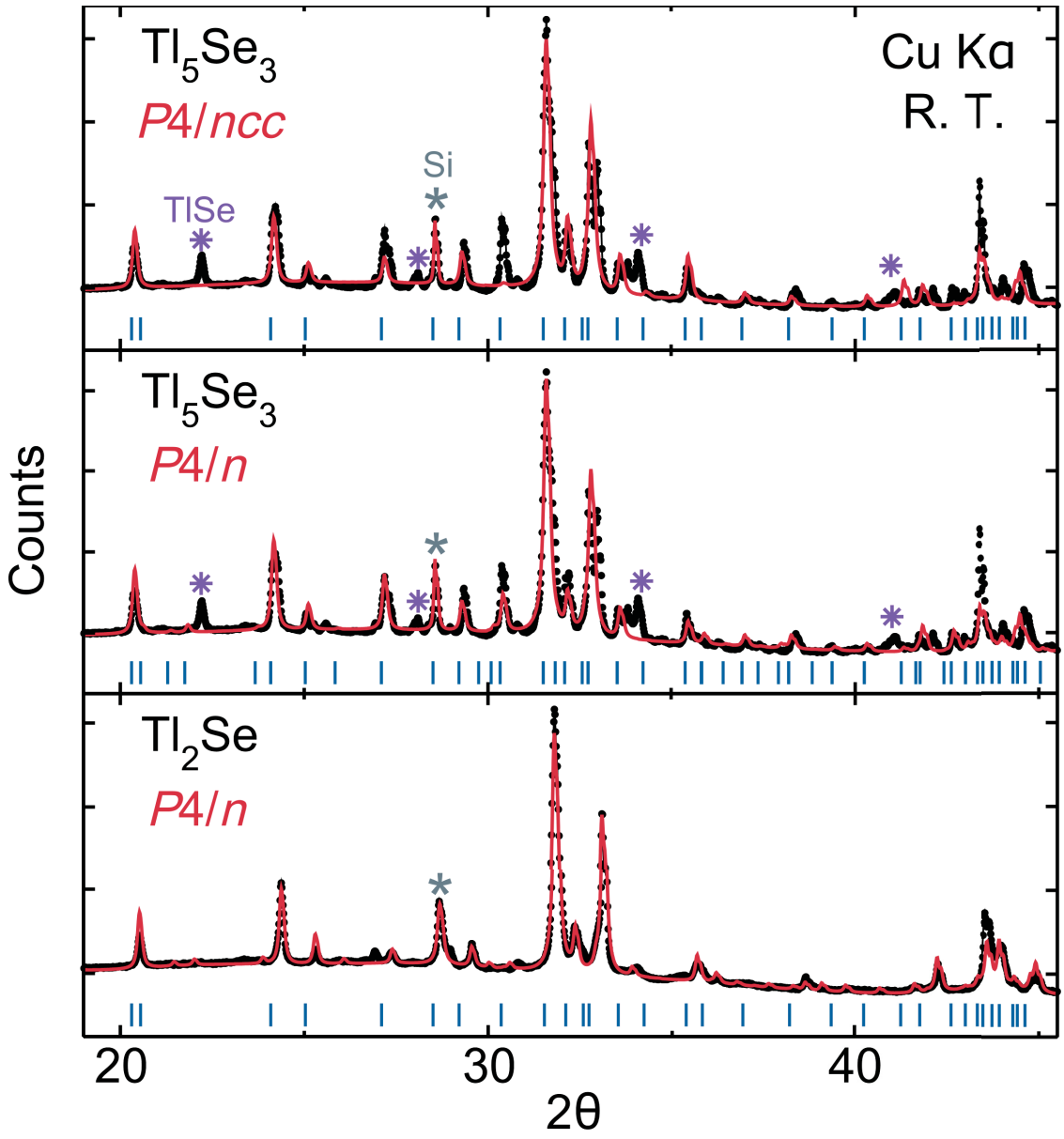

Figure 7.3.2: Laboratory x-ray diffraction patterns of targeted Tl_5Se_3 (top and middle panels) and $Tl_5Se_{3-\delta}$ Tl_2Se are shown with Reitveld refinements in spacegroups *P*4/*ncc* and *P*4/*n*. Data is given by black circles, red lines are the Rietveld refinement, and blue tic marks denote the allowed reflections. The gray and purple stars demarcate peaks due to a Si standard and TlSe, respectively. Intensity is plotted on a $\sqrt{y}$ scale for improved visualization of both large and small peaks from a single perspective.

TlSe in the latter: the main panel of Figure 7.3.3 shows each targeted stoichiometry has peaks that are not found in the other. It is possible these small peaks are due to impurities

which would vary as a function of starting compositions, however, not all of these peaks can be explained by a combination thallium, selenium, and their plausible side products with atmosphere, each other, and the synthesis containers.

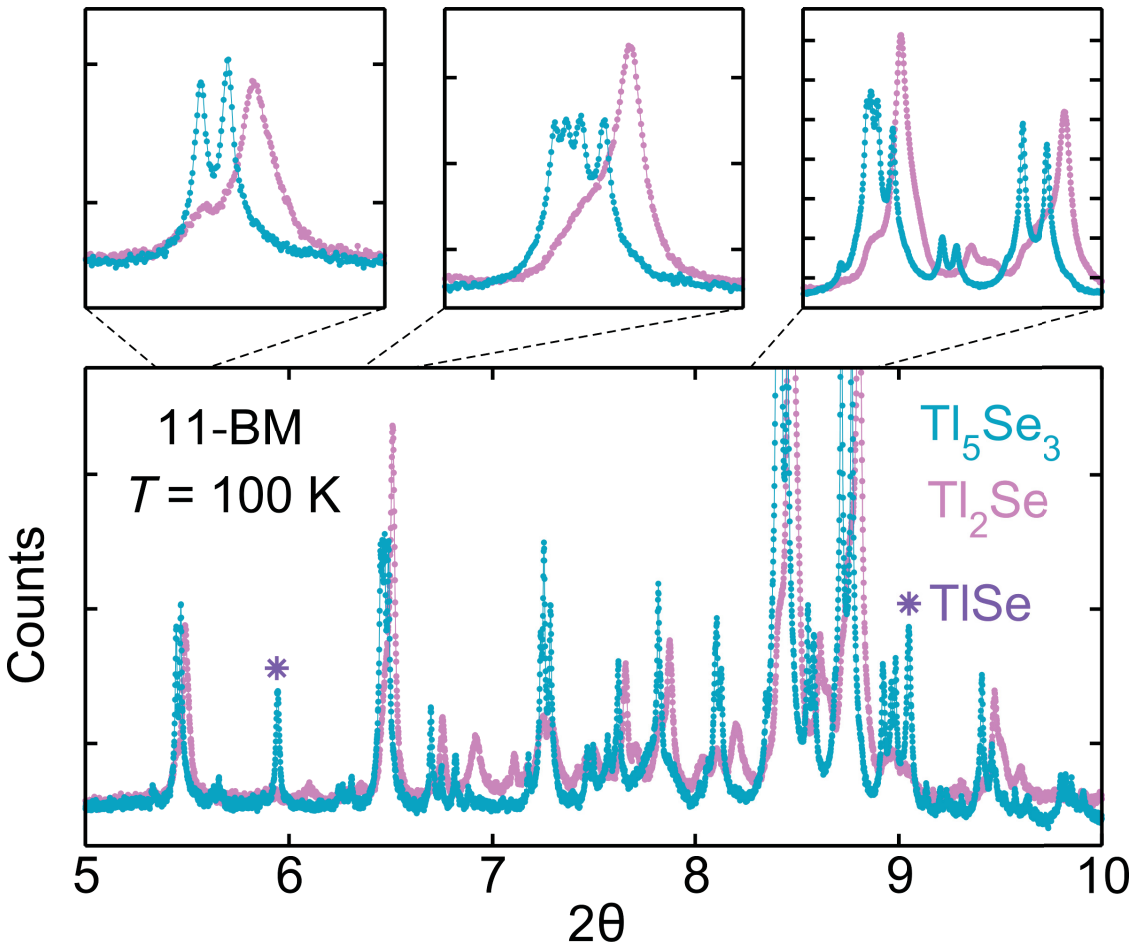

Figure 7.3.3: Synchrotron data taken at 11-BM on targeted stoichiometries Tl_5Se_3 (blue) and Tl_2Se (pink) are dissimilar: Tl_5Se_3 is not merely Tl_2Se with excess TlSe. Above, zoomed insets show splitting of Tl_5Se_3 peaks and shoulders on Tl_2Se. Intensity is plotted on a $\sqrt{y}$ scale for improved visualization of both large and small peaks from a single perspective; high contrast colors are used for the overlaid data also for improved visualization.

Synchrotron data taken on Tl_5Se_3 show (1) a secondary phase of TlSe on the order of a few mole percent, (2) a main phase of orthorhombic or lower symmetry, (3) apparent broadening of the peaks near the baseline, and (4) low-angle peaks possibly indicative of a very large supercell. The presence of TlSe is expected based on the in-house x-ray

patterns. The precise amount cannot be refined from XRD patterns without an accurate model of the main phase. Zooms of select peaks in Figure 7.3.3 illustrate splitting, which could be due to an tetragonal-to-orthorhombic change ($a \neq b$ splits peaks such as the (110)) or due to a transition to a lower symmetry (e.g., a lattice angle deviating from 90°). There is significant broadening visible for some peaks (e.g., at $2\theta = 7.08°$) which is consistent with the experimental sample degrading, possibly due to air- or moisture-sensitivity, to an amorphous material. Additional Tl_5Se_3 samples prepared in an air-free manner were also sent for synchrotron diffraction and showed an improvement in this feature of the diffraction pattern, but still had the numerous small peaks in the range shown in Figure 7.3.3 consistent with the non-air-free samples. Additionally, Tl_5Se_3 samples appeared to have small peaks at very low angles (corresponding to $d > 20$ Å), which, if not due to sample impurity or instrumental/experimental effects specific to that data collection, could indicate a supercell.

High-resolution SXRD data on Tl_2Se reveal many small peaks which violate the *P*4/*n* symmetry (Figure 7.3.4), as indicated in part previously by the in-house diffraction patterns. These peaks could be due to poor sample quality or side products due to targeting an unstable stoichiometry, but no combination of plausible thallium- and selenium-based compounds has been found to satisfactorially model these peaks. It is possible that such peaks are a result of a large supercell due to selenium vacancy ordering, and so various patterns of selenium vacancies in axial atom position targeting $Tl_5Se_{3-\delta}$ with $\delta = 0.5$ were modeled using the program DiFFaX (a program which can model layered structures). While these simulated patterns could explain some of the "extra" peaks present in the SXRD pattern of Tl_2Se, at least four peaks in the SXRD pattern remain unexplained by a periodic layered Tl_2Se structure. In addition to the unexplained peaks, there appear to be shoulders on several of the larger peaks. Zooms of select peaks in Figure 7.3.3 show this explicitly; the shoulders appear to line up with the placement of "Tl_5Se_3" peaks, suggesting trace amounts of the "Tl_5Se_3" phase are present in at least this Tl_2Se-targeted sample. These

data are consistent both an unstable system and with targeting a stoichiometry between two stable compounds.

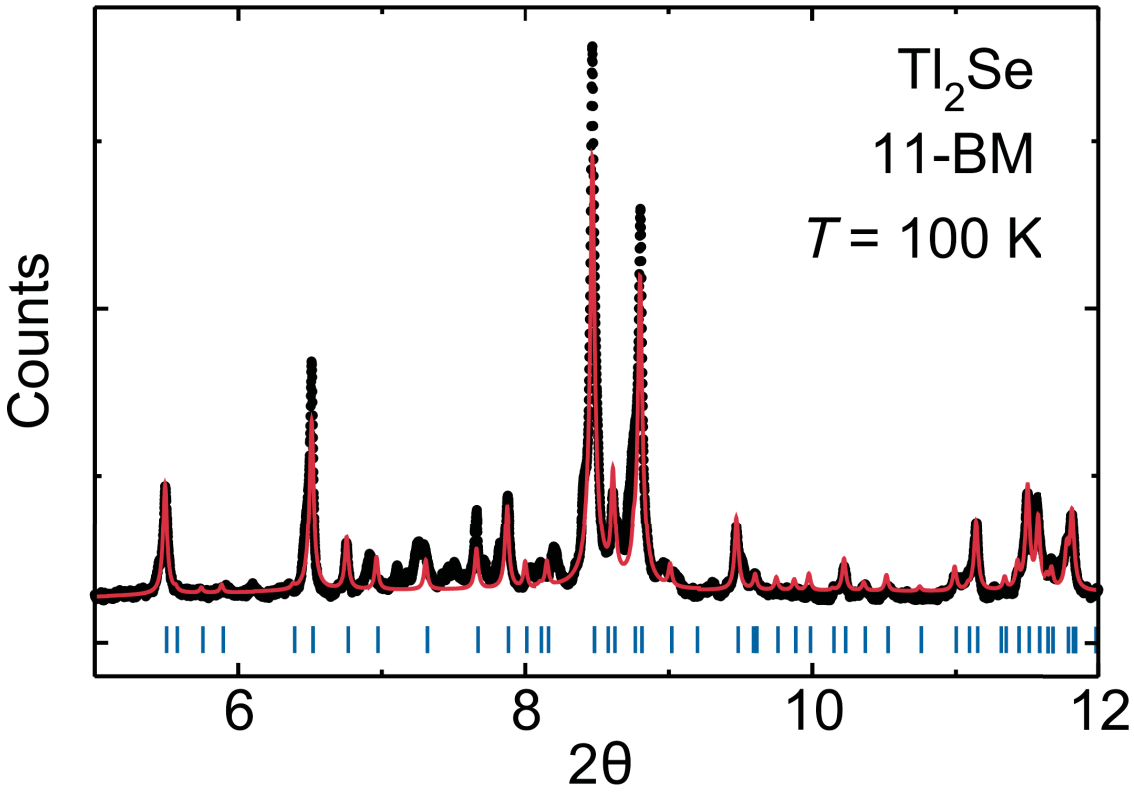

Figure 7.3.4: A *P*4/*n* model (red line) fit to synchrotron data (black circles) taken at 11-BM on targeted stoichiometry Tl_2Se fails to accurately capture all diffraction peaks and intensities. Intensity is plotted on a $\sqrt{y}$ scale for improved visualization of both large and small peaks from a single perspective.

The true structure of "Tl_5Se_3" remains undetermined as of yet. It is likely that the correct stoichiometry for a stable compound, if one exists, has not been properly identified. Towards this end, the tendency towards selenium deficiency must be further investigated and explained. We note here that lower resolution data on $Tl_5Se_{3-\delta}$ and Tl_2Se (in-house laboratory XRDs taken on small amounts of sample with resulting low counts) obscure the small violating peaks and can be fit satisfactorily in spacegroup *P*4/*n*, which is consistent with the lower experimental resolution available when Tl_5Se_3 and $Tl_5Se_{3-\delta}$ were first assigned to those spacegroups [1, 2].

7.3.1 Origin of structure change of Tl_5Se_3

While the structure of $Tl_5Se_{3-\delta}$ is yet to be determined, it clearly deviates in a significant manner from Tl_5Te_3. The reasons behind this change can be speculated:

- loss of selenium due to vaporization
- air-sensitivity
- size
- charge disproportionation
- anion-anion bonding

One might hypothesize that unintended selenium vacancies distort the structure, forming accidental $Tl_5Se_{3-\delta}$ instead of a more symmetric targeted "Tl_5Se_3," perhaps due to unintentional loss of selenium (selenium has a higher vapor pressure than tellurium). This cannot be the explanation: deliberate attempts to make Tl_5Se_3 in Se-rich environments or to add Se to $Tl_5Se_{3-\delta}$ do not result in Tl_5Se_3, and alloying Tl-Se with 60-70 mol% Tl shows no phase-pure Tl_5Se_3. It is possible that the Tl_5Se_3 compound decomposes somewhat in air, which begs the question why it would be kinetically and thermodynamically favorable for Tl-Se bonds to break in favor of Tl-O/Tl-OH bonds in this structure when the Tl-Te bonds in Tl_5Te_3 appeared stable in air on the scale of weeks or more. More likely any air- or moisture-sensitivity of synthesized "Tl_5Se_3" and $Tl_5Se_{3-\delta}$ samples is symptomatic of an unstable structure, rather than the cause of it.

Size could be a contributing factor for the structural breakdown of Tl_5Se_3/$Tl_5Se_{3-\delta}$ compared to Tl_5Te_3: selenium is a smaller anion than tellurium, which has the effect of shrinking the unit cell. Extending the linear trends of the $x \geq 2$ $Tl_5Te_{3-x}Se_x$ samples predicts $c = 12.34$ Å for Tl_5Se_3, smaller than any c lattice parameter of the known Tl_5Te_3 family. Notably, the interstitial thalliums of this structure are collectively rather sizable – there are four putatively 1+ thallium ions each of the A-site cavities between octahedra in

this perovskite-like structure. Compressing the unit cell so much along the c axis could be unstable simply due to the size of these interstitial thallium structures. Comparing the positions of the interstitial thallium atoms in $x = 2.2$ $Tl_5Te_{3-x}Se_x$ (the highest x of the series which has laboratory XRD does not violate $I4/mcm$ symmetries) and in Tl_5Te_3 shows that the interstitial thallium structures are larger in the former, likely because the interstitial thalliums are bonded to the equatorial anions. Therefore the size of the interstitial thallium structures is not a limiting factor, as structures are stable when these interstitials are compressed as they are in Tl_5Te_3. Rather, the close bonds of the equatorial anions with the interstitial thalliums could be a limiting factor. However, the compound $SnTlS_3$ has an arrangement of interstitial thalliums which encroaches further on the octahedral sublattice than that predicted for Tl_5Se_3 based on the trends in $x \geq 2$ $Tl_5Te_{3-x}Se_x$. $SnTlS_3$ has a distorted Tl_5Te_3 structure described by spacegroup $P4/ncc$, allowing the octahedral Tl cations to displace significantly off the polyhedral centers. Thus, size considerations may well contribute the structural distortion of $Tl_5Se_{3-\delta}$, but more research is needed to make definitive statements.

Other possible explanations for the structural distortion include charge disproportionation. As described above, thallium-selenium bonds should exhibit a higher degree of covalency than thallium-tellurium bonds (which are more intermetallic in character) and therefore thallium-selenide bonding may be more likely to result in charge disproportionation of Tl^{2+}. This proposition is only theoretical, but is supported by the geometries of other thallium selenide and thallium telluride compounds such as TlSe and TlTe (the former has two clearly different types of thallium ions, one closely bonded with selenium and the latter does not; in the latter, all the thallium atoms are symmetry-equivalent). If charge disproportionation occurs in a local or complex fashion, simplistic models such as the breathing mode captured by $P4/n$ (which, like $I4/m$, lacks the glide symmetry element which forces the octahedra to be equivalent) may fail to properly describe the resulting structural changes.

We cannot rule out a change in anion-anion bonding as a possible explanation at this time. The Cr_5B_3 structures with larger *c*/*a* ratios have bonding patterns including anion "dumbbells," and Se-Se dimers are not without precedent. We acknowledge the possibility, but do not have significant reason to believe this to be the driving cause of the structural distortion in $Tl_5Se_{3-\delta}$.

7.4 Superconductivity in the $Tl_5Te_{3-x}Se_x$ series

Parent structure Tl_5Te_3 is a superconductor with $T_c = 2.4$ K, while samples of both Tl_2Se and targeted Tl_5Se_3 do not exhibit superconductivity above $T = 1.8$ K. The magnetization response of $Tl_5Te_{3-x}Se_x$ samples to a small applied field is shown in Figure 7.4.1, showing superconductivity exists for samples of partial selenium substitution. The critical temperature T_c increases for $x \leq 2$ (top panel), reaching a maximum at $x = 2$ and $T_c \approx 3$ K. For substitution levels $x > 2$, T_c decreases sharply (bottom panel). Thus $Tl_5Te_{3-x}Se_x$ also can be said to have a superconducting dome, like $Sn_xTl_{1-x}Tl_4Te_3$. However, unlike a more conventional superconducting dome, the maximum does not indicate an optimum charge doping, but rather reflects the substitution patterns, which explains why the trend changes so sharply at $x = 2.0$. Tl_5TeSe_2's unique structure, discussed in Section 7.2, has an extreme *c*/*a* ratio for these compounds, an axially elongated lattice of interstitial thallium atoms, and anisotropic bonding, with Tl-Se bonds in the *a*-*b* plane and Tl-Te bonds along the *c* axis. Any of these structural and bonding changes may explain the increased superconductivity of the $Tl_5Te_{3-x}Se_x$ series; further work must be done to discern between the possibilities.

7.5 $Tl_5Te_{3-x}Se_x$ phase diagram

The phase diagram of $Sn_xTl_{1-x}Tl_4Te_3$ (Figure 7.5.1) summarizes the trends of the series, namely, the superconducting dome, the selenium substitution patterns, and the structural distortion of the Tl_5Se_3 endmember. Selenium substitution occurs preferentially on the

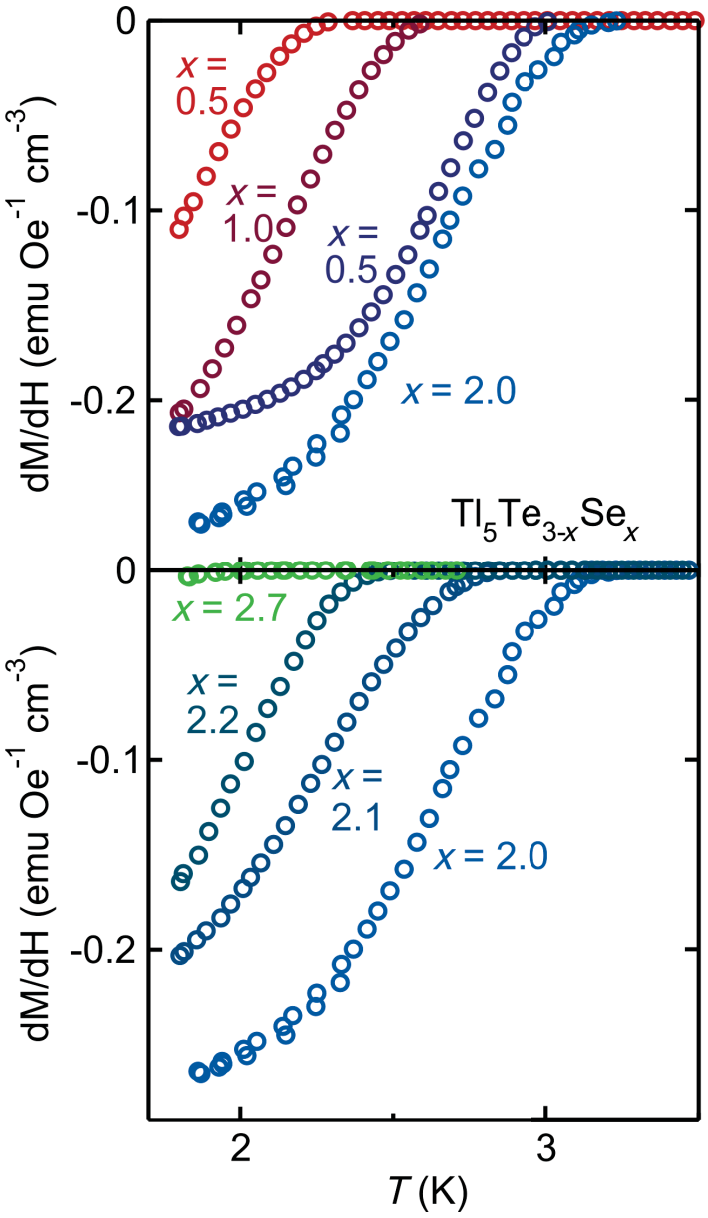

Figure 7.4.1: The magnetic response of $Tl_5Te_{3-x}Se_x$ to a small applied field indicates superconductivity. Critical temperature T_c increases for $x \leq 2$ (top panel), reaching a maximum at $x = 2$ and decreases sharply for substitution levels $x > 2$ (bottom panel).

equatorial site for $x \leq 2$ concomitantly with an increase in the critical temperature T_c. At doping levels above $x = 2$, there is a sharp decrease in T_c, which is quenched below $T_c = 1.8$ K by $x = 2.7$ in samples which are distorted from the Tl_5Te_3 structure. The coexistence of symmetry, bonding, and superconductivity over a similar doping range suggests there may be a relationship between these factors. In the parent Tl_5Te_3 structure, the su-

perconducting signal is more robust (higher H_{c1}) when a magnetic field is applied perpendicularly to c-axis than when applied along it. Note that the selenium-doped derivatives, by substituting preferentially on the axial site, do not disrupt the strong $Tl_{octahedral}$-Te_{axial} bonds along the c-axis (bonds which would be likely to distort with Tl^{2+} charge disproportionation) for $0 \leq x \leq 2$, while the fully substituted selenium endmember "Tl_5Se_3" does.

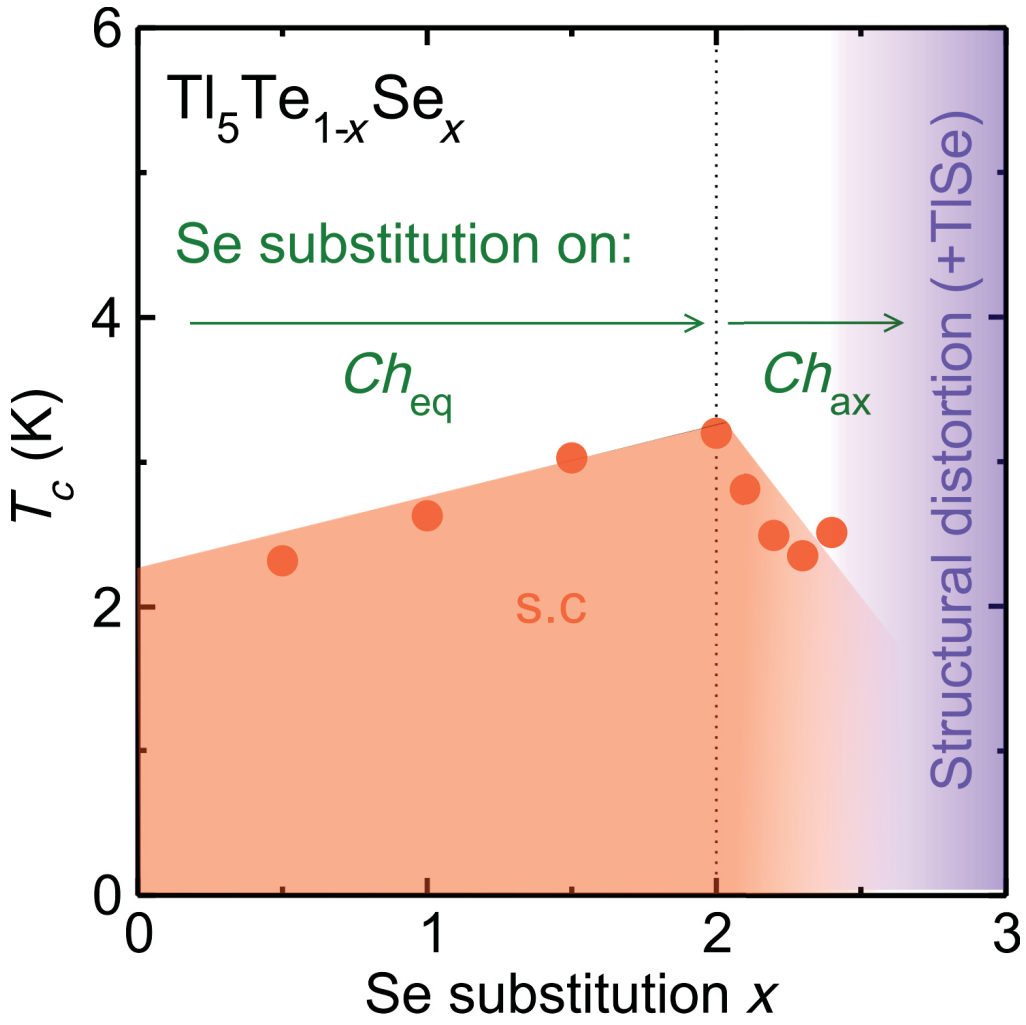

Figure 7.5.1: Plotting T_c as a function of $Tl_5Te_{3-x}Se_x$ substitution x illustrates a superconducting dome with a maximum at $x > 2$. The concurrent Se substitution sites are noted on the graph, suggesting site-specific substitution may have a direct impact on superconducting behavior in $Tl_5Te_{3-x}Se_x$.

This preservation of the bonding along the c for $Tl_5Te_{3-x}Se_x$ $0 \leq x \leq 2$ may have additional affects on physical properties beyond superconductivity. Chapter 5 shows there is a

band-parity inversion at the Z point which gives rise to $\mathbb{Z}_2$ non-trivial topological surface states. The Z momentum correlates with bonding along the c axis; depending on the other effects of selenium substitution on the band structure, it is possible – and likely – that this band-parity inversion may be also be preserved along with the bonding along the c axis for $0 \leq x \leq 2$. Samples with $x > 2.0$ then offer the chance to observe the change in topology as the Z momentum is specifically targeted by substitution along the c axis, especially those in the $2.0 \leq x \leq 2.2$ range which may keep the $I4/mcm$ symmetry. Additionally, as noted in Section 7.2, samples in this range of x could examine the effects of the interstitial sublattice. Because the c distance is not changed for $0 \leq x \leq 2$ but the distance of the interstitial thalliums to the (x,y,0) and (x,y,1/2) planes is, these compounds can probe how the geometry of the interstitials affects the physical properties.

Bibliography

[1] M. M. Stasova and B. K. Vainshtein, Kristallografiya **3**, 141 (1958).

[2] L. I. Man, V. S. Parmon, R. M. Imamov, and A. S. Avilov, Kristallografiya **25**, 1070 (1980).

[3] R. Blachnik and H. A. Dreisbach, J. Solid State Chem. **52**, 53 (1984).

[4] T. Doert, R. Asmuth, and P. Böttcher, J. Alloys Compd. **209**, 151 (1994).

[5] P. Böttcher, T. Doert, C. Druska, and S. Bradtmöller, J. Alloys Compd. **246**, 209 (1997).

[6] F. Römermann, Y. Feutelais, S.G. Fries, and R. Blachnik, Intermetallics **8**(1), 52 (2000).

[7] K. Momma and F. Izumi, J. Appl. Cryst. **44**, 1272 (2011).

8 Crystal Growth and Effect of Off-Stoichiometry in Magnetically Frustrated $Yb_2Ti_2O_7$

The following chapter is based on the article "The Impact of Stoichiometry of $Yb_{2+x}Ti_{2-x}O_{7-\delta}$ on its Structure and Physical Properties" by K. E. Arpino, B. A, Trump, A. O. Scheie, T. M. McQueen, and S. M. Koohpayeh in press, Physical Review B [1].

While the bulk of my graduate research has focused on Tl_5Te_3 family, I have also studied other materials with correlated electron phenomena, notably $Yb_2Ti_2O_7$. $Yb_2Ti_2O_7$ is a three-dimensional geometrically frustrated magnet which has been proposed to be a candidate quantum spin ice and has a low-temperature transition of unknown, presumed-magnetic origin to a much-debated ground state. Careful review of the relevant literature makes it clear there are issues with sample quality in this material. In this chapter, I present structural and physical properties characterization of a doped $Yb_{2+x}Ti_{2-x}O_{7-\delta}$ series to better understand what could be causing so much variation in the literature samples and data. Further, a method for growing a pure single crystal, which is characterized in light of the series, is presented. The series of $Yb_{2+x}Ti_{2-x}O_{7-\delta}$ doped samples demonstrates the effects of off-stoichiometry on $Yb_2Ti_2O_7$'s structure, properties, and magnetic ground state via x-ray diffraction, specific heat, and magnetization measurements. A stoichio-

metric single crystal of $Yb_2Ti_2O_7$ grown by the traveling solvent floating zone technique (solvent = 30 wt% rutile TiO_2 and 70 wt% $Yb_2Ti_2O_7$) is characterized and evaluated in light of this series. Our data shows that upon positive x doping, the cubic lattice parameter a increases and the Curie-Weiss temperature θ_{CW} decreases. Heat capacity measurements of stoichiometric $Yb_2Ti_2O_7$ samples exhibit a sharp, first-order peak at $T = 268(4)$ mK that is suppressed in magnitude and temperature in samples doped off ideal stoichiometry. The full entropy recovered per Yb ion is 5.7 J $K^{-1} \approx Rln2$. Our work establishes the effects of doping on $Yb_2Ti_2O_7$'s physical properties, which provides further evidence indicating that previous crystals grown by the traditional floating zone method are doped off ideal stoichiometry. Additionally, we present how to grow high-quality colorless single crystals of $Yb_2Ti_2O_7$ by the traveling solvent floating zone growth method.

8.1 Introduction

Materials with the pyrochlore structure ($A_2B_2O_7$) are a topic of extensive study in the field of magnetism as ideal hosts for prototypical geometric frustration including both classical and quantum spin-ice and spin-liquid behavior [2–6]. In this structure type, the A and B metal ions each form a sublattice of a corner-sharing tetrahedra; the two sublattices are inter-penetrating. Ising-like (uniaxial) spin interactions on either of these geometrically frustrated tetrahedra sublattices can give rise to spin-ice behavior [2, 4]. In the case of $Yb_2Ti_2O_7$, the magnetic behavior originates in the Yb^{3+} ($4f^{13}$) ions which make up the A sublattice. In an ideally stoichiometric sample of $Yb_2Ti_2O_7$, the magnetic behavior of this Yb^{3+} sublattice is isolated from any interfering magnetic interactions originating in the interpenetrating B sublattice because $3d^0$ Ti^{4+} has no valence electrons.

$Yb_2Ti_2O_7$'s magnetic interactions may be described by an anisotropic exchange Hamiltonian whose exchange parameters have been experimentally ascertained by multiple groups [7–11]. Based on the determined exchange parameters, the ground state of

Chapter 8. Crystal Growth and Effect of Off-Stoichiometry in Magnetically Frustrated $Yb_2Ti_2O_7$

$Yb_2Ti_2O_7$ has been predicted to lie near phase boundaries between ferromagnetic and antiferromagnetic states in theorized phase diagrams [7, 10–16], and it has been suggested that the quantum fluctuations resulting from proximity to these phase boundaries could potentially make $Yb_2Ti_2O_7$ a quantum spin liquid candidate [7]. $Yb_2Ti_2O_7$ has been considered a quantum spin ice candidate due to a finding that the predominant spin exchange is ferromagnetic along the local axis of the tetrahedra [7–9]; however, recent reports indicate the ground state is not that of a quantum spin ice [10, 15]. A number of experimental and theoretical investigations into the true nature of $Yb_2Ti_2O_7$'s ground state described it in widely varying and conflicting fashions: either as lacking [9, 18–24] or having [8, 12, 25–28] long-range magnetic order, with static [25, 27] to slowly fluctuating dynamic [17–20, 22, 24, 26, 29] spins.

Experimental inconsistencies in both the $Yb_2Ti_2O_7$ samples themselves and the measured low-temperature transition to the ground state hinder identification of the true ground state. While powder samples are generally white, the color of crystals varies from deep red to translucent yellow-gray [30, 31]. $Yb_2Ti_2O_7$ has a transition to the presumed ground state at $T \sim 250$ mK which appears to vary considerably between samples. The specific heat signatures of powders generally have a sharp, intense peak around T = 260 mK [22, 25, 29, 32, 33], while those of single crystals grown by the traditional floating-zone method have peaks which occur at lower temperatures ($T \sim 150$ to 200 mK) and are reduced in height by an order of magnitude [12, 22, 25, 29, 34]. Similarly, low-temperature magnetization measurements exhibit transitions at a higher temperature in powder samples than in single-crystal samples ($T = 245$ mK compared to $T = 150$ mK, respectively) [26]. These differences suggest a systematic material discrepancy between single crystal and powder samples, and indicate a better and more consistent method of crystal growth is needed.

Off-stoichiometry likely plays an important role in understanding these differences: in similar pyrochlores, physical properties have been shown to be highly dependent on sam-

ple stoichiometry [35–38]. In $Yb_2Ti_2O_7$, one crystal has been found to be Yb-doped, or "stuffed" (having Yb on the Ti-site), despite having been made from purely stoichiometric powder [39, 40]. Additionally, Chang et al. observed diminished intensity of EXAFS data for those crystals with lower heat capacity peaks in a study of three crystals and concluded that Yb deficiency is responsible for broadening the heat capacity peak [12]. On this basis, it has been generally assumed that all $Yb_2Ti_2O_7$ single crystal are non-stoichiometric, and this off-stoichiometry explains the discrepancy that has been observed between crystal and powder data. However, to our knowledge, the correlation between the stoichiometry and physical properties of $Yb_2Ti_2O_7$ which underlies this assumption has not be systematically investigated.

We report the structural and physical properties characterization of a polycrystalline $Yb_{2+x}Ti_{2-x}O_{7-\delta}$ doped series to elucidate the effects of off-stoichiometry on structure, heat capacity and entropy, and magnetic susceptibility. Additionally, a colorless single crystal of apparently stoichiometric $Yb_2Ti_2O_7$ grown by the traveling solvent floating zone (TSFZ) technique is characterized alongside the doped series. The low-temperature specific heat of the series displays a dramatic change in breadth, height, and temperature of the transition upon doping, while the single crystal has a single, notably sharp peak at $T = 268(4)$ mK.

8.2 Experimental procedures

8.2.1 Synthesis

Synthesized powders having target stoichiometries $Yb_{2+x}Ti_{2-x}O_{7-x/2}$ ($x = 0.08$, 0.02, 0.01, 0.00, -0.01, and -0.02) were prepared from precursors Yb_2O_3 (99.99% Alfa Aesar) and rutile TiO_2 (99.99% Alfa Aesar) in large ($\sim$20 g) batches to minimize mass error. Prior to use, precursors were dried at 1200 °C overnight. Amounts of precursors used were calculated on the basis of metal ion stoichiometries under the assumption that oxygen con-

centration, either excess or deficient, would be corrected by heating in ambient atmosphere ($Yb_{2+x}Ti_{2-x}O_{7-\delta}$). Precursors were combined and intimately ground in a porcelain mortar and pestle, then loaded into an alumina crucible and heated under ambient atmosphere to 1200 °C and held at temperature for 12 h. The material was removed, intimately ground, then pressed into a pellet and reheated in an alumina crucible under ambient atmosphere to 1350 °C and held at temperature for 10 h. This step was repeated several times until powder x-ray diffraction (XRD) patterns showed the precursors were fully reacted. The obtained powders were white.

Sintered rods (rigid, polycrystalline samples) were prepared by compacting and pressing synthesized powders into the form of cylindrical rods (of approximately 6 mm in diameter and 70-80 mm in length), and then sintering at higher temperatures in a four-mirror optical floating zone furnace (Crystal System Inc. FZ-T-4000-H-VII-VPO-PC equipped with four 1-kW halogen lamps) under 2 atm O_2. These polycrystalline rods were sintered by a single pass zone heating below the melting point: a power level of 62% was used for all but the $x = 0$ sample, which was heated at 68% lamp power.

A pure, stoichiometric single crystal approximately 5 mm in diameter and 40 mm in length was obtained via the TSFZ technique [41, 42] using a four-mirror optical floating zone furnace (Crystal System Inc. FZ-T-4000-H-VII-VPO-PC) equipped with four 1-kW halogen lamps as the heating source. The feed and seed rods, attached to the upper and lower shafts respectively, were sintered rods of stoichiometric $Yb_2Ti_2O_7$ powder. The seed rod had been used in a previous $Yb_2Ti_2O_7$ growth; any residual crystalline material at its top (the crystal growth base) was sanded flat. The $\sim$0.2 g solvent pellet used was composed of 30% rutile TiO_2 and 70% stoichiometric $Yb_2Ti_2O_7$ by mass. The solvent pellet was first melted and joined to the feed and seed rod in the optical furnace before beginning the growth. During the growth, the molten zone was passed upwards at a rate of 0.5 mm/h. Rotation rates of 3 and 6 rpm were employed in opposite directions for the feed rod (upper shaft) and the growing crystal (lower shaft), respectively. Crystal growth was carried out

at a power level of 64.2%, which remained fixed throughout the growth, under a dynamic oxygen atmosphere with a pressure of 1 atm and a flow rate of 10 mL/min. Only one zone pass was performed in a crystal growth. Additional clear $Yb_2Ti_2O_7$ single crystals of similar size were grown using the same parameters, indicating reproducibility.

8.2.2 Characterization

Powder X-ray diffraction (XRD) patterns were taken using a Bruker D8 Focus X-ray diffractometer operating with Cu Kα radiation and a LynxEye detector. Diffraction data was analyzed using the Bruker TOPAS software (Bruker AXS). For consistency, all the refinements reported were done on scans ranging from 2θ = 5 to 120 ° with silicon added to the sample as an internal standard. The use of a silicon standard is especially important in cubic materials such as this one, as cubic materials have only one internal lattice parameter which can convolute with the measurement parameters. Uncertainties and error bars reported for lattice parameters reflect the statistical error unless otherwise noted. Site-mixing and doping were individually tested for by holding all other parameters constant from a sample's best fit and intentionally varying the Yb and Ti occupancies to plot the Rwp as a function of site-mixing or doping; errors were estimated from the resulting plot via Hamilton R-ratio tests and visual inspection of the fits.

Physical property characterization was performed using a Quantum Design Physical Properties Measurement System (PPMS). Magnetization data were collected using the ACMS option at T = 2-300 K under $\mu_0 H$ = 0.2 T and converted to magnetic susceptibility using the approximation $\chi = M/H$. Curie-Weiss analyses were performed by adjusting χ_0 to achieve the most linear $(\chi - \chi_0)^{-1}$ in for the temperature range T = 2-30 K. Heat capacity data were collected at constant pressure in two ways (Subsection 2.3.2): using the semiadiabatic pulse technique (2% heat rise) for T = 0.1-2 K and using a large heat pulse (100-200% heat rise from the base temperature, or a 100-200 mK pulse) in the T = 0.1-0.4 K range of the peak. In the semiadiabatic pulse method, C_p is assumed to be

constant over a single short measurement and is extracted by fitting a 2τ heat flow model to the temperature-heat curve. In the large heat pulse method, C_p is not assumed to be constant over a longer measurement, but have distinct values in a series of δT bins. Removing the constant-C_p assumption is known to be better able to capture heat capacity accurately in a first-order transition. Differences in the data between the two methods result from applying heat pulses of different sizes over a transition with considerable latent heat and hysteresis. For consistency, temperature and heat capacity numbers were taken from heating traces for the large heat pulse data, which showed some hysteresis between heating and cooling traces (the peak in the cooling curve appeared approximately 5 mK lower than in the heating curve).

The entropy was calculated by integrating heat capacity divided by temperature of the sintered series up to $T = 2$ K and single crystal up to $T = 300$ K. For all samples, the heat capacity was assumed to be zero at $T = 0$ K in order to place the entropy on an absolute scale, though only entropy for measured temperatures is plotted in Figure 8.5.3. This assumption does not affect ΔS. In the range of $T = 5$ to 30 K, the magnetic entropy was isolated by subtracting the heat capacity of isostructural, non-magnetic $Lu_2Ti_2O_7$ to remove the lattice contribution [30]. Below $T = 5$ K, no lattice contribution was subtracted because the heat capacity of $Lu_2Ti_2O_7$ becomes negligibly small (e.g., $C < 0.01$ J K^{-1} (mol magnetic ion)$^{-1}$ up to $T = 2$ K, which is less than our $Yb_2Ti_2O_7$ measurement error). As the Debye temperatures of the two pyrochlores should be more than 99.5% similar due to atomic masses and stoichiometry [43], the heat capacity of $Lu_2Ti_2O_7$ was not scaled before subtracting it from that of $Yb_2Ti_2O_7$. The entropy curves are only negligibly different for data taken by different heat-pulse techniques.

8.3 Structure

Laboratory x-ray diffraction (XRD) patterns of the $Yb_{2+x}Ti_{2-x}O_{7-\delta}$ synthesized powders and sintered rods samples with target stoichiometries x = 0.08, 0.02, 0.01, 0.00, -0.01, and -0.02 were analyzed via Rietveld refinements using a cubic pyrochlore model to extract lattice parameter, metal-ion substitution, and site-mixing. Doping was presumed to occur as Yb^{3+} and Ti^{4+} ions substituting on the other's Wyckoff positions, with the overall charge discrepancy accommodated by oxygen vacancies or interstitials. Due to oxygen's relatively low x-ray scattering factor in this compound, only the occupancy of the metal ions could be reliably modeled. The XRD patterns show a pyrochlore structure: the presence of peaks such as the (111) in XRD patterns rule out a disordered fluorite structure which is possible for some $A_2B_2O_7$ materials [44].

The cubic lattice parameters a of synthesized powders and sintered rods $Yb_{2+x}Ti_{2-x}O_{7-\delta}$ samples are plotted in Figure 8.3.1, along with those of single crystal samples. Stoichiometric (x = 0) samples agree with most literature values [30, 44–46], although some studies found the lattice parameter at ambient temperatures to be notably lower, around 10.025 Å [39, 47]. As noted in Subsection 8.2.2, cubic lattice parameters are especially sensitive to experimental parameters.

XRD patterns show secondary phases in the synthesized powder samples at higher targeted levels of doping. In the x = 0.02 and 0.08 synthesized powder samples, a Ti-deficient Yb_2TiO_5 secondary phase [44] was observed, indicating the samples have not achieved their targeted stoichiometries, likely due to narrow $Yb_2Ti_2O_7$ phasewidth at lower temperatures as predicted in the composition-temperature phase diagram [48]. Within the limits of our x-ray diffractometer, this impurity phase was not seen in the corresponding doped sintered rod samples, which were processed at higher temperature than synthesized powders. This likely indicates a wider phasewidth towards positive x doping at higher temperatures (above 1350 ° C), which facilitated achievement of the targeted stoichiometries. In the x = -0.02 samples, however, both the synthesized powder and the sintered rod samples show

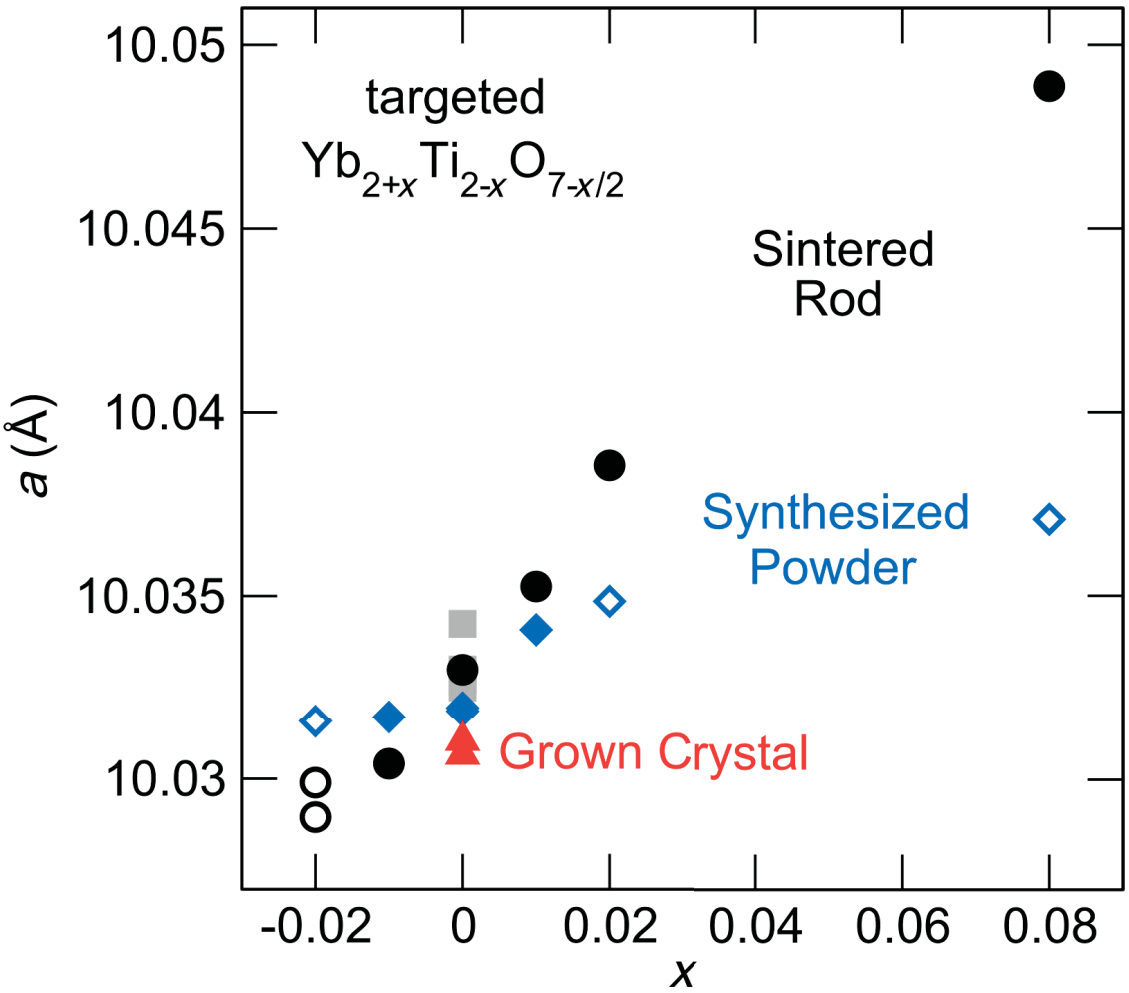

Figure 8.3.1: The cubic lattice parameter a of the synthesized powder (blue diamonds) and sintered rods (black circles) of the $Yb_{2+x}Ti_{2-x}O_{7-\delta}$ series is shown, along with that of the grown single crystal (red triangles, x estimated by Rietveld refinement) and literature values (gray squares) [30, 44–46]. Samples with impurity phases are depicted as hollow symbols: the $x = 0.02$ and $x = 0.08$ synthesized powder samples have a secondary Yb_2TiO_5 phase, and all $x = -0.02$ samples have a secondary phase of TiO_2. Error bars are contained within the symbols.

rutile TiO_2 ($\sim$1-3% TiO_2 by mass) as a secondary phase, possibly indicating a limited phasewidth towards negative x doping, consistent with the phase diagram [48].

For both the synthesized powder and sintered rod $Yb_{2+x}Ti_{2-x}O_{7-\delta}$ series, lattice parameter a increases with x, as expected because Yb^{3+} is larger than Ti^{4+}. The slope of this trend is lesser for the synthesized powder samples, which could result from the samples having a smaller magnitude of doping than intended (due to incomplete reaction and/or side prod-

ucts) or from site-mixing of the cation sites, which essentially averages the ion size. We observe both these effects in Rietveld analysis of the synthesized powders: we detail above the presence of additional phases in higher-doped samples of the synthesized powder series (TiO_2 for Ti-rich $x < 0$ and Yb_2TiO_5 for Yb-rich $x > 0$), and testing for site-mixing in Rietveld refinement reveals approximately 1% site mixing in synthesized powder samples (site-mixing for these six samples refines in the range of 0.5 to 1.2% site mixing with error averaging to 0.35%). In contrast, the sintered rod samples show no evidence of site mixing in Rietveld analysis, refining to zero site mixing as the clear minimum in the goodness of fit. Note that due to the atomic numbers of Yb and Ti (70 and 22, respectively), it is impossible to robustly distinguish whether the $x > 0$ samples have site-mixing or Yb vacancies based on laboratory X-ray diffraction data.

8.4 Single crystal growth

Initial attempts to grow a single crystal of $Yb_2Ti_2O_7$ at its melting point via the previously reported floating zone method [12, 21, 28, 30, 34] from pressed rods of polycrystalline, stoichiometric $Yb_2Ti_2O_7$ (no flux/solvent) yielded a single crystal with a number of questionable features. Firstly, the crystal was dark red in color, which is unexpected for Yb^{3+} and Ti^{4+} ions: Yb^{3+} absorbs in the UV, while Ti^{4+} has no valence electrons to absorb visible light. Density functional theory (DFT) calculations of the band structure support this analysis by predicting an ultraviolet 3.34 eV bandgap [49]. Secondly, the cubic lattice parameter a revealed a significant gradient along the grown crystal which varied from a = 10.05147(5) Å at the start of the grown crystal, consistent with extremely Yb-stuffed, to a = 10.03201(7) Å towards the end, consistent with nearly stoichiometric. Finally, XRD analysis of the frozen remnants of the molten zone showed evidence of titanium oxides as well as $Yb_2Ti_2O_7$ with a smaller lattice parameter (a = 10.0280(1) Å, consistent with $x < 0$ doping). These features suggest that $Yb_2Ti_2O_7$ melts incongruently, in which case

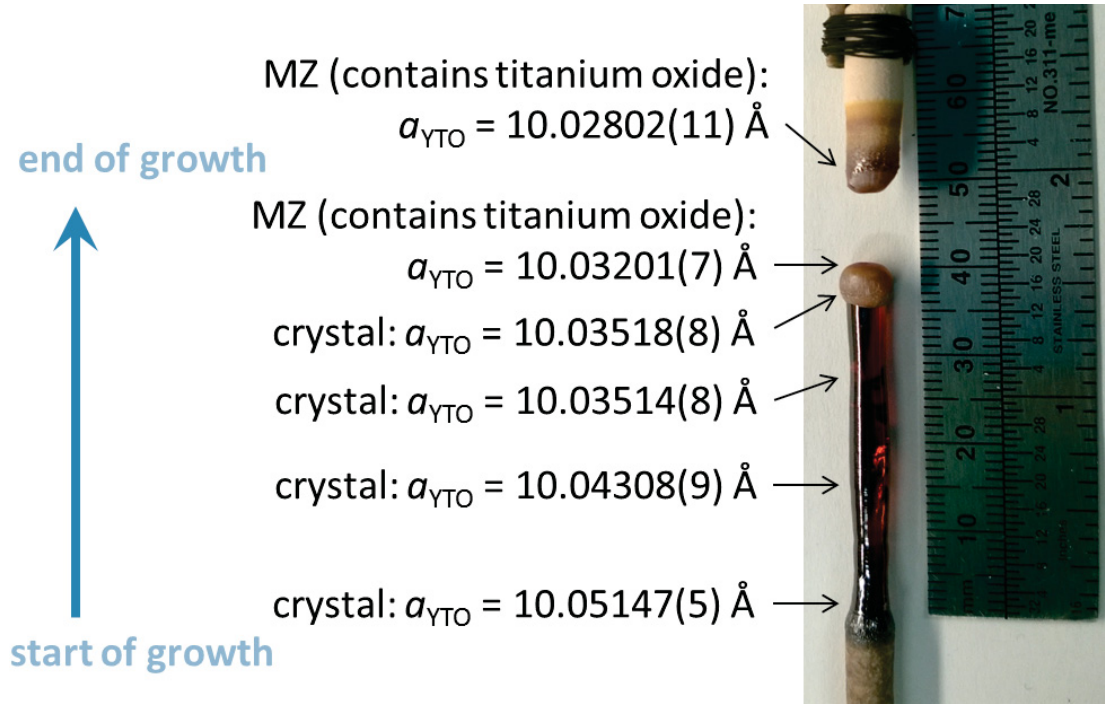

Figure 8.4.1: A crystal grown by the traditional floating zone technique exhibits a deep red color, a significant gradient of the crystal lattice parameter, and secondary phases of titanium oxides in the molten zone (MZ).

the TSFZ method offers an avenue for crystal growth [41, 42]. Due to the existence of a TiO_2–$Yb_2Ti_2O_7$ eutectic at $T = 1620$ ° C, it is possible based on the phase diagram [48] to use a TiO_2–$Yb_2Ti_2O_7$ flux to lower the temperature of the molten zone and precipitate out solid $Yb_2Ti_2O_7$. The specifics of our $Yb_2Ti_2O_7$ TSFZ crystal growth are given in Section 8.2.1.

Using the TSFZ method, the large (40 mm in length, 4 mm in diameter) clear single crystal pictured in Figure 8.4.2 was obtained. The quality and purity of this crystal is supported by its color, steady growth temperature, and Rietveld analysis. As stated above, a stoichiometric crystal of $Yb_2Ti_2O_7$ ought to be colorless due to the ions and the predicted bandgap [49]. It was not necessary to adjust the lamp power level during the growth: it was kept precisely at 64.2% for the whole crystal growth. The power level of an optical furnace correlates with the growth temperature, which is highly sensitive to any slight changes in the composition of the molten zone. The steady lamp power during the growth therefore

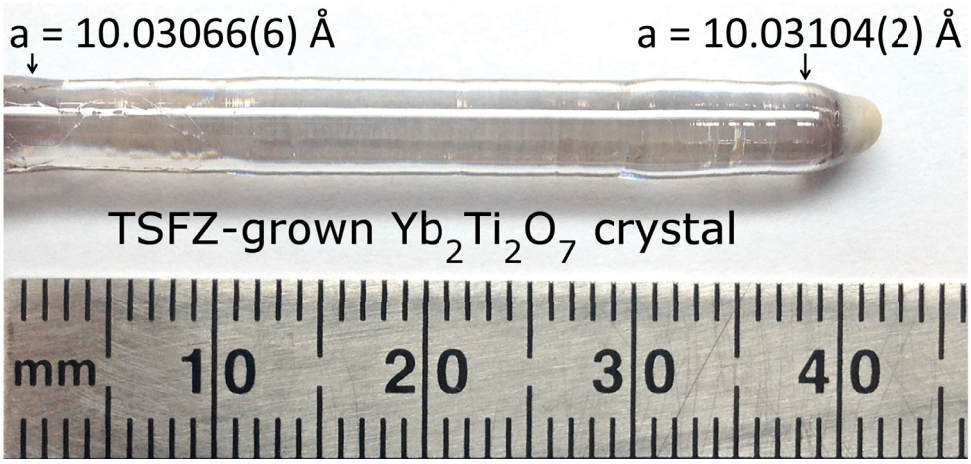

Figure 8.4.2: The TSFZ technique (solvent = 30 wt% TiO_2 and 70 wt% $Yb_2Ti_2O_7$) produces a large single crystal of $Yb_2Ti_2O_7$ that is clear and colorless.

indicates an unchanging stoichiometry of the molten zone: the material leaving the molten zone (the grown crystal) is identical in composition to the material entering the molten zone (the stoichiometric feed rod) [41, 42]. The quality and purity of this crystal were analyzed by Rietveld refinement to the XRD data. The lattice parameter does not change appreciably over the 40 mm length of the grown crystal: a =10.03066(6) Å at the start and 10.03104(2) Å at the end. Refinements specifically to check for $Yb_{2+x}Ti_{2-x}O_{7-x/2}$ doping and site-mixing indicate the crystal may be possibly Ti-rich, refining at $x = -0.005(9)$ with no (0.0(4)%) site mixing indicated. The possibility of small amount of excess Ti is consistent with the crystal growth method and the slightly lowered lattice parameter; however, the metal-ion ratio is within error of stoichiometric. The crystal therefore appears to be of high quality and approximately stoichiometric based on structural analysis; analysis of the physical properties (discussed below) agrees with this conclusion.

8.5 Characterization of the low-temperature transition

8.5.1 Heat capacity

Low-temperature ($T = \sim 0.1$ to 2 K) heat capacity measurements taken on the single crystal and on the sintered rod series are shown in Figure 8.5.1. The specific heat of the single crystal exhibits a single, large (87(9) J (mol f. u.)$^{-1}$ K $^{-1}$), sharp peak at T = 268(4) mK with no other notable features. This is the only crystal in the known literature whose heat capacity shares these attributes with powder data [22, 25, 29, 33]; a table of heat capacity signatures from the literature is presented (Table 8.5.1) for comparison. Given that there is evidence that at least one literature single crystal is off-stoichiometric [39] and a general belief that the off-stoichiometry of single crystals is the cause of the different heat capacity signature, this may suggest our single crystal is not doped off-stoichiometry like literature crystals are presumed to be. A large amount of latent heat is visible in the heat trace of the large pulse data (Figure 8.5.1 inset). The latent heat and the sharpness of the heat capacity peak suggest the transition is first order; additionally, there appears to be some hysteresis in the precise temperature at which the peak occurs depending on whether the data is taken upon heating or cooling, with the temperature of the peak in the cooling curve being about 5 mK lower.

Our sintered rod $Yb_{2+x}Ti_{2-x}O_{7-\delta}$ series displays a trend of the heat capacity peak broadening and decreasing in T and C upon doping. Even slight ($x = \pm 0.01$) doping greatly changes the temperature at which the peak is centered, from $T \sim 268$ mK to $T \sim 235$ and ~ 194 mK. The peak appears to become increasingly broader with doping. For the $x = 0.08$ sample, any feature which may be present is so broad we do not observe it as a recognizable peak, but only in the increased specific heat at the lowest temperatures compared to the other samples.

Our stoichiometric sintered rod sample exhibits a narrow initial peak at T = 265 mK along with at least one broad feature in the $200 < T < 250$ mK range. Though somewhat

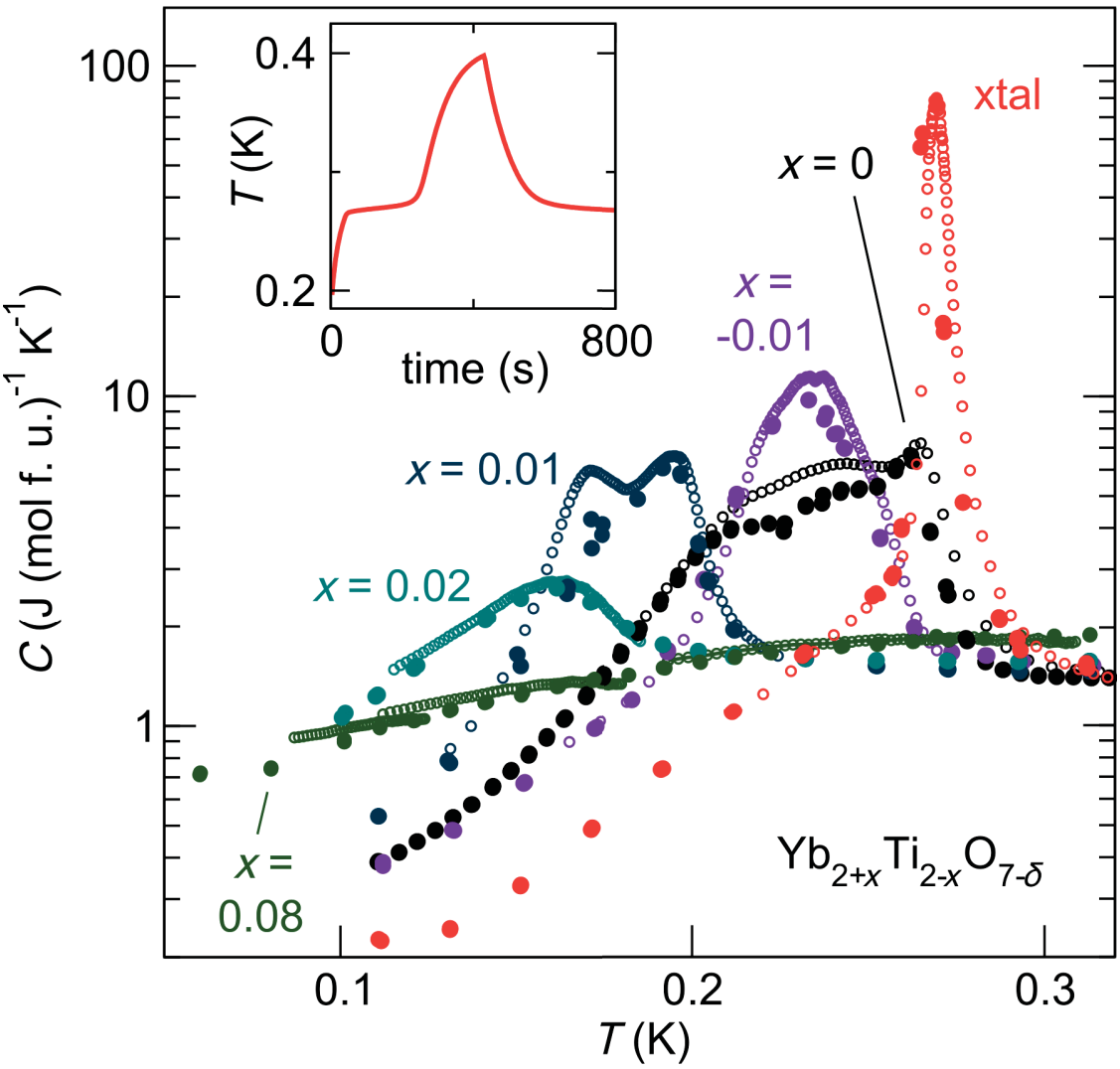

Figure 8.5.1: The specific heat capacity of the single crystal (red) and sintered rod $Yb_{2+x}Ti_{2-x}O_{7-\delta}$ series (darker colors, labeled) exhibit a peak at $T < 300$ mK which broadens and decreases in temperature as $Yb_{2+x}Ti_{2-x}O_{7-\delta}$ is doped away from $x = 0$. Data taken by the semi-adiabatic method are plotted as filled circles, and data taken by the large heat pulse method are plotted as smaller empty circles. Inset: heating trace of the single crystal taken by the large heat pulse method shows a first-order transition, as evidenced by a plateau in the temperature at around $T \sim 270$ mK.

obscured by its placement on the logarithmic scale, this initial feature spikes over 1 J (mol f. u.)$^{-1}$ K $^{-1}$) higher than the surrounding heat capacity and is less than 10 mK wide. It is close in temperature to the heat capacity peak of our single crystal and is similar in temperature, breadth, and height to the sharp initial feature of several crystals by Ross et al.

Table 8.5.1: A comprehensive list of $Yb_2Ti_2O_7$ low-temperature heat capacity peaks in the current literature [12, 22, 25, 29, 32–34, 39]. Values are estimated off published images and converted to the units indicated. Heat capacity is given in terms of J K^{-1} [mol f.u.]$^{-1}$ due to the varying molar amount of magnetic Yb in the series

Publication	**Sample**	**C**	**T**	**FWHM**
		$^{J}/_{K\ (mol\ f.u.)}$	mK	mK
Ross, 2011 [29]	powder	370	268	7
this work	single crystal	87	268	10
D'Ortenzio, 2013 [22]	polycrystal	73	265	14
Chang, 2014 [25]	powder	26	266	23
Blöte, 1969 [32]	powder	20	210	28
Ross, 2012 [39]	crystal: high-T feature	17	266	23
Ross, 2012 [39]	crystal annealed: high-T feature	9.2	267	39
this work	x = -.01	10	233	30
D. de Réotier, 2006[33]	powder	9	265	10
this work	x = 0	7.5	265	10
Chang, 2014 [25]	single crystal	6.8	197	28
Chang, 2012 [12]	single crystal A	6.8	197	20
this work	x = +.01	6	190	35
D'Ortenzio, 2013 [22]	single crystal	4.3	186	31
Ross, 2012 [39]	crystal: low-T feature	4.1	195	23
Ross, 2011 [29]	single crystal B: high-T feature	4.0	268	21
Ross, 2012 [39]	crystal annealed: low-T feature	3.7	195	25
Ross, 2011 [29]	single crystal A	3.1	178	38
Ross, 2011 [29]	single crystal B: low-T feature	3.1	194	31
this work	x = +.02	2.7	160	40
Chang, 2012 [12]	single crystal B	2.4	172	40
Yaouanc, 2011 [34]	crystal # 2 as grown	1.9	164	55
Yaouanc, 2011 [34]	crystal # 1 as grown	1.8	177	52
Yaouanc, 2011 [34]	crystal # 2 with heat treatment	1.8	163	41
Chang, 2012 [12]	single crystal C	n/a	n/a	n/a
this work	x = +0.08	n/a	n/a	n/a

which also have an initial sharp feature and broad humps at lower temperature [29, 39]. We hypothesize that the features below the sharp initial peak in our sample are due to included off-stoichiometry phases. Note a higher sintering temperature was used for this sample (68% lamp power vs. 62% used for the other rods); any partial melting of the sample during the sintering process may have formed non-stoichiometric phases if $Yb_2Ti_2O_7$ is an incongruent melter as is suggested in Section 8.4.

The low, broad peak in heat capacity data of our intermediately doped samples, e.g., the $x = 0.02$, appears most similar to the features of single crystals in the literature: although there is some variety in the specifics of peak shape for the various single crystal samples in the literature (namely the "sharpness" of the peak), all share a decreased and broadened peak centered at lower T than stoichiometric powder data. Single crystals in the literature have a broad peak of C $\leq$ 5 J (mol Yb)$^{-1}$ K $^{-1}$ in the T = 150-200 mK temperature range [12, 22, 25, 29, 34], while powders have much larger peaks at higher temperature ($T \sim 260$ mK) [22, 25, 29, 32, 33]. The varying ranges, scales, and units of graph axes across the literature may hinder ease of direct comparison; we include Table 8.5.1 as a comprehensive comparison of all currently published low-temperature heat capacity date on $Yb_2Ti_2O_7$. Considering the series of doped samples presented in this work, we posit that the crystals in the literature are not stoichiometric, but instead are doped off-stoichiometry systematically due to the crystal growth method employed. Ross et al. have already found one of these single crystals to be doped at a level of $x = 0.046(4)$ [39]. Our series of doping levels illustrates explicitly that the heat capacity peak decreases in both height and temperature in doped $Yb_2Ti_2O_7$.

The heat capacity of $Yb_2Ti_2O_7$ is compared to isostructural, non-magnetic analogue $Lu_2Ti_2O_7$ in Figure 8.5.2. $Lu_2Ti_2O_7$ data from the literature [30] serves as an approximation of the lattice specific heat; because the Debye temperatures of the two pyrochlores should be more than 99.5% similar due to atomic masses and stoichiometry [43], the heat capacity of $Lu_2Ti_2O_7$ does not need to be scaled in order to make the comparison. The

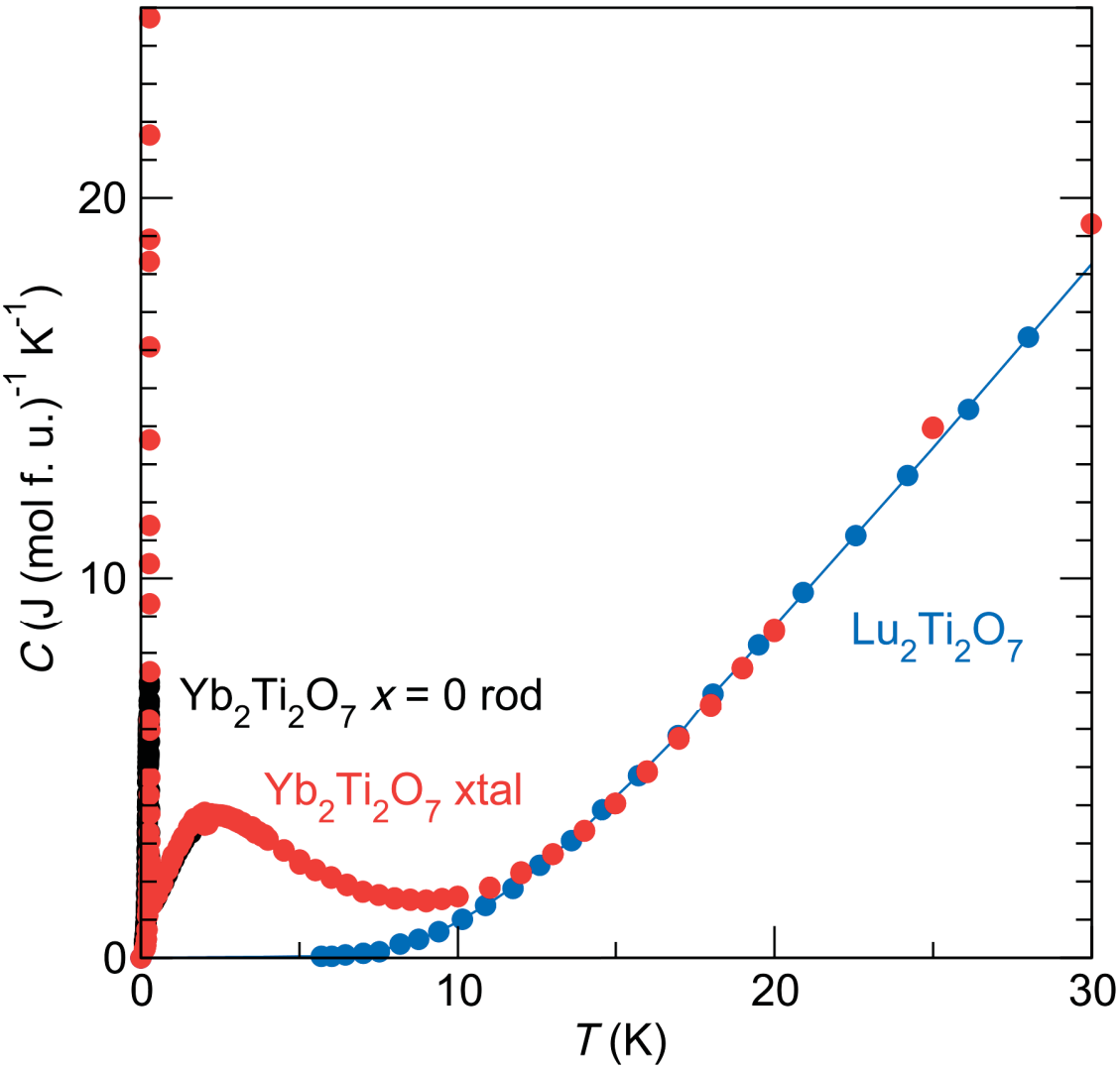

Figure 8.5.2: The heat capacity of our $Yb_2Ti_2O_7$ single crystal (red) and $x = 0$ sintered polycrystalline rod (black) is shown with that of $Lu_2Ti_2O_7$ [30] (blue). Data are shown as circles; the blue line is the $Lu_2Ti_2O_7$ data extrapolated. Subtracting the extrapolated $Lu_2Ti_2O_7$ data from the $Yb_2Ti_2O_7$ data yields the magnetic heat capacity of $Yb_2Ti_2O_7$ used in the paper. (The low-temperature peak extends beyond the scale of this graph and is not shown in its entirety.)

magnetic heat capacity of $Yb_2Ti_2O_7$ is then isolated by subtracting the $Lu_2Ti_2O_7$ data, which approximates $Yb_2Ti_2O_7$'s lattice specific heat, from the $Yb_2Ti_2O_7$ datasets.

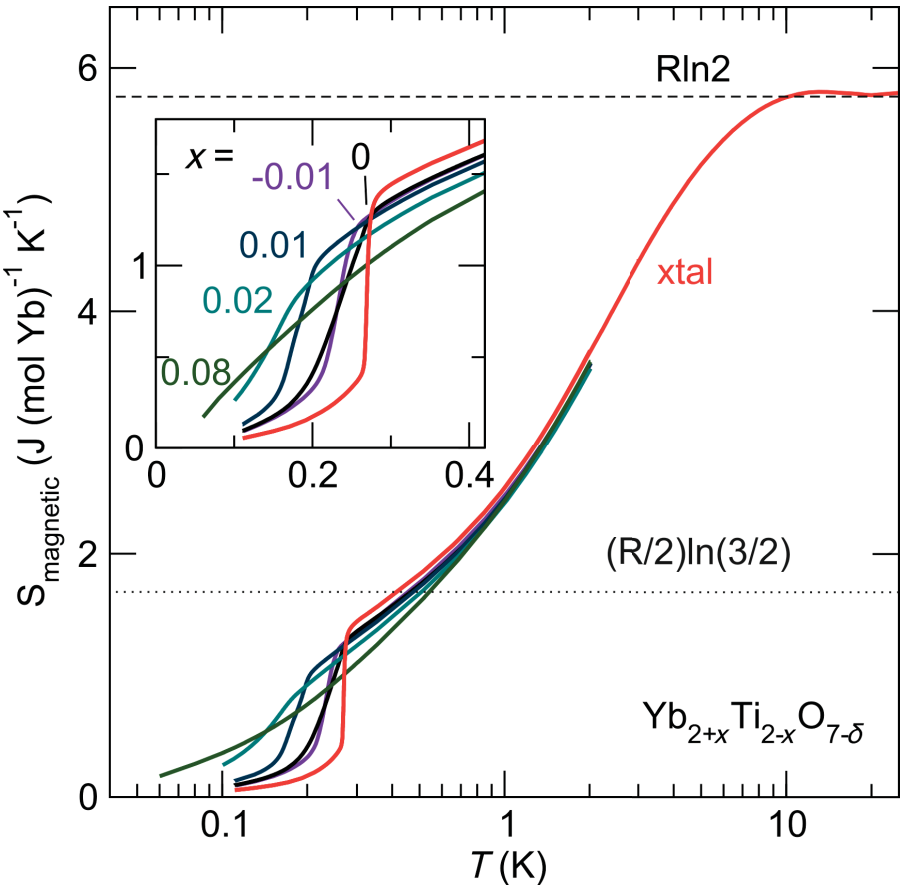

Figure 8.5.3: Magnetic entropy per mole Yb of the single crystal (red) integrated over $\sim 0.1 \leq T \leq 20$ K levels off at the two-state entropy $R\ln 2$ rather than the spin ice limit $Rln2 - (R/2)ln(3/2)$. Magnetic entropy of the sintered rod $Yb_{2+x}Ti_{2-x}O_{7-\delta}$ series (darker colors, labeled in insert) integrated over $\sim 0.1 \leq T \leq 2$ K show that the sharp decrease in entropy at the $T \sim 270$ mK transition broadens significantly as $Yb_{2+x}Ti_{2-x}O_{7-\delta}$ is doped away from $x = 0$ (detailed view in inset). Entropy associated with this broadened transition persists in the doped samples to lower temperatures.

8.5.2 Entropy

Integrating the magnetic heat capacity over temperature as described in Section 8.2 allows evaluation of the magnetic entropy, shown in Figure 8.5.3. The magnetic entropy of the stoichiometric single crystal shows a sharp increase at $T \sim 270$ mK corresponding to the transition as well as a significant increase in the T = 2 to 10 K range corresponding to a hump in the heat capacity, which indicates significant spin correlations above the magnetic transition. The total magnetic entropy per mole Yb appears to approach the two-state

spin entropy $Rln2$ (Subsection 2.3.2). The entropy recovered clearly exceeds the spin-ice entropy of $Rln2 - (R/2)ln(3/2)$, confirming that the magnetic ground state of $Yb_2Ti_2O_7$ cannot be that of a spin ice [10, 15]. The amount of entropy recovered in the transition is similar to the residual entropy of spin-ice; however, the lack of plateau observed indicated the existence of a stable spin-ice-like state above the transition is unlikely. Our results are consistent with $Yb_2Ti_2O_7$ powder and crystalline results in the literature [8, 25, 32], while there are conflicting reports on the total entropy recovered for similar spin-ice pyrochlores [36, 50, 51]. Recovering the full $Rln2$ magnetic entropy in total is consistent with the ground state of $Yb_2Ti_2O_7$ being a ferromagnetic splayed ice state [27, 52] or collinear ferromagnetic state [12, 28], either of which would not have macroscopic residual entropy. Note that as $\Delta S = 5.72$ J K^{-1} (mol Yb)$^{-1}$ for 0.11 K$\leq T \leq$20 K, the assumption that C(T = 0 K) = 0 does not qualitatively affect the result that the entropy recovered is $Rln2$ per mole Yb ion.

Our doped $Yb_{2+x}Ti_{2-x}O_{7-\delta}$ samples all appear to recover similar total entropy as the single crystal over the transition. While these samples were only measured up to T = 2 K, the magnetic entropy at $T = 2$ K of doped $Yb_{2+x}Ti_{2-x}O_{7-\delta}$ is comparative to that of the stoichiometric crystal (C $\sim$ 3.5 J K^{-1} (mol Yb)$^{-1}$), and it is reasonable to assume the doped samples approach the same $Rln2$ per mole Yb limit as the crystal. The recovery of entropy is broadened out over a range of temperatures, especially for the $x = 0.08$ sample. This broad recovery of entropy, in conjunction with a lower transition temperature, indicates spin rearrangement associated with the transition extends to very low temperature in doped samples (e.g., T = 60 mK in $x = 0.08$ sample). This could indicate that measurements of dynamic spins at low temperatures [17–20, 22, 24, 26, 29] may not be accurate measurements of the true ground state if taken on an inadvertently doped sample, as spin entropy associated with the transition remains to lower temperatures for doped samples such as the traditionally grown single crystals.

8.6 Magnetic susceptibility

Magnetization measurements for temperatures ranging from $T = 2$ to 300 K at $\mu_0 H = 0.2$ T were performed on the $Yb_{2+x}Ti_{2-x}O_{7-\delta}$ sintered rod series and the single crystal. The inverse susceptibility is non-linear over the full range even when including a χ_0 term to account for small, temperature-independent contributions (e.g., weak diamagnetism from core electrons). Such non-linearity could result from occupation of excited crystal field levels [17, 39, 47, 53]; however, when applied over a small range at low temperatures to avoid excited crystal field levels, the Curie-Weiss analysis can approximate a line reasonably well. Such an analysis was performed on a per mole Yb ion basis from $T = 2$ to 30 K to focus on the paramagnetic behavior and to best compare to literature analysis (Figure 8.6.1). Analysis on a per mole Yb ion basis is warranted by our initial assumption that substitutional doping does not change the oxidation state of the metal elements in this compound.

The effective magnetic moments p_{eff} per mole Yb for the series and the crystal (Figure 8.6.1(b)) appear to be roughly constant around 3.17, which corresponds to a Curie constant of 1.26 emu K Oe^{-1} per mole Yb ion. These values are similar to the literature values ($p_{\text{eff}} \approx$ 3-3.5) [39, 47, 54]. This result lends support for our initial assumption that Ti substitutes for Yb^{3+} as Ti^{4+} ($Ti^{\bullet}_{Yb}$) rather than Ti^{3+} (Ti^{x}_{Yb}), because magnetically active $3d^1$ Ti^{3+} would increase the magnetic response of the $x < 0$ samples, which is not observed.

The Curie-Weiss temperature (θ_{CW}, Figure 8.6.1(c)) for the whole series is small and positive ($\theta_{CW} = 0.7557(5)$ K for the stoichiometric), suggesting predominantly ferromagnetic interactions. Previous analyses find similar small, positive values for the Curie-Weiss temperature [12, 17, 28, 32, 39, 47, 54]. There is a sharp, notable decrease in the Curie-Weiss temperature with increasing $x > 0$ (corresponding with more Yb^{3+} ions) down to 0.358 K. Presumably, this effect arises from x Yb^{3+} ions substituting on the B sites influencing the interactions of the corner-sharing network of Yb^{3+} on A sites. With the caveat that quantitative comparison of parameters extracted depends considerably on the analysis

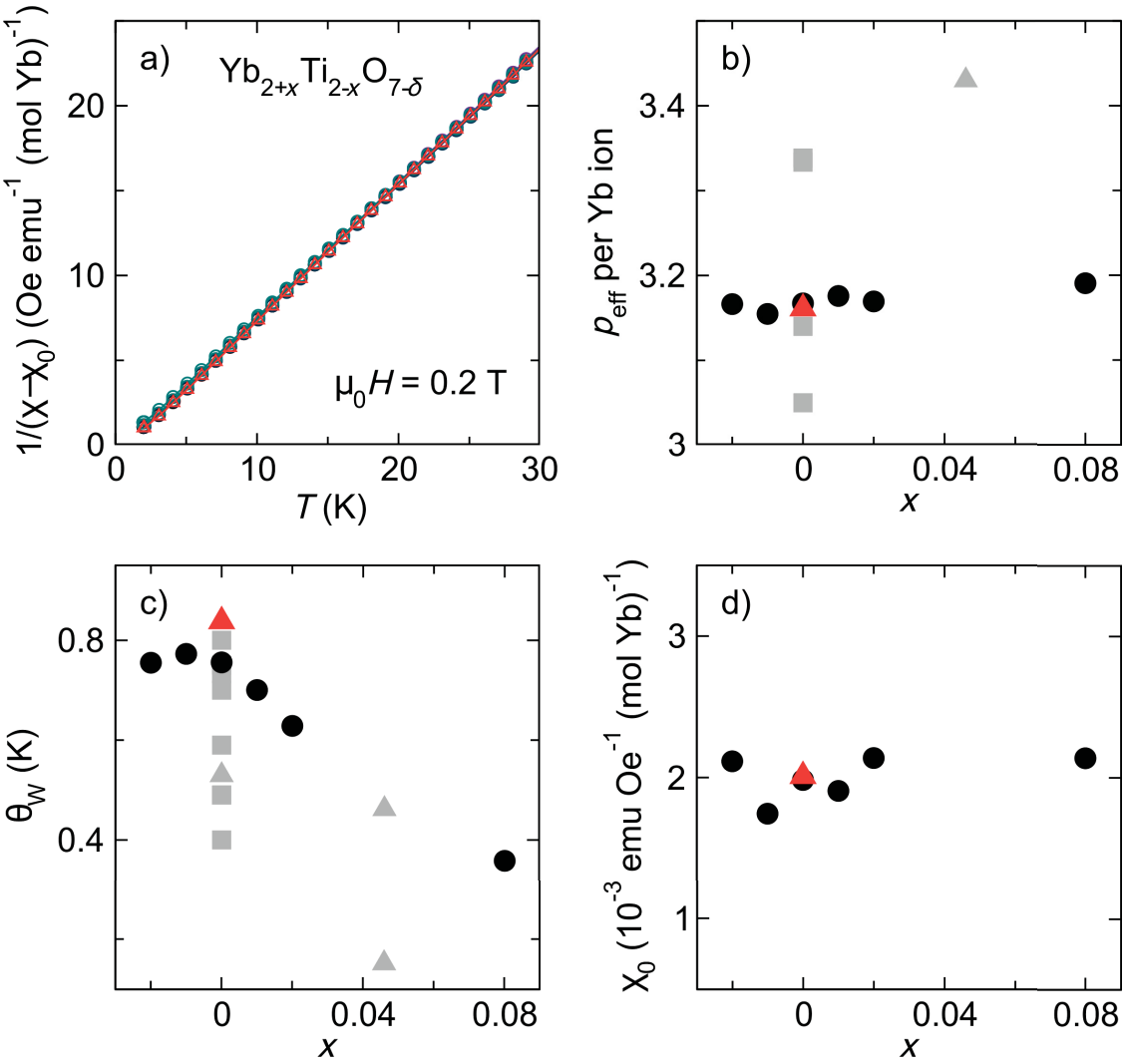

Figure 8.6.1: Curie-Weiss analysis of the magnetic susceptibility of the single crystal (red triangles in b-d) and the $Yb_{2+x}Ti_{2-x}O_{7-\delta}$ sintered rod series (black circles in b-d), with literature values (gray squares and triangles in b-c denote powder [17, 32, 39, 47, 54] and crystal samples [28, 39], respectively) shown for comparison. Statistical error bars from the fit are contained within the symbols. (a) Curie-Weiss fits in the T = 2-30 K range appear linear. The fit to the crystal data is in red and fits to the sintered rod series are in darker colors used in Figures 8.5.1 and 8.5.3; the fits are sufficiently similar that they overlap. (b) The effective magnetic moment p_{eff} per Yb^{3+} ion are randomly distributed around 3.171(8), within the range of literature values. (c) The Curie-Weiss temperature decreases upon $x > 0$ doping (stuffing). (d) Temperature-independent term χ_0 appears randomly distributed.

parameters (including linear regression and temperature range used), we observe that the Curie-Weiss temperature of crystals in the literature appears to generally be lower than that

of powders in the literature (e.g., 0.462 K for the crystal vs. 0.733 K for the powder when similarly analyzed [39]). This observation lends additional support to the hypothesis that crystals grown in the literature are off-stoichometric [39].

The distribution of χ_0 (Figure 8.6.1(d)) appears to be random in the range 0.0017 - 0.0022 emu Oe^{-1} per mole Yb ion for the series and single crystal, and likely reflects the error in the measurement technique rather than any sample dependence. In comparison, we estimate χ_0 to be approximately 0.005 emu Oe^{-1} per mole Yb from a simulation of χ^{-1} as a function of temperature calculated using the crystal field levels given by Gaudet et al. [40].

8.7 Conclusions

We have demonstrated the effect of doping $Yb_2Ti_2O_7$ on its properties by synthesizing and analyzing a $Yb_{2+x}Ti_{2-x}O_{7-\delta}$ series covering a range of stoichiometries. Notably, we show that lattice parameter a increases with doping x, that the Curie-Weiss temperature decreases upon stuffing ($x > 0$), that the peak in the heat capacity shifts to lower temperatures and becomes weaker and broader with doping, and that doping does not affect the total magnetic entropy recovered but does result in dynamic spins persisting to lower temperatures. The properties of crystals in the literature grown via the traditional floating zone method, specifically lower transition temperatures, broader peaks in the heat capacity, and lower Curie-Weiss temperatures, are consistent with our results for off-stoichiometric $Yb_2Ti_2O_7$. It has been generally assumed that off-stoichiometry explains the discrepancy that has been observed between crystal and powder data based on limited data from a few crystals [12, 39]; our study provides the systematic experimental evidence linking stoichiometry to its effects on physical properties.

By nature of their structure, pyrochlores have a number of nearly degenerate ground states; it is possible in such a material for even slight disorder to have significant impli-

cations. Such extreme sensitivity to deviations from perfect crystalline order is expected and observed in related pyrochlores such as $Ho_2Ti_2O_7$, $Tb_2Ti_2O_7$, and $Pr_2Zr_2O_7$ where the single ion ground state is not protected by Kramer's degeneracy [35–38]. It is interesting that we observe a similar sensitivity in $Yb_2Ti_2O_7$ despite Yb^{3+} having a single ion ground state doublet protected by Kramer's degeneracy; the force which causes such sensitivity is unknown. It is possible that the sensitivity of $Yb_2Ti_2O_7$ to disorder is due to proximity of the ground state to different phases, as predicted by several phase diagrams [7, 10–16].

In-depth analysis of structural disorder is necessary to shed further light on the mechanisms by which doping affects the physical properties in $Yb_2Ti_2O_7$. Pyrochlores are known to be susceptible to a variety of structural disorders, ranging from point defects such as cationic site mixing, stuffing, and oxygen vacancies, to extended defects such as antiphase domains (sections of $A_2B_2O_7$ occuring as $B_2A_2O_7$) [55], nanoscale phase separation of doping levels [35], and structural instabilities [56, 57]. High-resolution synchrotron and neutron diffraction on $Yb_{2+x}Ti_{2-x}O_{7-\delta}$ [39, 40, 44, 46, 57, 58] can determine the disorder as a function of doping and synthesis temperature, from which the mechanisms by which minimal doping has such a large effect can be posited. For example, Ross et al. [39] observe stuffed Yb ions, which could broaden the transition by producing a local strain field [40] that locally modulates magnetic interactions, giving rise to micro-regions with varied transition temperatures. Moreover, the ground state phase diagram could be mapped as a function of disorder, and intentional doping could tune the ground state.

In addition to characterizing the effects of doping $Yb_2Ti_2O_7$ on its physical properties, we present a new method of growing stoichiometric $Yb_2Ti_2O_7$ single crystals using the TSFZ method with a solvent mix of $Yb_2Ti_2O_7$ and rutile TiO_2. This method yields a large, pure, colorless single crystal of stoichiometric $Yb_2Ti_2O_7$ with no observable structural gradient. Diffraction, magnetic susceptibility, and heat capacity all support the quality of this crystal; specifically, the heat capacity shows a single, sharp, peak at $T = 268(4)$ mK with a latent heat, indicative of a first order phase transition. This development is especially

important due to the suspected off-stoichiometry of floating-zone grown crystals in the literature. High-quality, undoped stoichiometric crystals are necessary to determine the magnetic interactions of $Yb_2Ti_2O_7$ and its response to applied fields because doped samples may have excess interfering magnetic moments, as indicated broadly by the trends in the Curie-Weiss temperature with doping. Moreover, the ambiguous broadened transition edge at lower temperatures in off-stoichiometric $Yb_{2+x}Ti_{2-x}O_{7-\delta}$ samples could interfere with low-temperature measurements of the ground state. We hope that having access to more pure single crystals of $Yb_2Ti_2O_7$ will advance the ability to accurately probe and understand this intriguing material.

One such measurement is field-dependent oriented low-temperature heat capacity measurements: in conjunction with myself and Dr. Seyed Koohpayeh, the Broholm lab at Johns Hopkins University is currently experimentally determining phase diagrams for fields applied along each crystal direction [100], [110], and [111]. Fields applied unidirectionally can selectively perturb and/or overcome the magnetic exchange interactions, opening up phases which were not accessible in the zero-field compound. We have grown crystals of $Yb_2Ti_2O_7$ grown by the TSFZ method described in this chapter which were oriented and cut/polished with broad (100), (110), and (111) faces in order to prepare them for directional heat capacity measurements. Initial measurements with a range of fields applied along each direction has been taken using the large heat pulse method, and comprehensive analysis of the datasets is underway. Relatedly, the large pulse method, both data collection and processing, is being further developed by Allen Scheie as an improved and more efficient method of gathering heat capacity data on first order phase transitions with large amounts of latent heat.

8.8 Acknowledgments

The Institute of Quantum Matter is supported by Department of Energy (DOE), Office of Basic Energy Sciences, Division of Materials Sciences and Engineering under award DE-FG02-08ER46544. The authors acknowledge helpful input from and conversations with Collin Broholm.

Bibliography

[1] K. E. Arpino, B. A, Trump, O. A. Scheie, T. M. McQueen, and S. M. Koohpayeh Phys. Rev. B, in press (2017).

[2] A. P. Ramirez, Ann. Rev. Mater. Sci. **24**, 453 (1994).

[3] J. S. Gardner, M. J. P. Gingras, and J. E. Greedan, Rev. Mod. Phys. **82**, 53 (2010).

[4] S. T. Bramwell and M. J. P. Gingras, Science **294**, 1495 (2001).

[5] B. Canals and C. Lacroix, Phys. Rev. Lett. **80**, 2933 (1998).

[6] L. Balents, Nature **464**, 199 (2010).

[7] K. A. Ross, L. Savary, B. D. Gaulin, and L. Balents, Phys. Rev. X **1**, 021002 (2011).

[8] R. Applegate, N. R. Hayre, R. R. P. Singh, T. Lin, A. G. R. Day, and M. J. P. Gingras, Phys. Rev. Lett. **109**, 097205 (2012).

[9] N. R. Hayre, K. A. Ross, R. Applegate, T. Lin, R. R. P. Singh, B. D. Gaulin, and M. J. P. Gingras, Phys. Rev. B **87**, 184423 (2013).

[10] J. Robert, E. Lhotel, G. Remenyi, S. Sahling, I. Mirebeau, C. Decorse, B. Canals, and S. Petit, Phys. Rev. B **92**, 064425 (2015).

[11] R. Coldea in *KITP conference, 2015*.

[12] L. Chang, S. Onoda, Y. Su, Y. Kao, K. Tsuei, Y. Yasui, K. Kakurai, and M. Lees, Nat. Comm. **3**, 992 (2012).

[13] A. W. C. Wong, Z. Hao, and M. J. P. Gingras, Phys. Rev. B **88**, 144402 (2013).

[14] H. Yan, O. Benton, L. Jaubert, and N. Shannon, arXiv:1311.3501

[15] L.D.C. Jaubert, O. Benton, J. G. Rau, J. Oitmaa, R.R.P. Singh, N. Shannon, and M. J.P. Gingras, Phys. Rev. Lett. **115**, 267208 (2015).

[16] G. Chen, Phys. Rev. B **94**, 205107 (2016).

[17] H. B. Cao, A. Gukasov, I. Mirebeau, and P. Bonville, J. Phys. Condens. Matter **21**, 492202 (2009).

[18] J. A. Hodges, P. Bonville, A. Forget, A. Yaouanc, P. Dalmas de Réotier, G. André, M. Rams, K. Królas, C. Ritter, P. C. M. Gubbens, C. T. Kaiser, P. J. C. King, and C. Baines, Phys. Rev. Lett. **88**(7), 077204 (2002).

[19] A. Yaouanc, P. Dalmas de Réotier, P. Bonville, J. A. Hodges, P. C. M. Gubbens, C. T. Kaiser, and S. Sakarya, Physica B: Condens. Matter **326**, 456 (2003).

[20] J. S. Gardner, G. Ehlers, N. Rosov, R. W. Erwin, and C. Petrovic, Phys. Rev. B **70**, 180404 (2004).

[21] K. A. Ross, J. P. C. Ruff, C. P. Adams, J. S. Gardner, H. A. Dabkowska, Y. Qiu, J. R. D. Copley, and B. D. Gaulin, Phys. Rev. Lett. **103**, 227202 (2009).

[22] R. M. D'Ortenzio, H. A. Dabkowska, S. R. Dunsiger, B. D. Gaulin, M. J. P. Gingras, T. Goko, J. B. Kycia, L. Liu, T. Medina, T. J. Munsie, D. Pomaranski, K. A. Ross, Y. J. Uemura, T. J. Williams, and G. M. Luke, Phys. Rev. B **88**, 134428 (2013).

[23] S. Bhattacharjee, S. Erfanifam, E. L. Green, M. Naumann, Z. Wang, S. Granovsky, M. Doerr, J. Wosnitza, A. A. Zvyagin, R. Moessner, A. Maljuk, S. Wurmehl, B. Büchner, and S. Zherlitsyn, Phys. Rev. B **93**, 144412 (2016).

[24] P. Bonville, J. A. Hodges, E. Bertin, J. P. Bouchaud, P. Dalmas de Réotier, L.P. Regnault, H. M. Rønnow, J. P. Sanchez, S. Sosin and A. Yaouanc, Hyperfine Interact. **156**, 103 (2004).

[25] L.-J. Chang, M. R. Lees, I. Watanabe, A. D. Hillier, Y. Yasui, and S. Onoda, Phys. Rev. B **89**, 184416 (2014).

[26] E. Lhotel, S. R. Giblin, M. R. Lees, G. Balakrishnan, L. J. Chang, and Y. Yasui, Phys. Rev. B **89**, 224419 (2014).

[27] J. Gaudet, K. A. Ross, E. Kermarrec, N. P. Butch, G. Ehlers, H. A. Dabkowska, and B. D. Gaulin, Phys. Rev. B **93**, 064406 (2016).

[28] Y. Yasui, M. Soda, S. Iikubo, M. Ito, M. Sato, N. Hamaguchi, T. Matsushita, N. Wada, T. Takeuchi, N. Aso, and K. Kakurai, J. Phys. Soc. Jpn. **72**(11), 3014 (2003).

[29] K. A. Ross, L. R. Yaraskavitch, M. Laver, J. S. Gardner, J. A. Quilliam, S. Meng, J. B. Kycia, D. K. Singh, T. Proffen, H. A. Dabkowska, and B. D. Gaulin, Phys. Rev. B **84**, 174442 (2011).

[30] Q. J. Li, L. M. Xu, C. Fan, F. B. Zhang, Y. Y. Lv, B. Ni, Z. Y. Zhao, and X. F. Sun, J. Cryst. Growth **377**, 96 (2013).

[31] K. A. Ross, PhD thesis, McMaster University, 2012.

[32] H. Blöte, R. Wielinga, and W. Huiskamp, Physica **43**, 549 (1969).

[33] P. Dalmas de Réotier, V. Glazkov, C. Marin, A. Yaouanc, P. C. M. Gubbens, S. Sakarya, P. Bonville, A. Amato, C. Baines, and P. J. C. King, Physica B: Condens. Matter **374**, 145 (2006).

[34] A. Yaouanc, P. Dalmas de Réotier, C. Marin, and V. Glazkov, Phys. Rev. B **84**, 172408 (2011).

[35] S. M. Koohpayeh, J.-J. Wen, B. A. Trump, C. L. Broholm, and T. M. McQueen, J. Cryst. Growth **402**, 291 (2014).

[36] G. C. Lau, R. S. Freitas, B. G. Ueland, B. D. Muegge, E. L. Duncan, P. Schiffer, and R. J. Cava, Nature Phys. **2**, 249 (2006).

[37] E. Kermarrec, D. D. Maharaj, J. Gaudet, K. Fritsch, D. Pomaranski, J. B. Kycia, Y. Qiu, J. R. D. Copley, M. M. P. Couchman, A. O. R. Morningstar, H. A. Dabkowska, and B. D. Gaulin, Phys. Rev. B **92**, 245114 (2015).

[38] H. Takatsu, T. Taniguchi, S. Kittaka, T. Sakakibara, and H. Kadowaki, J. Physics: Conference Series **683**, 012022 (2016).

[39] K. A. Ross, T. Proffen, H. A. Dabkowska, J. A. Quilliam, L. R. Yaraskavitch, J. B. Kycia, and B. D. Gaulin, Phys. Rev. B **86**, 174424 (2012).

[40] J. Gaudet, D. D. Maharaj, G. Sala, E. Kermarrec, K. A. Ross, H. A. Dabkowska, A. I. Kolesnikov, G. E. Granroth, and B. D. Gaulin, Phys. Rev. B **92**, 134420 (2015).

[41] S. M. Koohpayeh, D. Fort, and J. S. Abell, Prog. Cryst. Growth Charact. Mater. **54**, 121 (2008).

[42] S.M. Koohpayeh, Prog. Cryst. Growth Charact. Mater. **62**, 22 (2016).

[43] A. Tari, *The Specific Heat of Matter at Low Temperatures* (Imperial College Press, London, 2003), p. 270.

[44] G. C. Lau, B. D. Muegge, T. M. McQueen, E. L. Duncan, and R. J. Cava, J. Solid State Chem. **179**, 3126 (2006).

[45] J. Lian, J. Chen, L. M. Wang, R. C. Ewing, J. M. Farmer, L. A. Boatner, and K. B. Helean, Phys. Rev. B *68*, 134107 (2003).

[46] K. Baroudi, B. D. Gaulin, S. H. Lapidus, J. Gaudet, and R. J. Cava, Phys. Rev. B **92**, 024110 (2015).

[47] S. T. Bramwell, M. N. Field, M. J. Harris, and I. P. Parkin J. Phys.: Condensed Matter **12**, 483 (2000).

[48] G. V. Shamrai, A. V. Zagorodnyuk, R .L. Magunov, and A. P. Zhirnova, Inorg. Mater. **28**, 1633 (1992).

[49] H. Y. Xiao, L. M. Wang, X. T. Zu, Jie Lian, and R. C. Ewing, J. Phys.: Condens. Matter **19**, 346203 (2007).

[50] D. Pomaranski, L. R. Yaraskavitch, S. Meng, K. A. Ross, H. M. L. Noad, H. A. Dabkowska, B. D. Gaulin, and J. B. Kycia, Nature Phys. **9**, 353 (2013).

[51] A. P. Ramirez, A. Hayashi, R. J. Cava, R. Siddharthan, and B. S. Shastry, Nature **399**, 333 (1999).

[52] A. Yaouanc, P. Dalmas de Réotier, L. Keller, B. Roessli, and A. Forget, J. Phys.: Condens. Matter **28**, 426002 (2016).

[53] M. G. Townsend and W. A. Crossley, J. Phys. Chem. Solids **29**, 593 (1968).

[54] J. A. Hodges, P. Bonville, A. Forget, M. Rams, K. Królas and G. Dhalenne, J. Phys.: Condens. Matter **13**, 9301 (2001).

[55] T. Uehara, K. Koto, and F. Kanamaru, Solid State Ionics **23**(12), 137 (1987); T. Moriga, A. Yoshiasa, F. Kanamaru, and K. Koto, Solid State Ionics **31**(4) 319 (1989).

[56] T. M. McQueen, D. V. West, B. Muegge, Q. Huang, K. Noble, H. W. Zandbergen, and R. J. Cava, J. Phys.: Condens. Matter **20**, 235210 (2008).

[57] G. C. Lau, T. M. McQueen, Q. Huang, H. W. Zandbergen, and R. J. Cava, J. Solid State Chem. **181**, 45 (2008).

[58] B. A. Trump (unpublished).

Biography

Kathryn Arpino was born in Boston, Massachusetts on July 11th, 1988 and attended the Wellesley Public School system through high school. She entered the liberal arts institution Hamilton College in central New York state for her undergraduate education. Her introduction to scientific research began there with a STEP-Dreyfus grant which enabled her to work with Professors Gordon Jones and Brian Collett on the aCORN ("a CORrelation in Neutron decay") project the summer before she matriculated. During her time as an undergraduate, Kathryn continued her interest in experimental research under the auspices of Professors Karen Brewer in the Chemistry department and Ann Silversmith in the Physics department in the field of doped sol-gel glasses. Kathryn received a Bachelor of Arts degree in 2010, graduating with a major in Chemical Physics and a minor in Comparative Literature. Additionally, she fulfilled all the requirements for a major in Mathematics. Over the next year, Kathryn took classes and taught chemical laboratory at Columbia University in New York, New York, but spent her evenings reading Professor Tyrel McQueen's research. Ultimately, she contacted Johns Hopkins University and enrolled the following academic year. Since then, she has been fortunate to pursue research in correlated electron materials under Dr. McQueen's guidance as part of the JHU Institute for Quantum Matter (IQM). She has presented a number of talks on her graduate research in the condensed matter physics and solid-state chemistry communities. Additionally, she has both taught and developed chemical laboratory courses at JHU. In her time here, she has found a true second home in the city of Baltimore (though she remains an avid Boston sports fan). The following is a list of scientific publications by the author at the time of this dissertation.

1. K. E. Arpino, B. A, Trump, A. O. Scheie, T. M. McQueen, and S. M. Koohpayeh "The Impact of Stoichiometry of $Yb_{2+x}Ti_{2-x}O_{7-\delta}$ on its Structure and Physical Properties" in press, Phys. Rev. B.

2. K. E. Arpino, B. D. Wasser, and T. M. McQueen "Superconducting Dome and

Crossover to an Insulating State in $[Tl_4]Tl_{1-x}Sn_xTe_3$ " APL Mat. **3**, 041507 (2015). (invited)

3. K. E. Arpino, D. C. Wallace, Y. F. Nie, T. Birol, P. D. C. King, S. Chatterjee, M. Uchida, S. M. Koohpayeh, J.-J. Wen, C. J. Fennie, K. M. Shen, and T. M. McQueen "Evidence for Topologically Protected Surface States and a Superconducting Phase in $[Tl_4]Tl_{1-x}Sn_xTe_3$ Using Photoemission, Specific Heat, and Magnetization Measurements, and Density Functional Theory" Phys. Rev. Lett. **112**, 017002 (2014).

4. T. M. McQueen, P. Cottingham, J. P. Sheckelton, and K. E. Arpino. 2014. Simplified devices utilizing novel pn-semiconductor structures. United States Patent 8,860,078 issued Oct 14, 2014.

5. W. A. Phelan, D. C. Wallace, K. E. Arpino, J. R. Neilson, K. J. Livi, C. R. Seabourne, A. J. Scott, and T. M. McQueen "Stacking Variants and Superconductivity in the Bi-O-S System" J. Amer. Chem. Soc. **135**(14), 5372 (2013).

6. J. M. Caron, J. R. Neilson, D. C. Miller, K. Arpino, A. Llobet, and T. M. McQueen "Orbital selective magnetism in the spin-ladder iron selenides $Ba_{1-x}K_xFe_2Se_3$" Phys. Rev. B. **85**(18), 180405 (2012).

7. K. E. Arpino, A. J. Silversmith, D. M. Boye, and K. R. Hoffman"Post Annealing Immersion: a new technique for studying rare earth ions in porous materials" J. Lumin. **131**(3), 453 (2011).

8. A. J. Silversmith, A. P. Beyler, K. E. Arpino, D. M. Boye, and K. R. Hoffman "Mechanisms of fluorescence enhancement in rare earth doped sol-gel glasses containing Al^{3+}" J. Lumin. **131**(3), 457 (2011).